MIT

Benchmark for
Evaluation
And
Validation of
Reactor
Simulations

RELEASE rev. 3.0.2

*MIT **C**omputational **R**eactor **P**hysics **G**roup*

January 2, 2025

Authors

Nicholas Horelik
Bryan Herman
Matthew Ellis
Shikhar Kumar
Jingang Liang
Benoit Forget
Kord Smith

Acknowledgements

Citation

N. Horelik, B. Herman, B. Forget, and K. Smith. Benchmark for Evaluation and Validation of Reactor Simulations (BEAVRS), v1.0.1. *Proc. Int. Conf. Mathematics and Computational Methods Applied to Nuc. Sci. & Eng.*, 2013. Sun Valley, Idaho

Changelog

1/2/25 - 3.0.2

- Corrected the number of control rod banks reported in Table 1

12/6/20 - 3.0.1

- Corrected outer radius of BP plenum geometry and updated the figrue of top and bottom of the core

- Update formula for density of borated water in borated water composition

- Corrected ARO ITC from -1.71 to 1.71 for Cycle 2 HZP

- Added cooling time between cycles in power history data

- Fixed the axial position of the dashpot in the guide tube

5/22/18 - 3.0

- Introduced uncertainty quantification of measurements

- Deleted inconsistent boron letdown data

- Corrected weight of Inconel per Top/Bottom grid listing in the table of fuel assembly parammeters

10/30/17 - 2.0.2

- Updated Cycle 2 Power History plot to include correct End of Cycle

- Re-calculated all material compositions using latest isotopic natural abundances data, IUPAC 2013

10/26/16 - 2.0.1

- Corrected the critical Boron concentration from 1237 to 1273 ppm in Cycle 2

- Improved re-alignment algorithm in processing measurement data

9/6/16 - 2.0

- Slight shifts to all axial planes

- Added B4C control rod material and updated the control rod specification

- Updated the grid spacer specifications with more accurate heights

- Updated the control rod 0% withdrawn axial location

- Updated the burnable poison insertion axial location

- Added upper plenum and end plugs to burnable poison rods

- Added upper plenum, end plugs, and spacer region to control rods

- Changed from air to helium for control rod and control rod gaps

- Updated neutron shield panel specification

- Updated RPV geometry and material specification

- Added the core liner

- Added water gap between fuel assemblies and baffle

- Added new materials for nozzle and support plate structure to conserve mass and volume fractions

- Added inlet coolant temperature measurements

- Added tilt-corrected data

10/16/13 - 1.1.1

- Added new bare instrument thimble figure and additional clarification regarding instrument tubes below the dashpot.

10/16/13 - 1.1

- Added cycle 2 information: shuffling pattern, burnable absorbers, fresh assembly materials specification, zero power physics test data. For differences and additions see Tables 1, 4-8, and 23, Sources 52, 53 and 71, Sections 2.2.2.1, 2.2.3.1, 3.2 and 3.3, and Figures 15, 17, 19, and 29.

- Added note in Section 3.3 regarding quality of detector trace data

- Added new materials for cycle 2 enrichments

- Added detailed assembly loadings (fresh fuel only) for cycle 2

- All mass densities (and number densities) of fuel have been changed to agree with exact fuel pin dimensions reported in specification

2/21/13 - 1.0.1

- Inconel was misreported as the grid material in Figure 24, changed to Zircaloy

- Grid thickness reported in the caption of Figure 23 did not match figure

- Grid thickness reported in the caption of Figure 24 did not match figure

- Grid strap thickness reported in the caption of Figure 25 did not match figure

1/31/13 - 1.0

- Changed Mass density and composition of SS304

1/18/13 - 0.2.5

- Updated RPV thickness to accurate source

- Updated inconel spring mass and dimension to approximate source

- Changed top/bottom egg-crate dimensions to properly conserve inconel mass. Top/bottom grids now have different radial dimensions vs. intermediate grids for the egg-crate.

- Hot Zero Power temperature was changed from 560 K to 560 F.

- All Fuel material mass and number densities have been changed to reflect actual core-averaged Uranium assembly loading for each enrichment.

- Burnable absorber specification was changed so that the active poison extends from the top of the active fuel to 2 in. above the bottom of the active fuel. The blank pin above burnable absorbers was also changed from Zircaloy to Stainless Steel.

- Added air gap to control rods

- Changed Ag-In-Cd cladding material to SS304

- Changed water density to reflect boron in it (changed boron num dens)

- Fixed Air mass density, factor of 10 lower

- Changed RPV inner and outer radii

12/17/12 - 0.2.4

- Revised instrument tube and burnable absorber tube pincell details above active fuel regions.

12/4/12 - 0.2.3

- Changed instrument tube and guide tube pincell details above and below active fuel regions.

ABSTRACT

Advances in parallel computing have made possible the development of high-fidelity tools for the design and analysis of nuclear reactor cores, and such tools require extensive verification and validation. This document describes BEAVRS, a new multi-cycle full-core Pressurized Water Reactor (PWR) depletion benchmark based on two operational cycles of a commercial nuclear power plant that provides a detailed description of fuel assemblies, burnable absorbers, in-core fission detectors, core loading patterns, and numerous in-vessel components. This benchmark enables analysts to develop extremely detailed reactor core models that can be used for testing and validation of coupled neutron transport, thermal-hydraulics, and fuel isotopic depletion. The benchmark also provides measured reactor data for Hot Zero Power (HZP) physics tests, boron letdown curves, and three-dimensional in-core flux maps from fifty-eight instrumented assemblies. It should be noted however, that not all the necessary data are presented in this document. It will be necessary for analysts to make appropriate judgements and assumptions depending on methods employed.

This document and its associated data package is hosted online at the MIT Computational Reactor Physics Group website `http://crpg.mit.edu/`, where future revisions and refinements to the benchmark specification will be made publicly available.

Contents

List of Figures

List of Tables

List of Source References

Definitions and Acronyms

ARO	All Rods Out
BAF	Bottom of Active Fuel
BP	Burnable Poison
BOC	Beginning of Cycle
CASL	Consortium for Advanced Simulation of Light Water Reactors (LWRs)
CESAR	Center for Exascale Simulation of Advanced Reactors
EFPD	Effective Full Power Days
EPRI	Electric Power Research Institute
FFTF	Fast Flux Test Factility
HZP	Hot Zero Power
IR	Inner Radius
LMFR	Liquid Metal Fast Reactor
LWR	Light Water Reactor
MOX	Mixed Oxide
OR	Outer Radius
pcm	per cent mille
ppm	parts per million
PWR	Pressurized Water Reactor
SS304	Stainless Steel 304
TAF	Top of Active Fuel

1   Introduction

Advances in computing capabilities are further improving the feasibility of fast-running high-fidelity simulations of nuclear cores. Where current core simulations require a series of homogenization procedures to model reactors on a coarse-mesh in order to overcome memory and computer processing limitations [2], modern techniques aspire to provide solutions using fully-detailed geometries with far fewer approximations. For instance, recent research efforts improving the scalability and efficiency of Monte Carlo neutron transport algorithms have resulted in very accurate solutions to the well-known Hoogenboom-Martin problem [3] with the MC21 Monte Carlo code [4] [5], with statistical uncertainties approaching the 1% pin-power accuracy criterion proposed by Smith [6] for full-core Monte Carlo analysis. Likewise, modern deterministic approaches are targeting similar accuracy on some of the world's largest super-computers [7]. Indeed, the development of such high-fidelity full-core modelling capabilities for LWRs is the stated goal of several DOE projects such as CASL (Consortium for Advanced Simulation of LWRs) [8] and CESAR (Center for Exascale Simulation of Advanced Reactors) [9]. However, there is a lack of detailed and relevant benchmarks needed to validate these methods, and a more complete benchmark that includes measured reactor data is presented here.

Nearly all non-proprietary benchmarks do not capture the detail of LWRs needed to validate high-fidelity methods being developed today. For instance, the OECD LWR and Pressurized Water Reactor (PWR) reactor benchmark specifications [10] mostly refer to simple lattice experiments, limited physics testing configurations, and small test reactors. Whereas several full-core LMFR models are available (FFTF, JOYO, etc.), LWRs are markedly under represented. This is particularly true for full-core benchmarks of most interest to the methods development and regulatory community: production reactors similar to operating and planned commercial units. Some recent publications come close to satisfying this need, but they ultimately fall short either in scope or applicability. For instance, a 2011 EPRI report [11] provides reactivity and depletion data with several benchmark specifications for PWR assembly lattices. These benchmarks, while using full-core simulations and measured data, take the approach of reducing the benchmark to single-assembly calculations and do not provide detailed full-core tests or measured reactor data.

A distinction should be noted between the kind of data-backed benchmark being pursued here and the code-comparison benchmarks often used to evaluate methods. For instance, several newer and widely-used LWR benchmarking suites are not backed by measured data, such as the C5G7 MOX benchmarks [12], the Hoogenboom-Martin LWR Monte Carlo benchmark [4], and the approximate PWR specification by Douglas et al. [13]. Instead, comparisons are based on results submitted by many different parties using a variety of codes. Measured reactor data is required for a credible validation.

This document introduces a new benchmark that addresses many of the shortcomings of previous LWR benchmarks by providing a highly-detailed PWR specification with two cycles of measured operational data that can be used to validate high-fidelity core analysis methods.

2   Benchmark Specifications

2.1   Overview

The core geometry specifications are described in 3 levels of increasing scope, detailing each of the hierarchical elements of the model. First the radial geometry is described, followed by a section detailing the axial parameters.

At the lowest level, the radial geometry of each of the pincell types used throughout the core is described. Next, the fuel assembly design is detailed, including the possible configurations of burnable absorbers and the radial specification of the grid spacers. Finally, the greater core geometry is described, including the fuel assembly enrichment locations, the positions of burnable absorbers, instrument tubes, control rod banks, and shutdown banks, as well as the baffle that surrounds the fuel assemblies, the core barrel, four neutron shield panels, and the reactor pressure vessel and liner.

After the radial and axial geometry descriptions, a material specifications section lists the details of each of the materials referred to. Table 1 provides a summary of key model parameters that will be specified in greater detail in subsequent sections, and Figure 1 shows a core cross section indicating the radial structures and assembly loading pattern.

Table 1: Summary of key model parameters.

Core Lattice		Source
No. Fuel Assemblies	193	1
Loading Pattern	w/o U235	
Region 1 (cycle 1)	1.60†	1
Region 2 (cycle 1)	2.40†	1
Region 3 (cycle 1)	3.10†	1
Region 4A (cycle 2)	3.20††	1
Region 4B (cycle 2)	3.40††	1
Cycle 1 Heavy Metal Loading	81.8 MT	3

Fuel Assemblies		
Pin Lattice Configuration	17×17	4
Active Fuel Length	365.76 cm	5
No. Fuel Rods	264	4
No. Grid Spacers	8	4

Control		
Control Rod Material (Upper Region)	B4C	57
Control Rod Material (Lower Region)	Ag-In-Cd	56
No. Control Rod Banks	53	1
No. Burnable Poison Rods in Core	1266	1
Burnable Poison Material	Borosilicate Glass, 12.5 w/o B_2O_3	4

Performance		
Core Power	3411 MWth	6
Operating Pressure	2250 psia	6
Core Flow Rate	61.5×10^6 kg/hr (5% bypass‡)	7

† Cycle 1 Actual core-averaged enrichments calculated from detailed assembly loadings, see Source 70.
†† Cycle 2 Actual core-averaged enrichments calculated from detailed assembly loadings, see Source 71.
‡ It is assumed that 5% of core flow rate goes core into bypass region. A fraction of this flow rate passes through guide tubes. The flow rate should be estimated so that no boiling occurs in these regions.
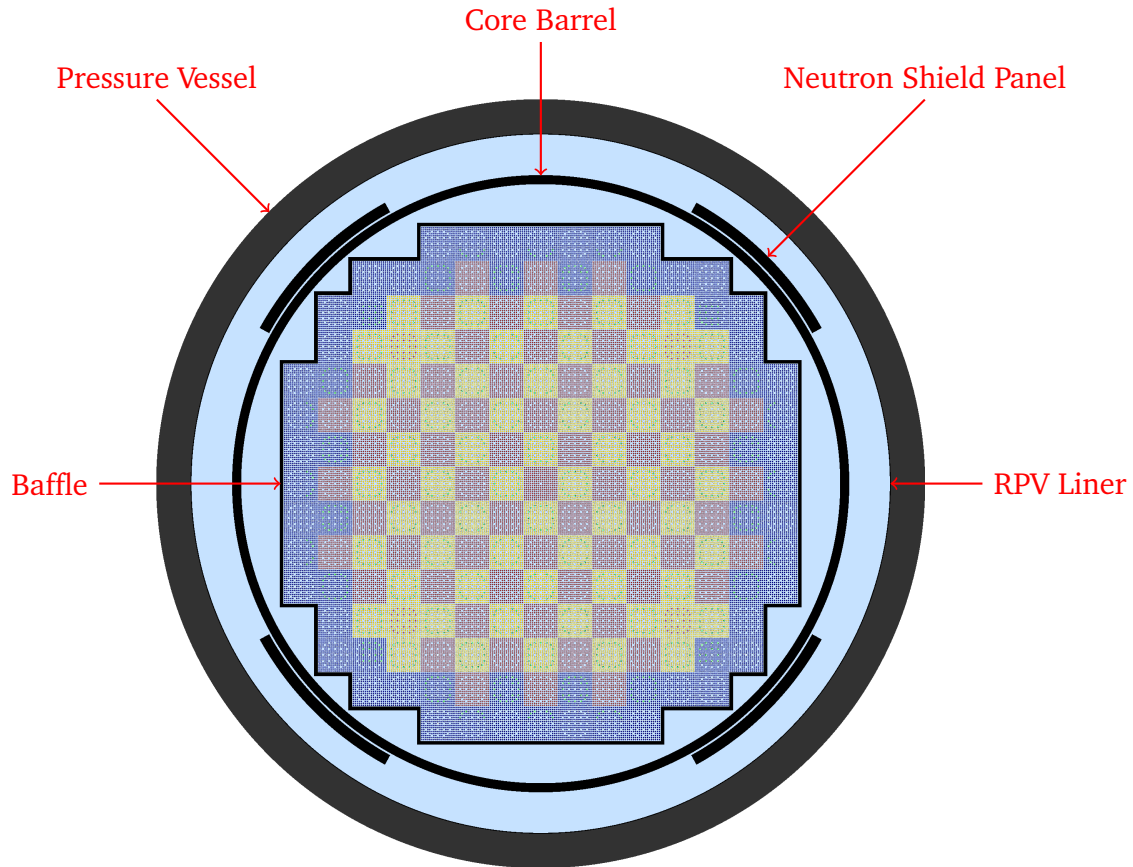
Figure 1: Core cross-section indicating radial structures and enrichment loading pattern (cycle 1). Black denote stainless steel, dark gray denotes carbon steel, light blue denotes water, and red, yellow, and dark blue denote the 1.6, 2.4, and 3.1 w/o U235 regions, respectively.

2.2   Radial Geometry

2.2.1   Pin Types

In this section the radial parameters of each of the pincell types used in the fuel assemblies are detailed. Each of these describes a complete pincell surrounded by the main coolant - in other words, the outer guide tube shell that surrounds instrument tubes, control rods, and burnable absorber rods is presented here as part of those pincells.

While the following radial parameters are constant throughout the axial extent of the core of most pins, a distinction is made for the pins that have components below the control rod stop at the bottom of the core. This region, referred to as the "dashpot", consists of a tapering of the guide tubes to a thinner radius that causes the constriction of flow to naturally prevent control rods from extending too far into the core. In this model, this is approximated by a region of

thinner guide tubes (described further in later sections). Thus radial parameters are provided for pins for both regions where appropriate. Note that the central guide tubes of each assembly (the "instrument tubes") do not shrink for the dashpot.

For all figures in this section, dimensions and materials are specified in order starting from the inner region, through the outer rings. No thermal expansion is considered.

Figure 2 — Fuel Pin
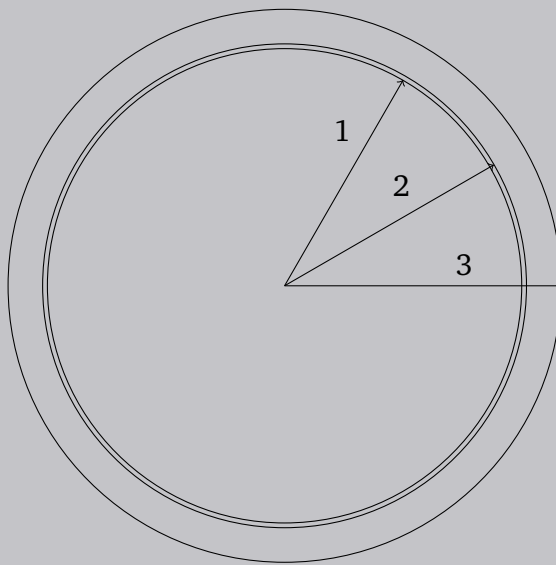
Arrow	Radius (cm)	Material	Source
1	0.39218	Fuel	8
2	0.40005	Helium	9
3	0.45720	Zircaloy	10

Figure 3 — Upper Fuel Pin Plenum
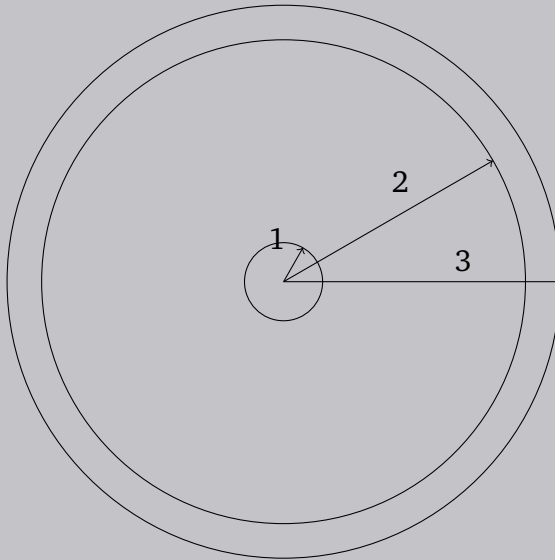
Arrow	Radius (cm)	Material	Source
1	0.06459	Inconel	11
2	0.40005	Helium	9
3	0.45720	Zircaloy	10

This shows the radial geometry used in the upper plenum region of the fuel pins, with a small mass of Inconel to approximate the spring.

Figure 4 — Empty Guide Tube Geometry above Dashpot
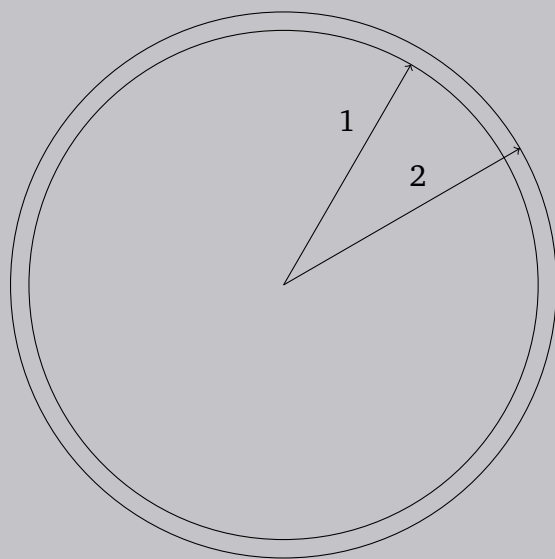
Arrow	Radius (cm)	Material	Source
1	0.56134	Water	13
2	0.60198	Zircaloy	14

Figure 5 — Empty Guide Tube Geometry at Dashpot
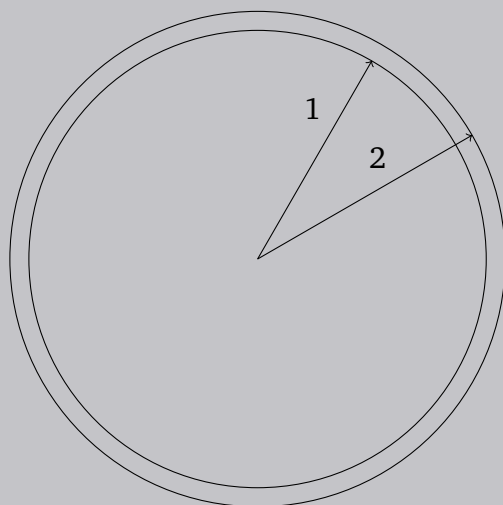
Arrow	Radius (cm)	Material	Source
1	0.50419	Water	15
2	0.54610	Zircaloy	16

Figure 6 — Instrument Tube Pin Geometry
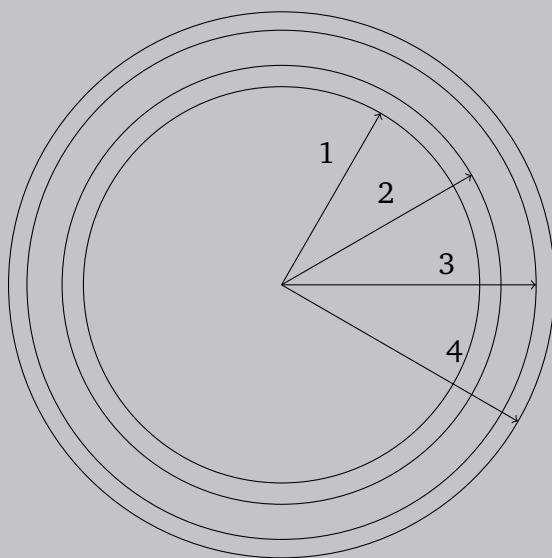
Arrow	Radius (cm)	Material	Source
1	0.43688	Air	17
2	0.48387	Zircaloy	18
3	0.56134	Water	13
4	0.60198	Zircaloy	14

The thimble radii were chosen to be equivalent to the outer thimble radii of control rods and burnable absorber rods by assumption. Note that not all instrument tube positions contain the thimble defined by the first 2 radii in the diagram above, as discussed in Section 2.2.3.3. This pincell does not change at the dashpot.

Figure 7 — Bare Instrument Thimble Pin Geometry
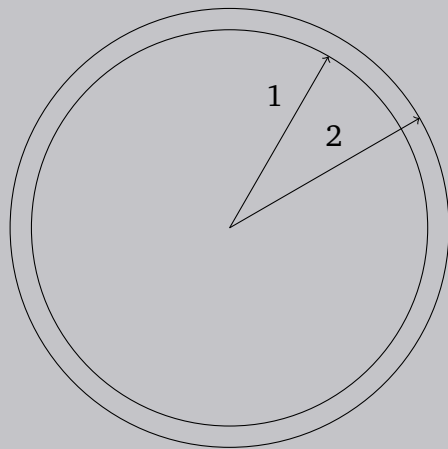
Arrow	Radius (cm)	Material	Source
1	0.43688	Air	17
2	0.48387	Zircaloy	18

The bare instrument thimble for regions below the instrument tube.

Figure 8 — BP Geometry above Dashpot
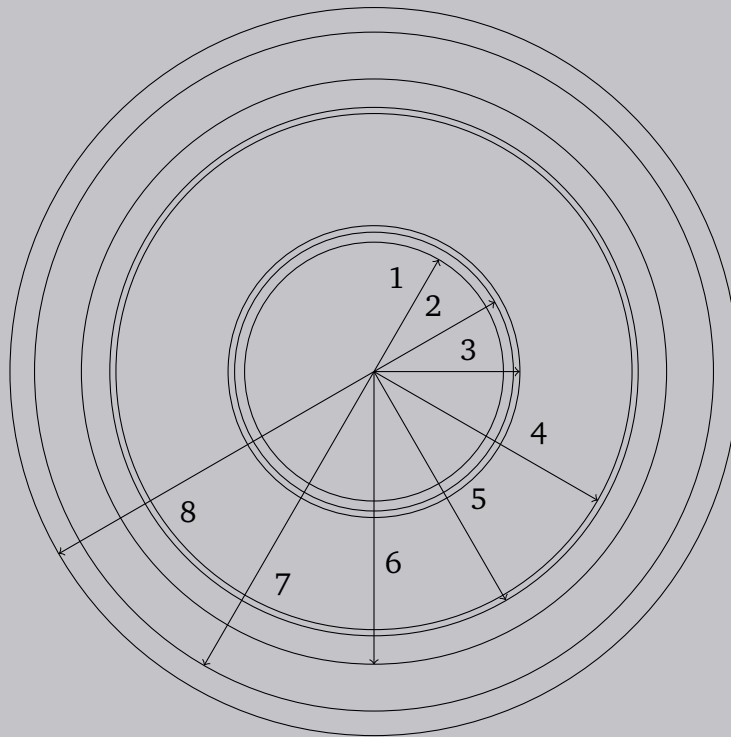
Arrow	Radius (cm)	Material	Source
1	0.21400	Air	19
2	0.23051	SS304	20
3	0.24130	Helium	21
4	0.42672	Borosilicate Glass	22
5	0.43688	Helium	23
6	0.48387	SS304	24
7	0.56134	Water	13
8	0.60198	Zircaloy	14

Figure 9 — BP Plenum Geometry
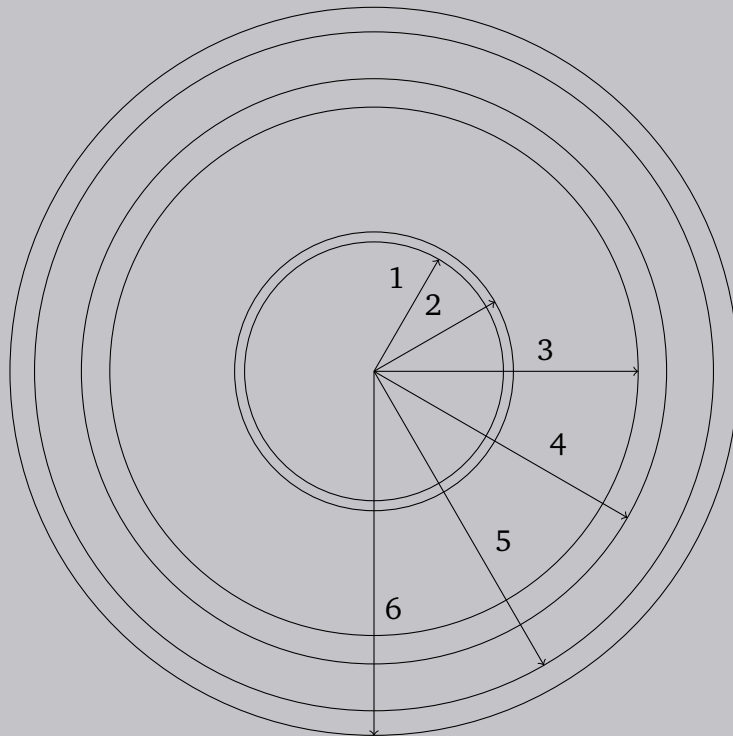
Arrow	Radius (cm)	Material	Source
1	0.21400	Air	19
2	0.23051	SS304	20
3	0.43688	Helium	23
4	0.48387	SS304	24
5	0.56134	Water	13
6	0.60198	Zircaloy	14

Figure 10 — Control Rod Pin Upper Geometry

Arrow	Radius (cm)	Material	Source
1	0.37338	B4C	28
2	0.38608	Helium	25
3	0.48387	SS304	26
4	0.56134	Water	13
5	0.60198	Zircaloy	14
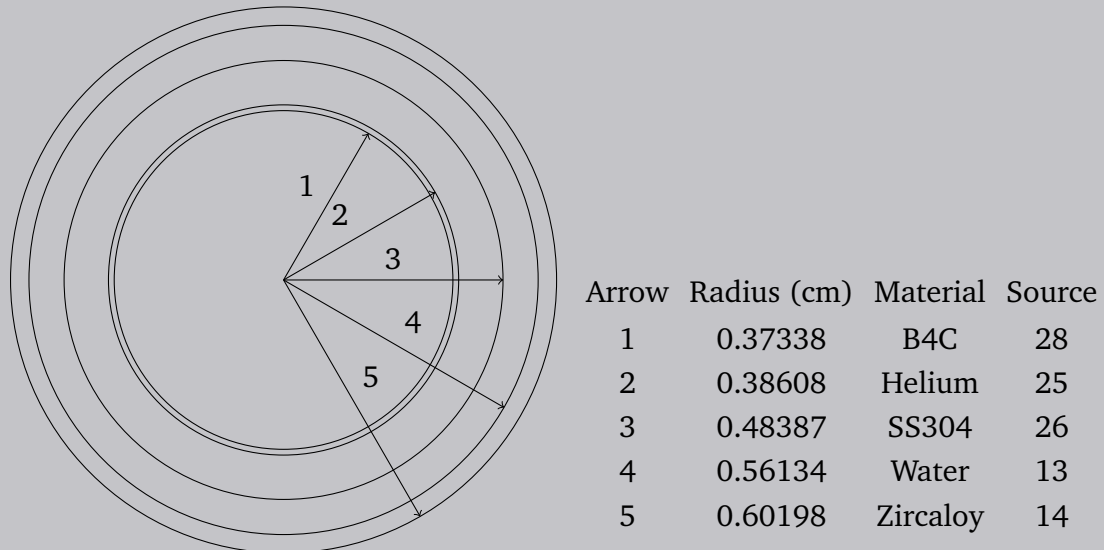
Figure 11 — Control Rod Pin Lower Geometry

Arrow	Radius (cm)	Material	Source
1	0.38227	Ag-In-Cd	27
2	0.38608	Helium	25
3	0.48387	SS304	26
4	0.56134	Water	13
5	0.60198	Zircaloy	14
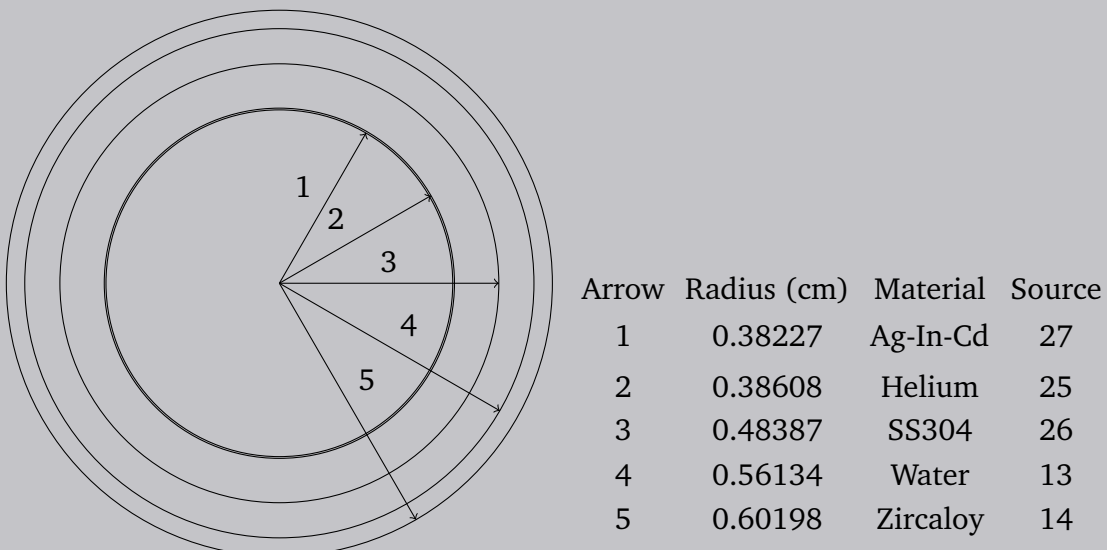
Figure 12 — Control Rod Pin Spacer Geometry
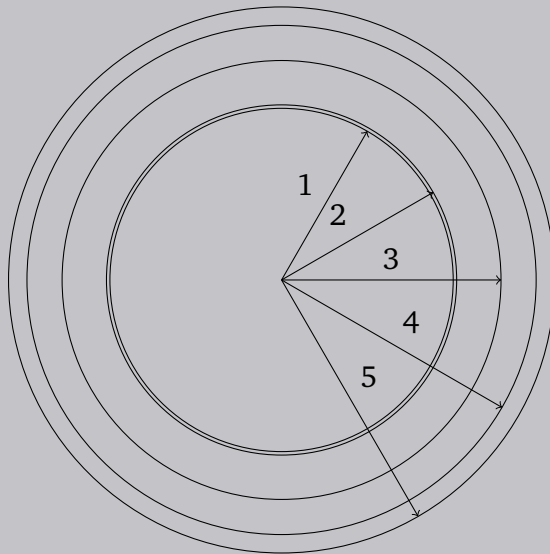
Arrow	Radius (cm)	Material	Source
1	0.37845	SS304	29
2	0.38608	Helium	25
3	0.48387	SS304	26
4	0.56134	Water	13
5	0.60198	Zircaloy	14

Figure 13 — Control Rod Pin Plenum Geometry
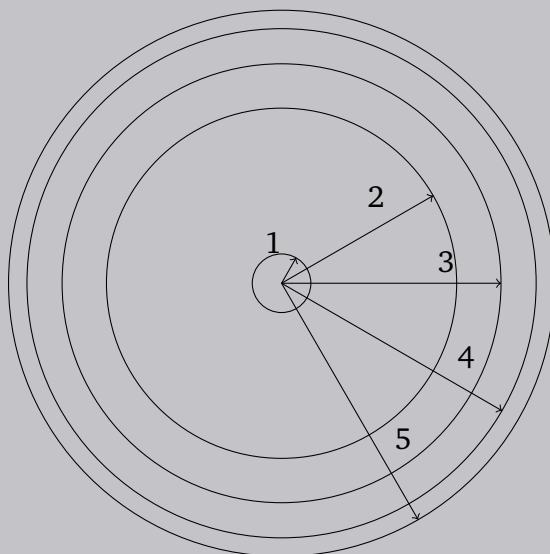
Arrow	Radius (cm)	Material	Source
1	0.06459	Inconel	12
2	0.38608	Helium	25
3	0.48387	SS304	26
4	0.56134	Water	13
5	0.60198	Zircaloy	14

2.2.2   Fuel Assemblies

Each of the assemblies in the core is made up of a 17×17 array of pins described in Section 2.2.1. Table 2 outlines the important parameters of each, and the positions of the guide tubes are shown in Figure 14.

Assemblies are made up of one of three different enrichment fuel pins, and the guide tube positions can be filled with one of several different burnable absorber configurations described in Section 2.2.2.1. For any configuration, the center guide tube may contain an instrument tube. The details of the layout of these features throughout the core are described in Section 2.2.3.

Table 2: Fuel assembly parameters.

		Source
Fuel Assembly Lattice Pitch	21.50364 cm	30
Pin Lattice Pitch	1.25984 cm	31
Pin Lattice Configuration	17×17	4
No. Fuel Rods	264	4
No. Guide Tube Positions	24	4
No. Instrument Tube Positions	1	4
No. Grid Spacers	8	4
Top/Bottom Grid Spacer Material	Inconel 718	4
Top/Bottom Grid Sleeve Material	Stainless Steel 304	4
Intermediate Grid Spacer and Sleeve Material	Zircaloy	4
Weight of Inconel per Top/Bottom Grid	780.273 g	32
Weight of Stainless Steel per Top/Bottom Grid	91.0329 g	34
Weight of Zircaloy per intermediate Grid	1,169.23 g	33
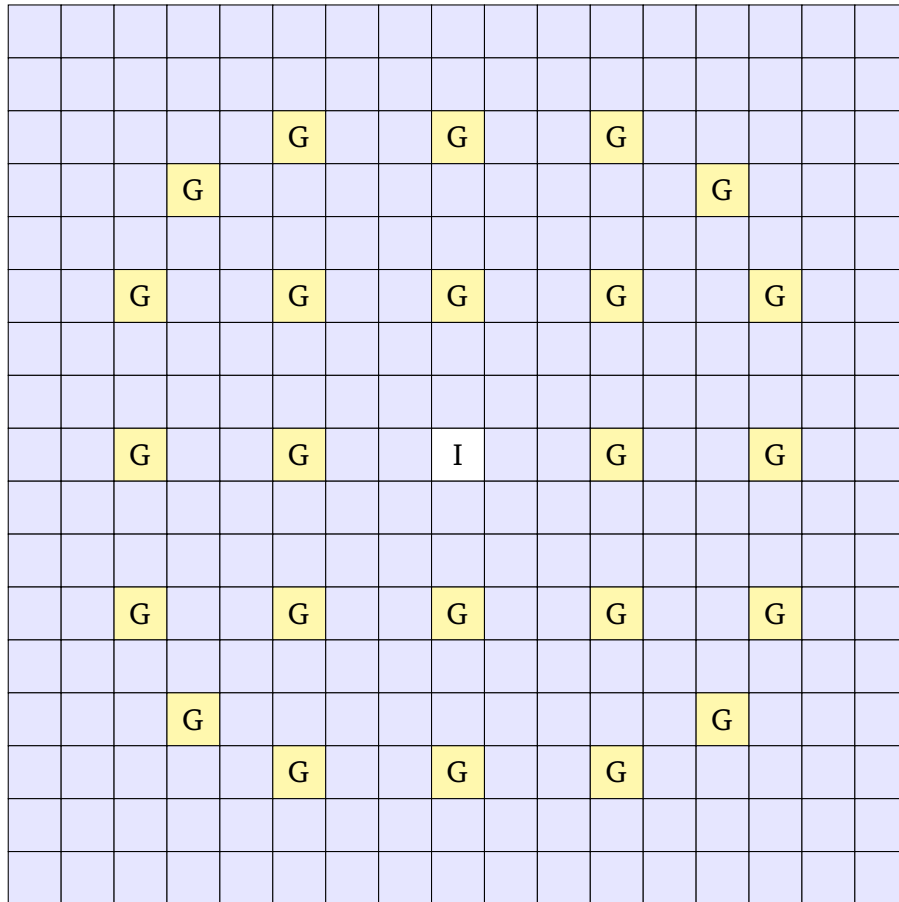
Figure 14: Fuel assembly guide tube locations. Blank locations denote fuel rods, **G** denotes a guide tube location, and **I** denotes a guide tube position that might contain an instrument tube. Source: 35

2.2.2.1 Burnable Absorber Configurations

Assemblies in the core that do not contain control rods may posses one of 5 burnable absorber configurations, or have none at all. Figures 15 through 22 depict these configurations. Each configuration appears in all four quadrants of the core, and thus the 6BA and 5BA configurations need to be rotated as indicated. Note that the 12BA configuration is different between cycle 1 and cycle 2.
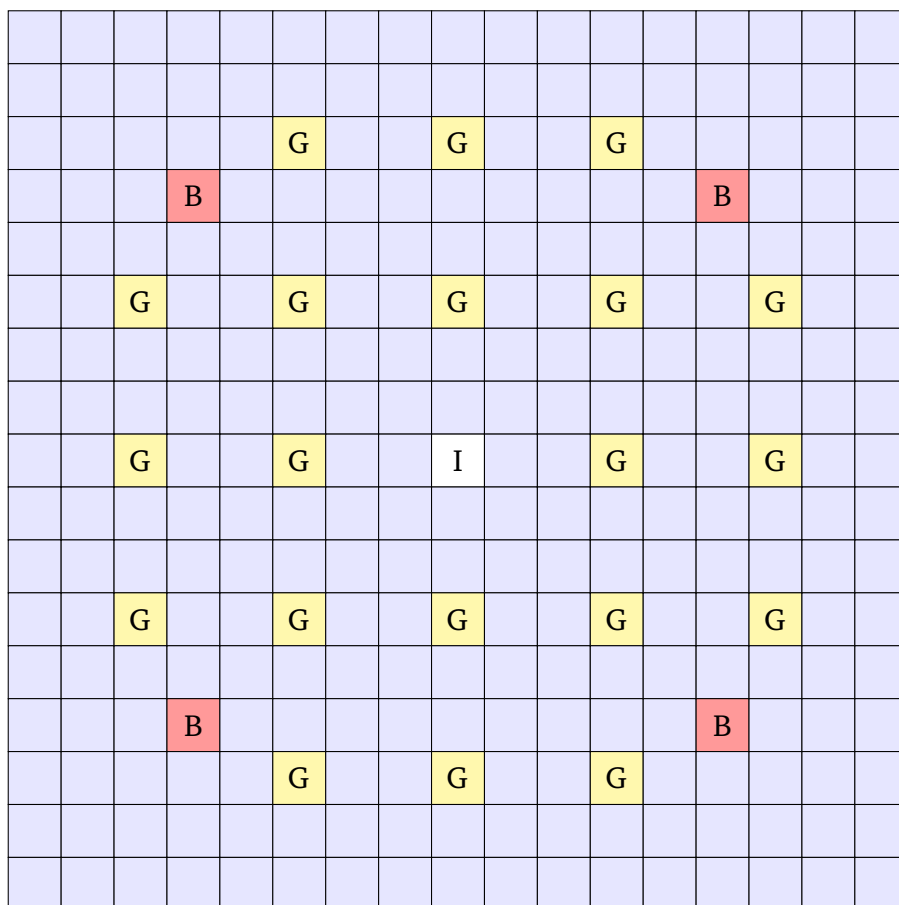
Figure 15: The 4BA burnable absorber configuration. Blank locations denote fuel rods, **G** denotes a guide tube location, **B** denotes a burnable absorber rod, and **I** denotes a guide tube position that might contain an instrument tube. Source: 35
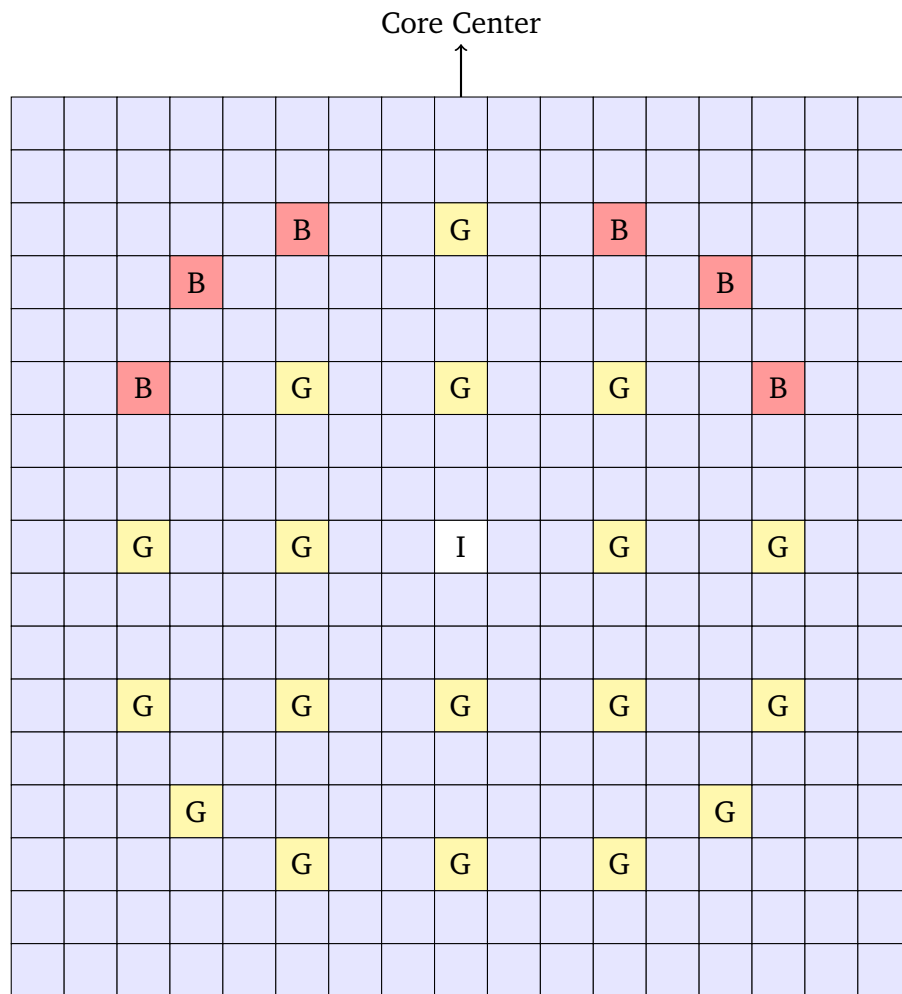
Figure 16: The 6BA burnable absorber configuration. Blank locations denote fuel rods, **G** denotes a guide tube location, **B** denotes a burnable absorber rod, and **I** denotes a guide tube position that might contain an instrument tube. Source: 35
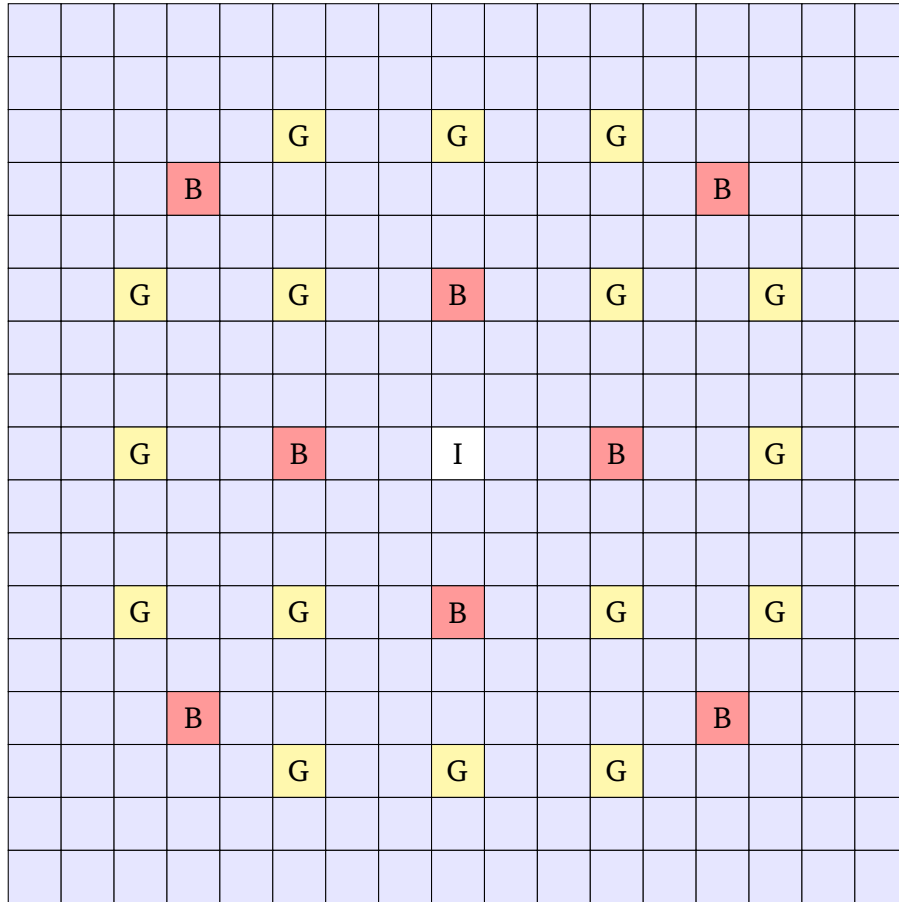
Figure 17: The 8BA burnable absorber configuration. Blank locations denote fuel rods, **G** denotes a guide tube location, **B** denotes a burnable absorber rod, and **I** denotes a guide tube position that might contain an instrument tube. Source: 35
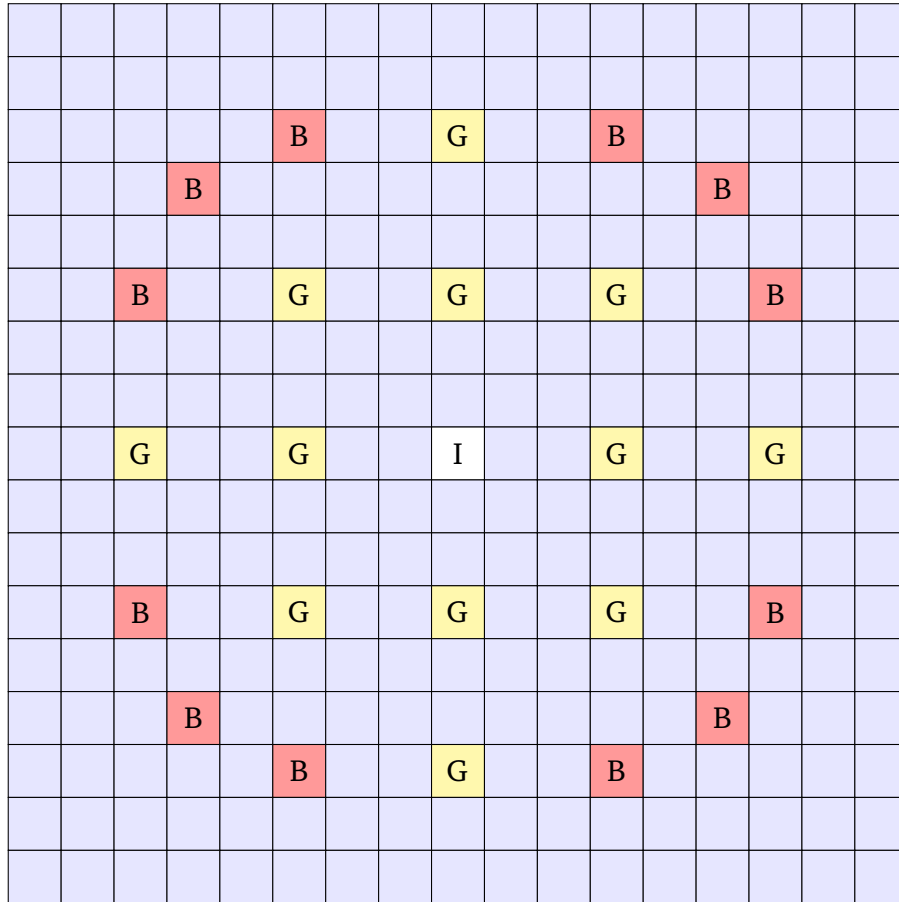
Figure 18: The 12BA burnable absorber configuration for cycle 1. Blank locations denote fuel rods, **G** denotes a guide tube location, **B** denotes a burnable absorber rod, and **I** denotes a guide tube position that might contain an instrument tube. Source: 35
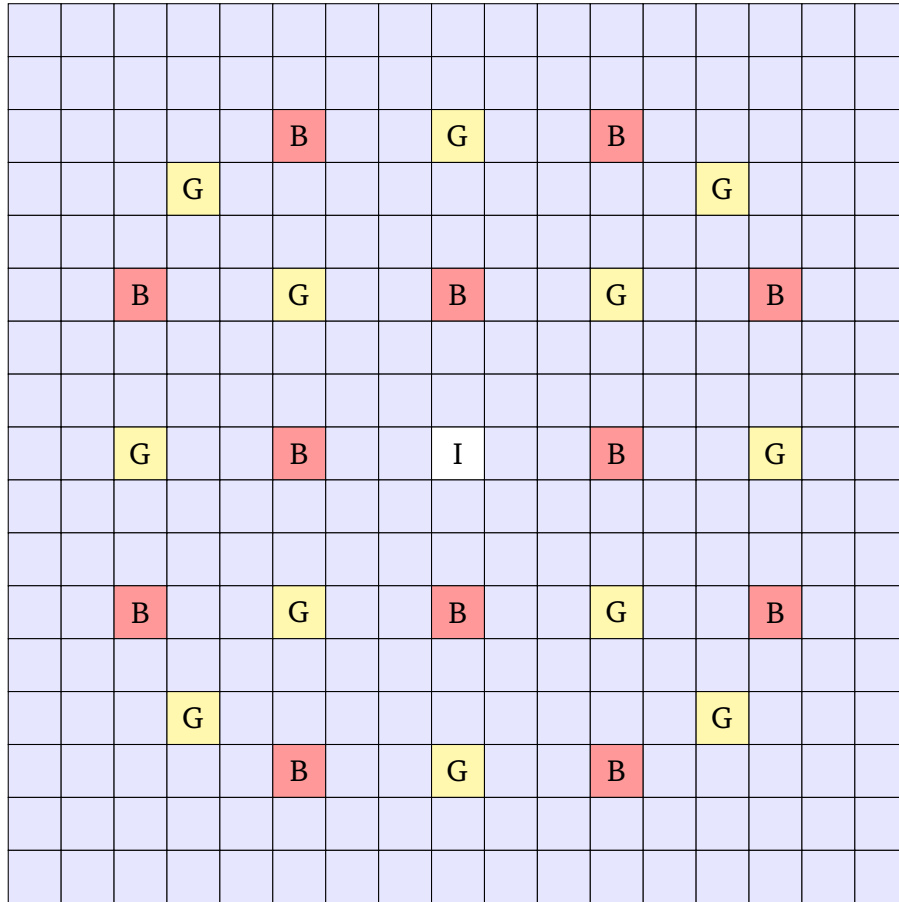
Figure 19: The 12BA burnable absorber configuration for cycle 2. Blank locations denote fuel rods, **G** denotes a guide tube location, **B** denotes a burnable absorber rod, and **I** denotes a guide tube position that might contain an instrument tube. Source: 35

Core Center
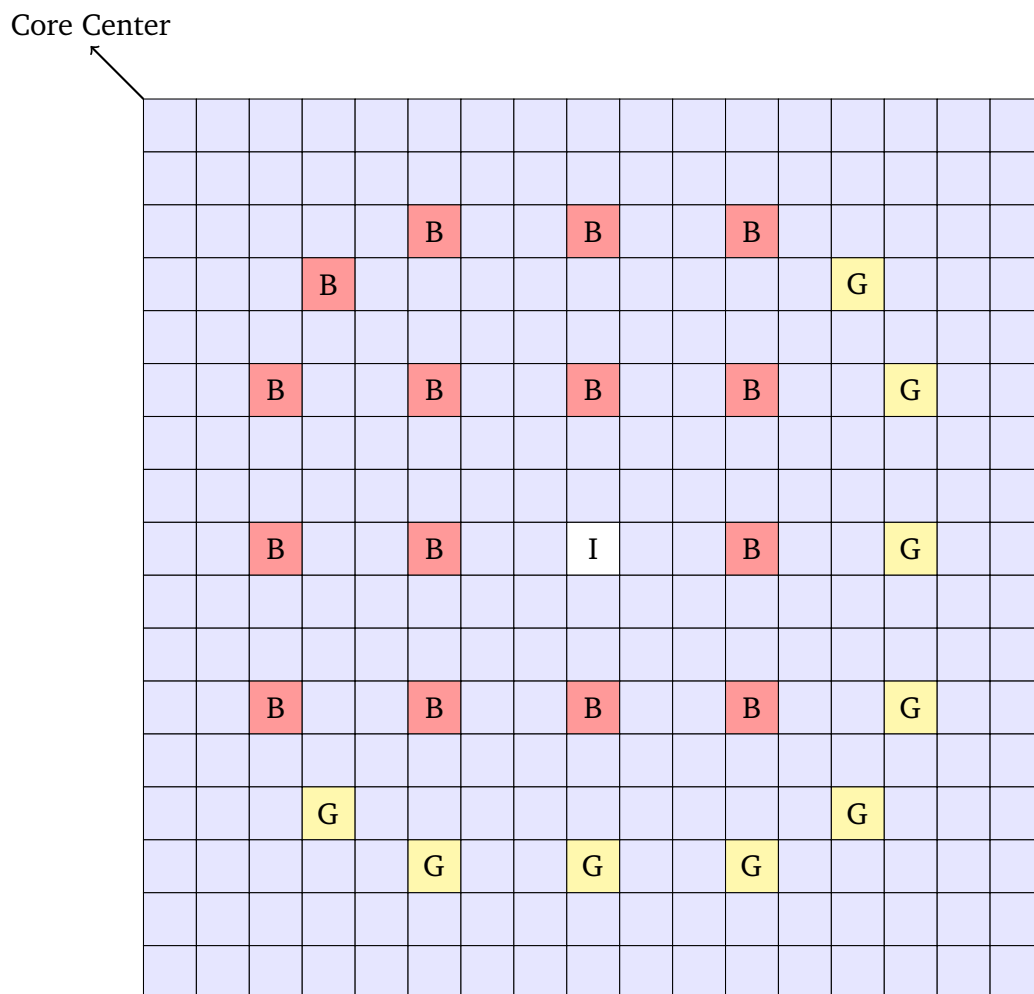
Figure 20: The 15BA burnable absorber configuration. Blank locations denote fuel rods, **G** denotes a guide tube location, **B** denotes a burnable absorber rod, and **I** denotes a guide tube position that might contain an instrument tube. Source: 35
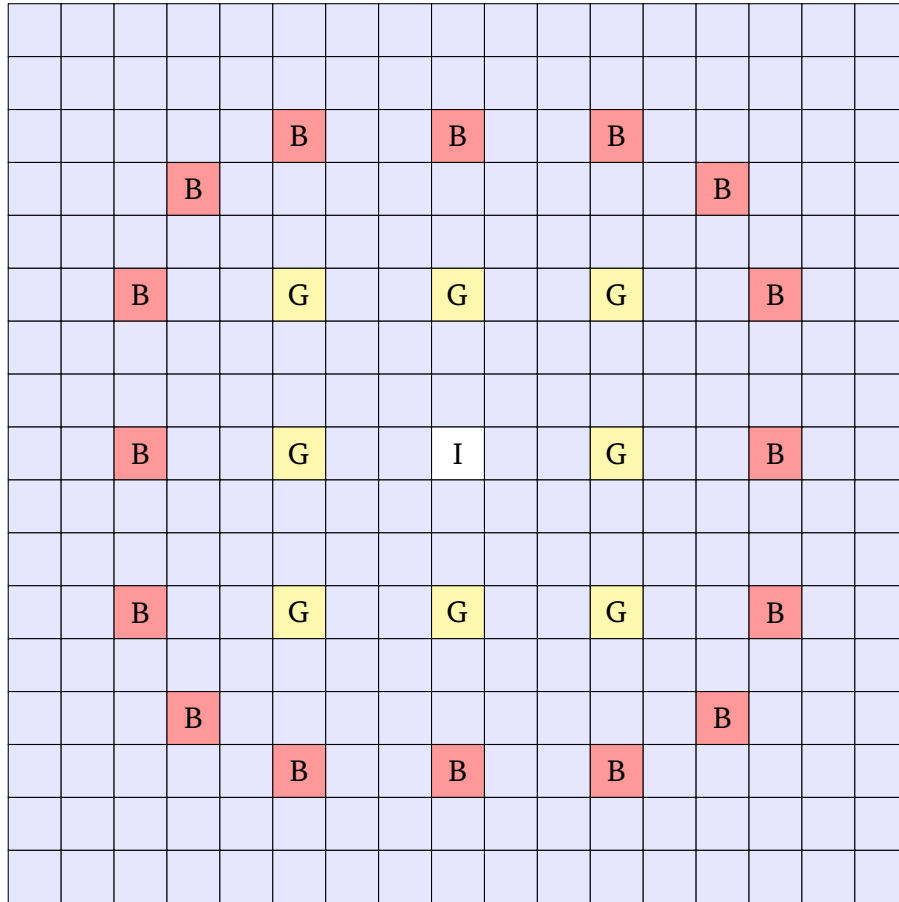
Figure 21: The 16BA burnable absorber configuration. Blank locations denote fuel rods, **G** denotes a guide tube location, **B** denotes a burnable absorber rod, and **I** denotes a guide tube position that might contain an instrument tube. Source: 35
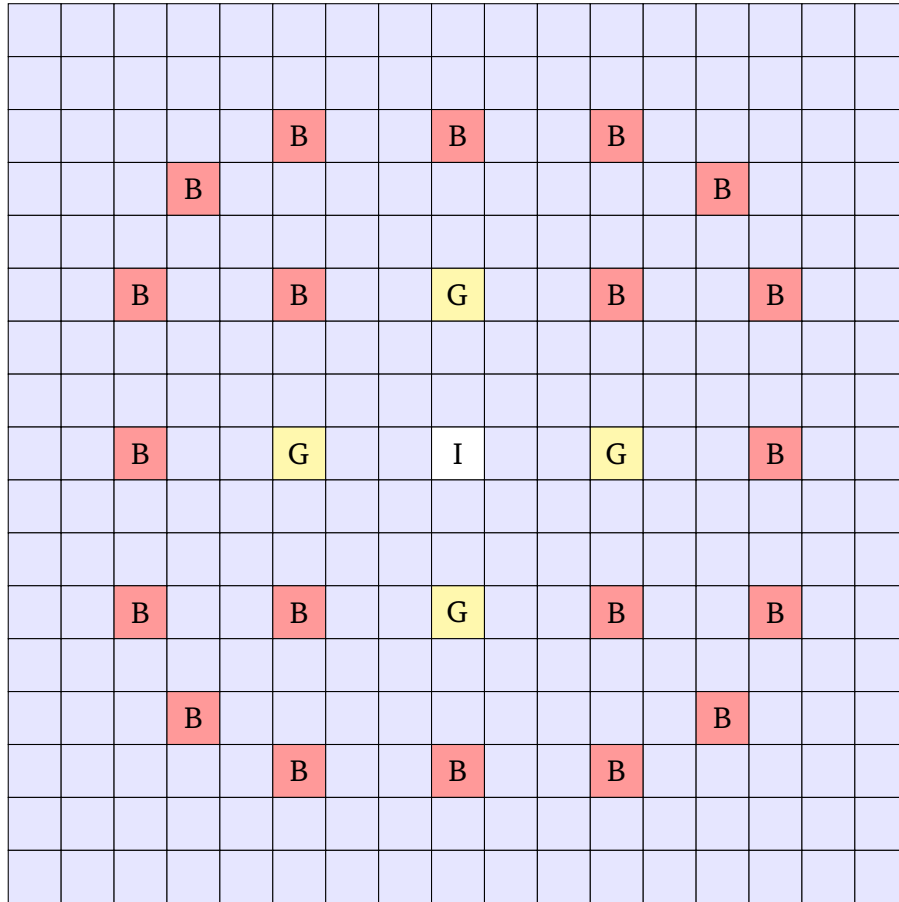
Figure 22: The 20BA burnable absorber configuration. Blank locations denote fuel rods, **G** denotes a guide tube location, **B** denotes a burnable absorber rod, and **I** denotes a guide tube position that might contain an instrument tube. Source: 35

2.2.2.2   Radial Grid Spacer Specifications

In axial regions containing spacers, dimensions are chosen to conserve the total weight of Inconel, Zircaloy, and stainless steel in each grid, as listed in Table 2. The present model creates an egg-crate structure around each pincell as well as a sleeve around assemblies.

The middle six grid spacers consist entirely of Zircaloy while the top and bottom spacers consist of a Stainless Steel 304 (SS304) sleeve with Inconel internal structures. As described in Source 36, for the top/bottom grids the entire mass of the Inconel was distributed evenly among each of the 289 pincells in box of appropriate thickness inside the outer edges of the pincells. Additionally, the stainless steel mass of the grid sleeve was placed in a box of appropriate thickness around the outside of the assembly, fitting inside the region between assemblies. The 6 intermediate grids also consist of both these regions (outer grid sleeve and inner egg-crate), filled with Zircaloy. This was done for a top/bottom grid height of 1.322in and an intermediate grid height of 2.25in, with the same grid sleeve dimensions for each grid type. The inner egg-crate dimensions differ between each grid type.

Figures 23 and 24 show the modified pincell geometry used for the inner grid structure around a fuel pin for each grid type, where the box thicknesses are chosen to conserve mass in the total grid. The same box is also placed around the guide tube pincells for each grid type.

Arrow	Length (cm)	Material	Source
1	0.39218	Fuel	8
2	0.40005	Helium	9
3	0.45720	Zircaloy	10
4	0.61015	Water	36
5	0.62992	Inconel	36
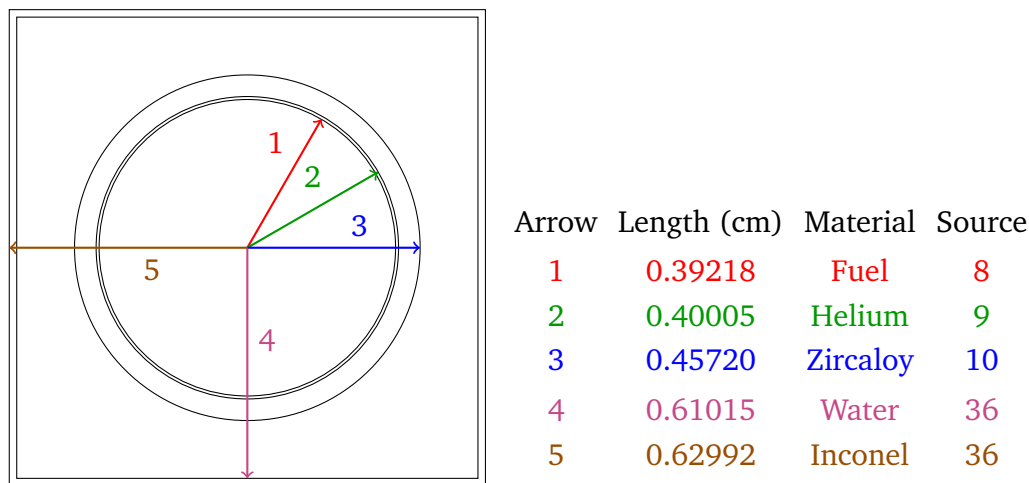
Figure 23: Fuel pincell geometry for the Inconel 718 top/bottom grid spacer inner egg-crate, chosen to have a thickness of 0.0198cm. Source: 36

Figure 25 shows the dimensions of the grid sleeve assemblies in all grid spacer regions. To see what this looks like in combination with the inner structural component in the pincells see Figure 26, which shows an image of what the aggregate grid spacer model looks like to scale.

Arrow	Length (cm)	Material	Source
1	0.39218	Fuel	8
2	0.40005	Helium	9
3	0.45720	Zircaloy	10
4	0.61049	Water	36
5	0.62992	Zircaloy	36
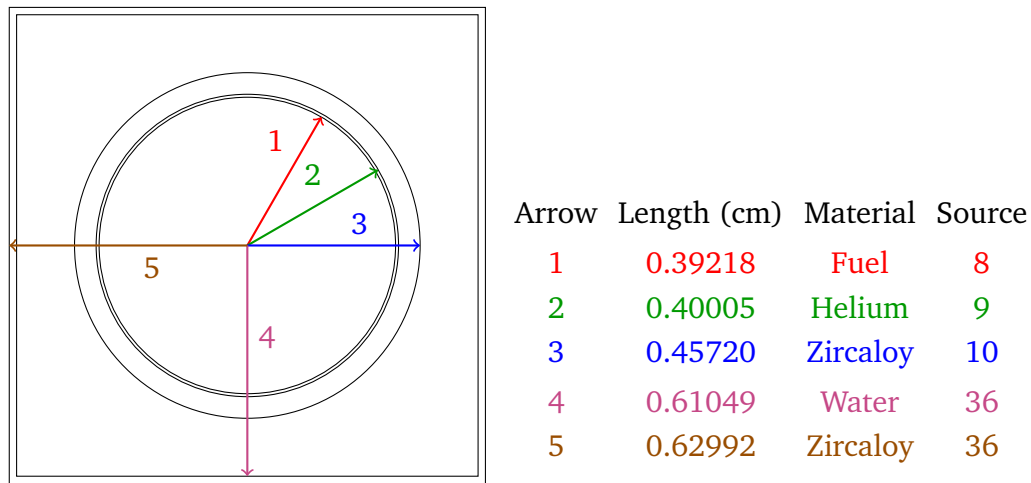
Figure 24: Fuel pincell geometry for the Zircaloy intermediate grid spacer inner egg-crate, chosen to have a thickness of 0.0194cm. Source: 36

Arrow	Length (cm)	Material	Source
1	10.70864	(Assembly)	36
2	10.74798	(Grid Sleeve)	36
3	10.75182	Water	30
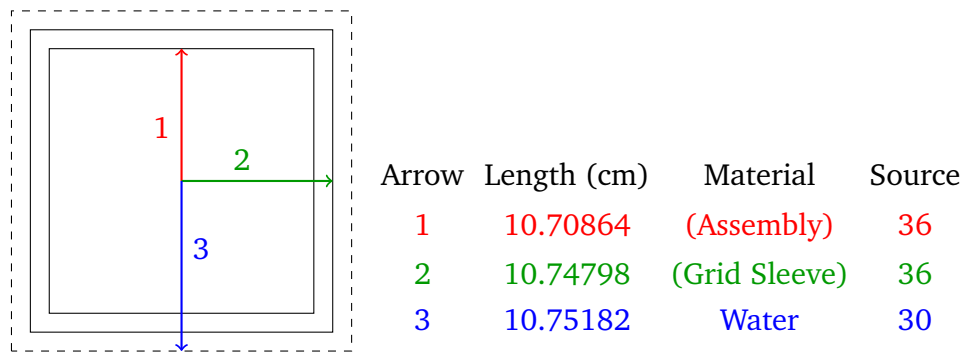
Figure 25: Schematic dimensions of stainless steel grid sleeve. Arrow 1 is the half-width of 17 times the pin lattice pitch; arrow 2 is the outer grid sleeve box half-width; arrow 3 is the outer boundary of the assembly pitch in the overall fuel assembly layout. The grid sleeve thickness was chosen as 0.00384cm to conserve the estimated stainless steel mass. Source: 36
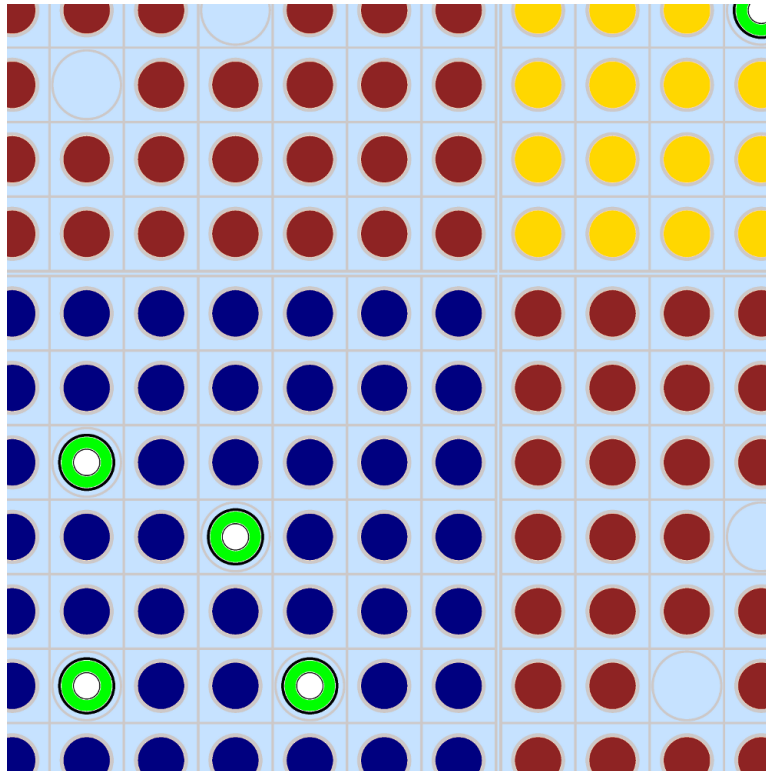
Figure 26: Scale view of an intermediate grid spacer showing inter-assembly spacing at a corner of position J14. Grey is Zircaloy, black is stainless steel, light blue is water, green is burnable absorber, white is air, and dark blue, red and yellow are the three different fuel enrichments.

2.2.3   Core Specification

The remainder of the radial specification is made up of the building blocks defined in the previous sections. Specifically, the main core lattice of fuel assemblies is made up of the previously described fuel assemblies, separated by the fuel assembly lattice pitch specified in Table 2. In addition, specifications for the structural components surrounding the fuel assembly lattice are given in Table 3.

Table 3: Structural component specifications.

		Source
Baffle Width	2.22250 cm	37
Baffle Water Gap	0.1627 cm	41
Baffle Material	Stainless Steel 304	41
Core Barrel IR	187.960 cm	38
Core Barrel OR	193.675 cm	39
Core Barrel Material	Stainless Steel 304	40
Neutron Shield Panel IR	194.840 cm	41
Neutron Shield Panel OR	201.630 cm	41
Neutron Shield Panel Material	Stainless Steel 304	41
Neutron Shield Panel Width	32° at the 45° marks	41
Pressure Vessel Liner IR	219.150 cm	41
Pressure Vessel Liner OR	219.710 cm	41
Pressure Vessel Liner Material	Stainless Steel 304	47
Pressure Vessel IR	219.710 cm	41
Pressure Vessel OR	241.300 cm	41
Pressure Vessel Material	Carbon Steel 508	47

2.2.3.1   Enrichment Zones and Burnable Absorber Positions

The initial cycle 1 fuel assembly loading pattern is shown in Figure 27, including the distribution of enrichments as well as burnable absorber locations. The burnable absorber configurations here are described in Section 2.2.2.1, rotated as appropriate for core symmetry. A scale view of burnable absorber pins depicting these rotations is shown in Figure 28.

Figure 29 shows the shuffling pattern for cycle 2, which includes 64 fresh assemblies and a different burnable absorber pattern.
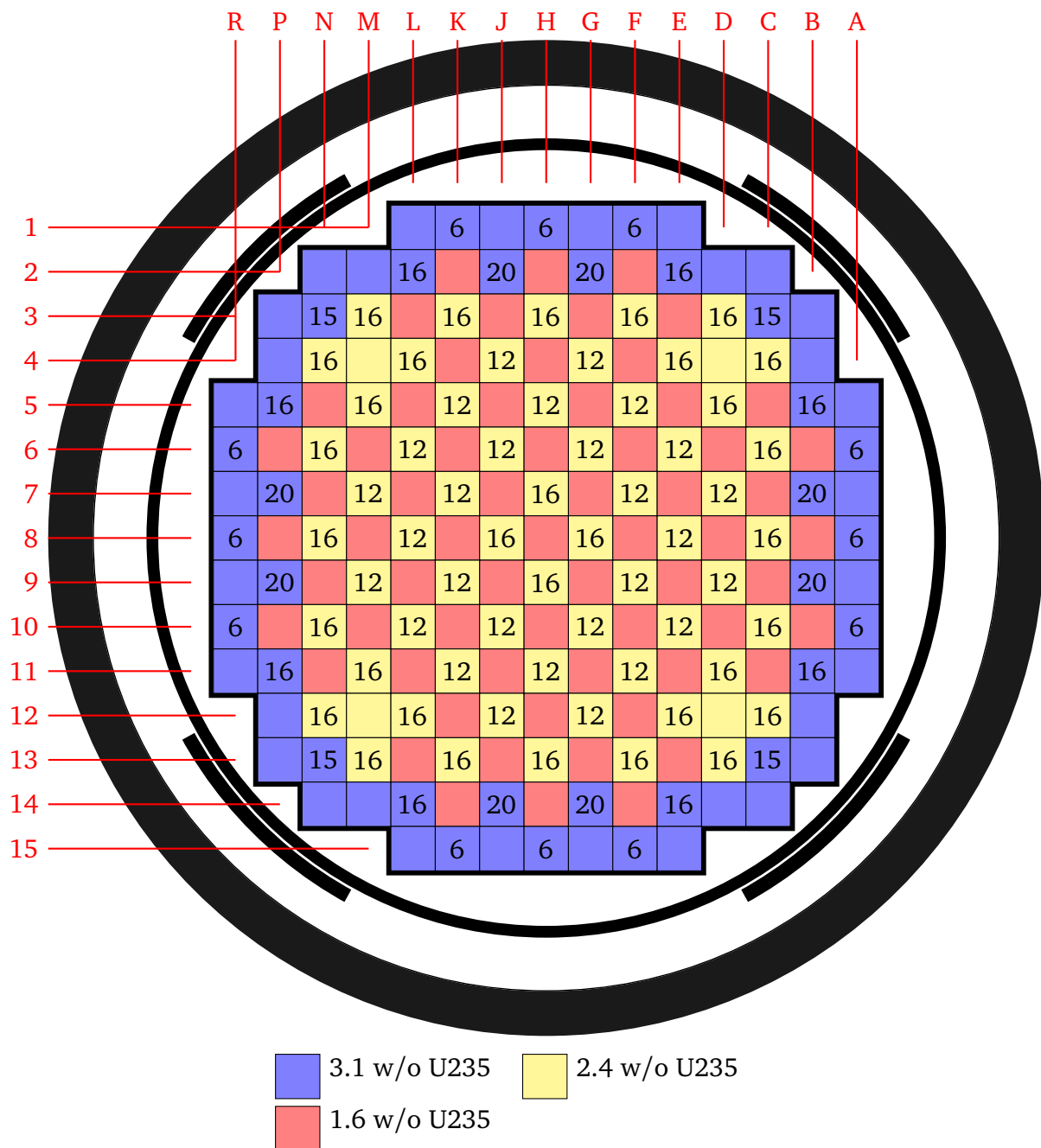
Figure 27: Layout of fuel assemblies showing enrichment loading pattern and burnable absorber positions in cycle 1. Source: 1
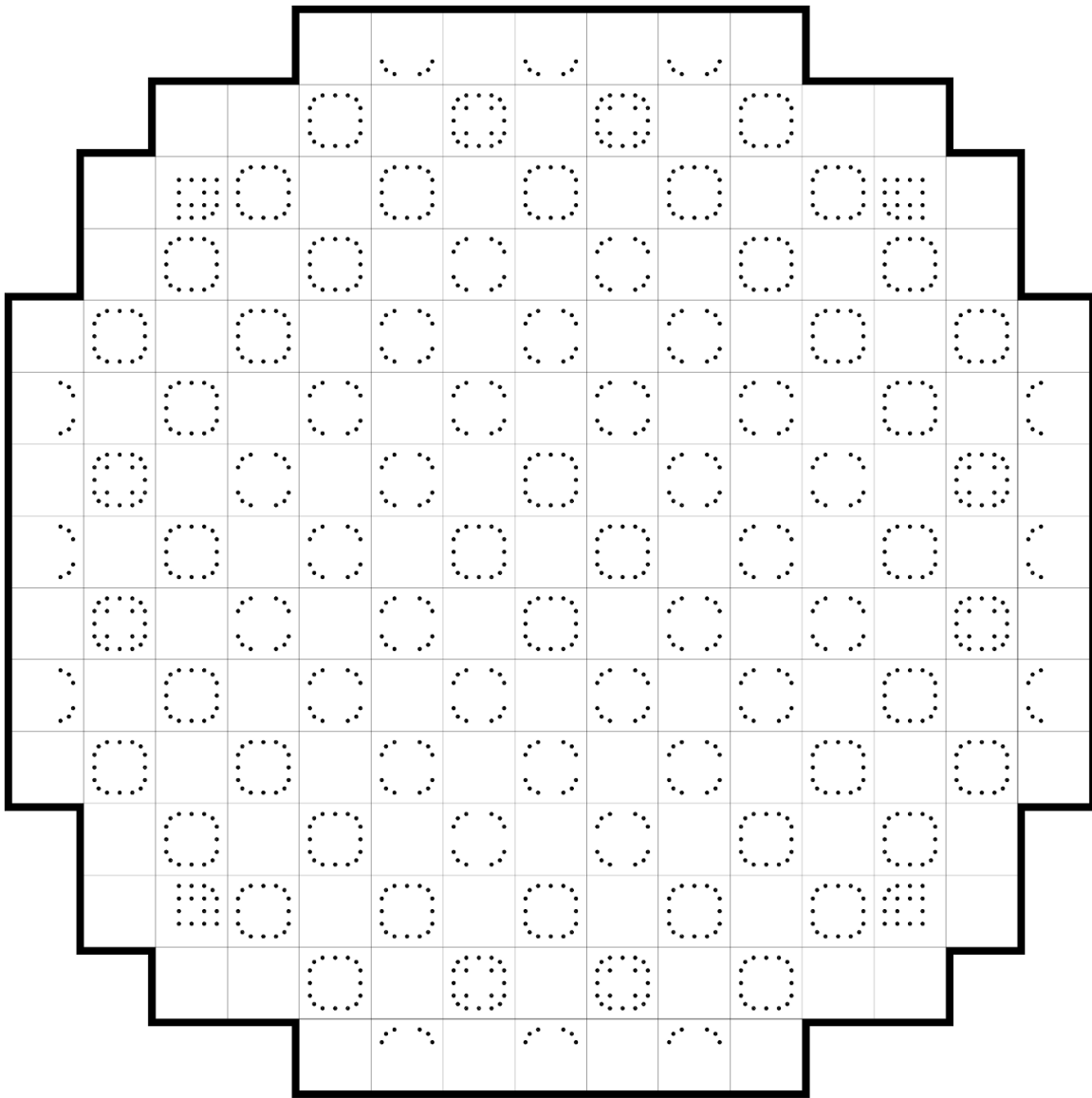
Figure 28: Detailed scale view of burnable absorber pins in cycle 1, showing proper rotations.
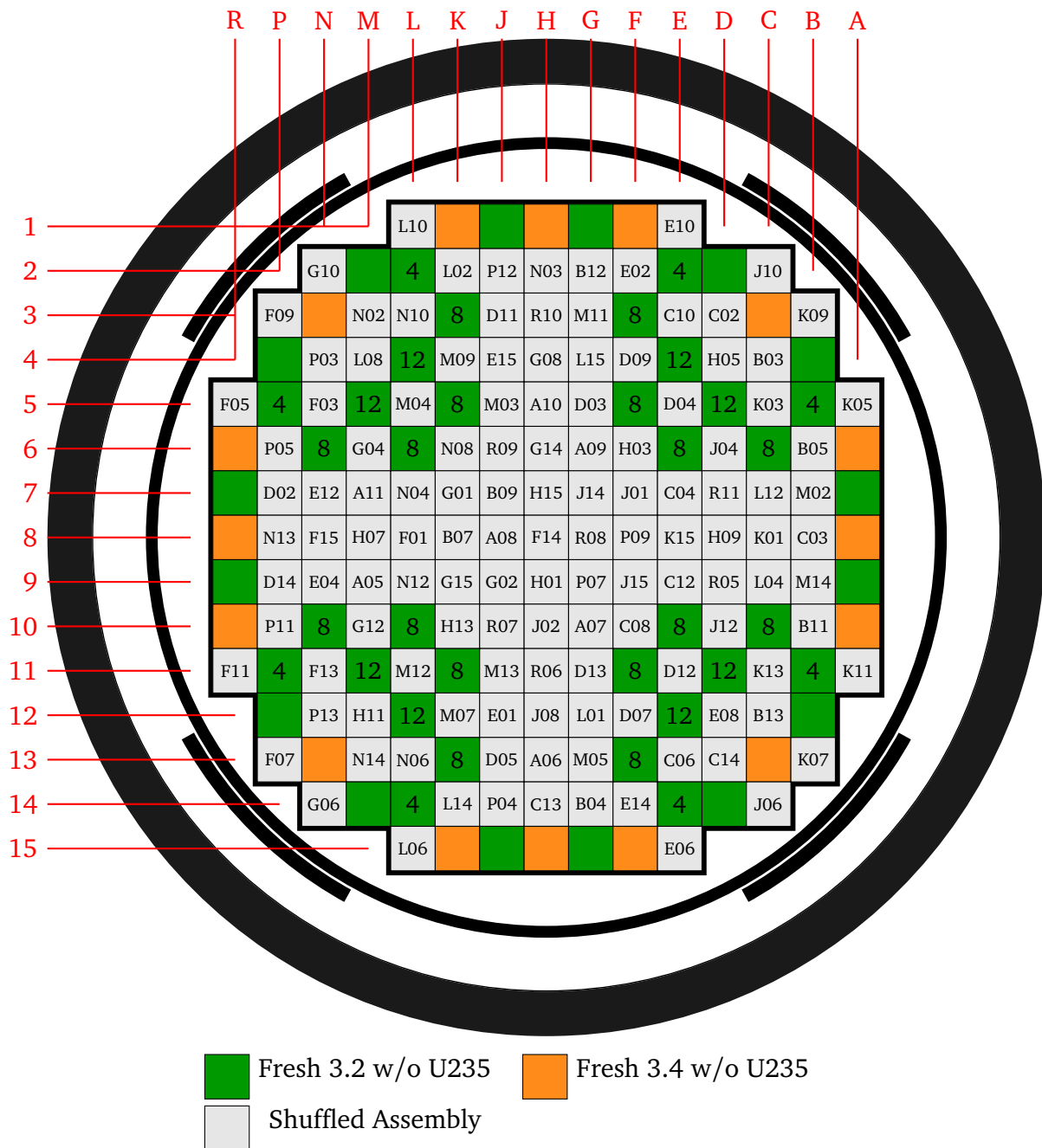
Figure 29: Cycle 2 shuffling pattern, burnable absorber positions, and enrichment loading pattern of fresh assemblies. Sources: 1, 2

2.2.3.2 Control Rod Bank Positions

Each of the four control rod banks - specified by the identifiers A, B, C, and D - are made up of several control rod clusters in multiple fuel assemblies. In control rod clusters, every guide tube is filled with the control rod pincell described in section 2.2.1, with the exception of the center tube. Each of the clusters in a given control rod bank move together.

In addition to the control rod banks, 5 shutdown banks of control rod clusters are included above the core - specified by S_A, S_B, S_C, S_D, and S_E. These clusters are not used in normal operation, however, their reactivity worth was measured and reported in Table 22.

Figure 30 shows the radial locations of control rod clusters belonging to each control rod and shutdown bank. The axial specifications of each are described later in Section 2.3.5.

The positions of control rod banks do not change between cycle 1 and cycle 2.
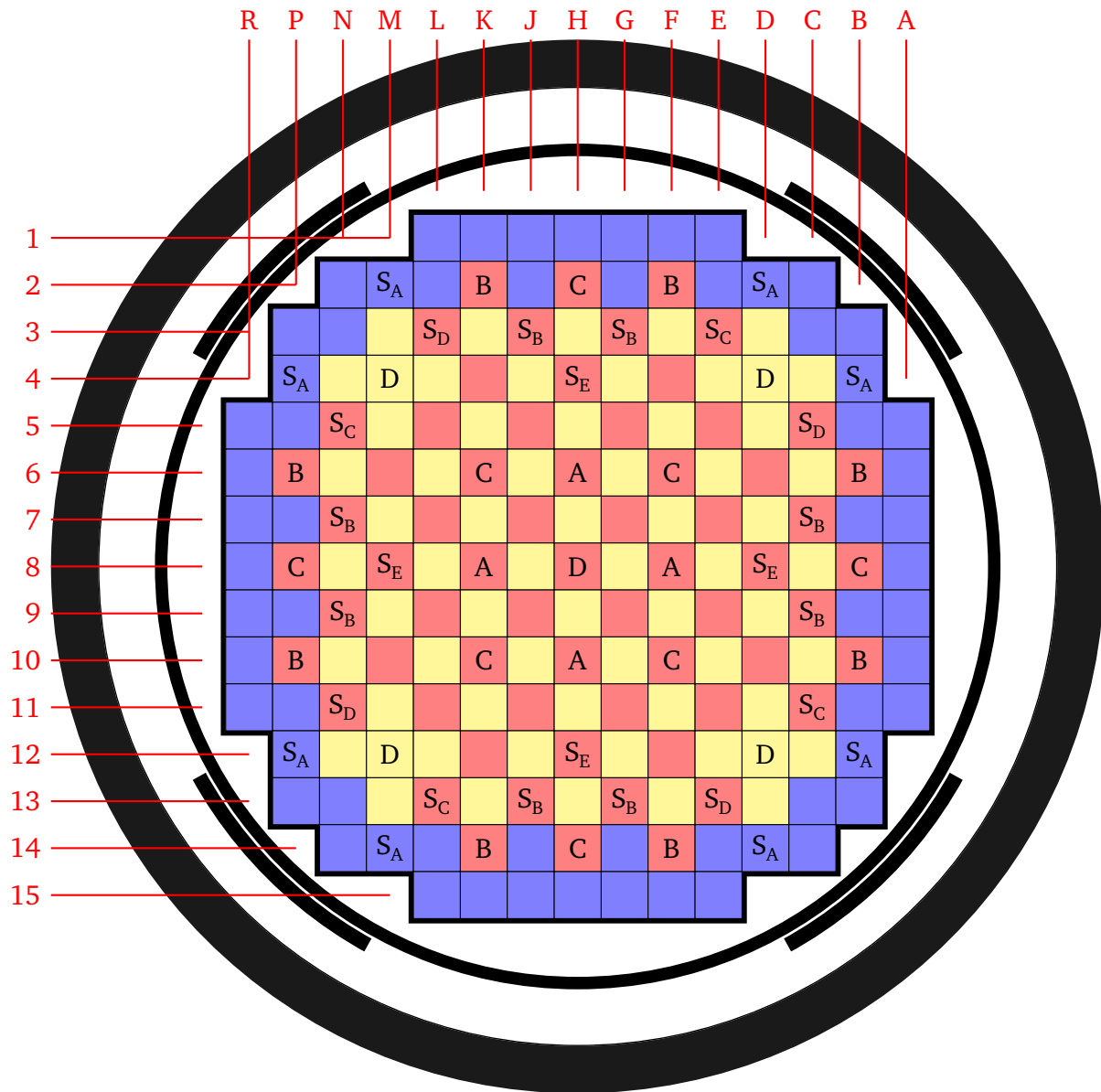
Figure 30: Control rod and shutdown bank positions. Source: 1

2.2.3.3 Instrument Tube Positions

The central guide tube for many fuel assemblies in the core is filled by an instrument tube, as described in Section 2.2.1. Figure 31 shows these positions. Where not indicated, the central guide tube is filled with water, as described in section 2.2.1.

The positions of instrument tubes do not change between cycle 1 and cycle 2.
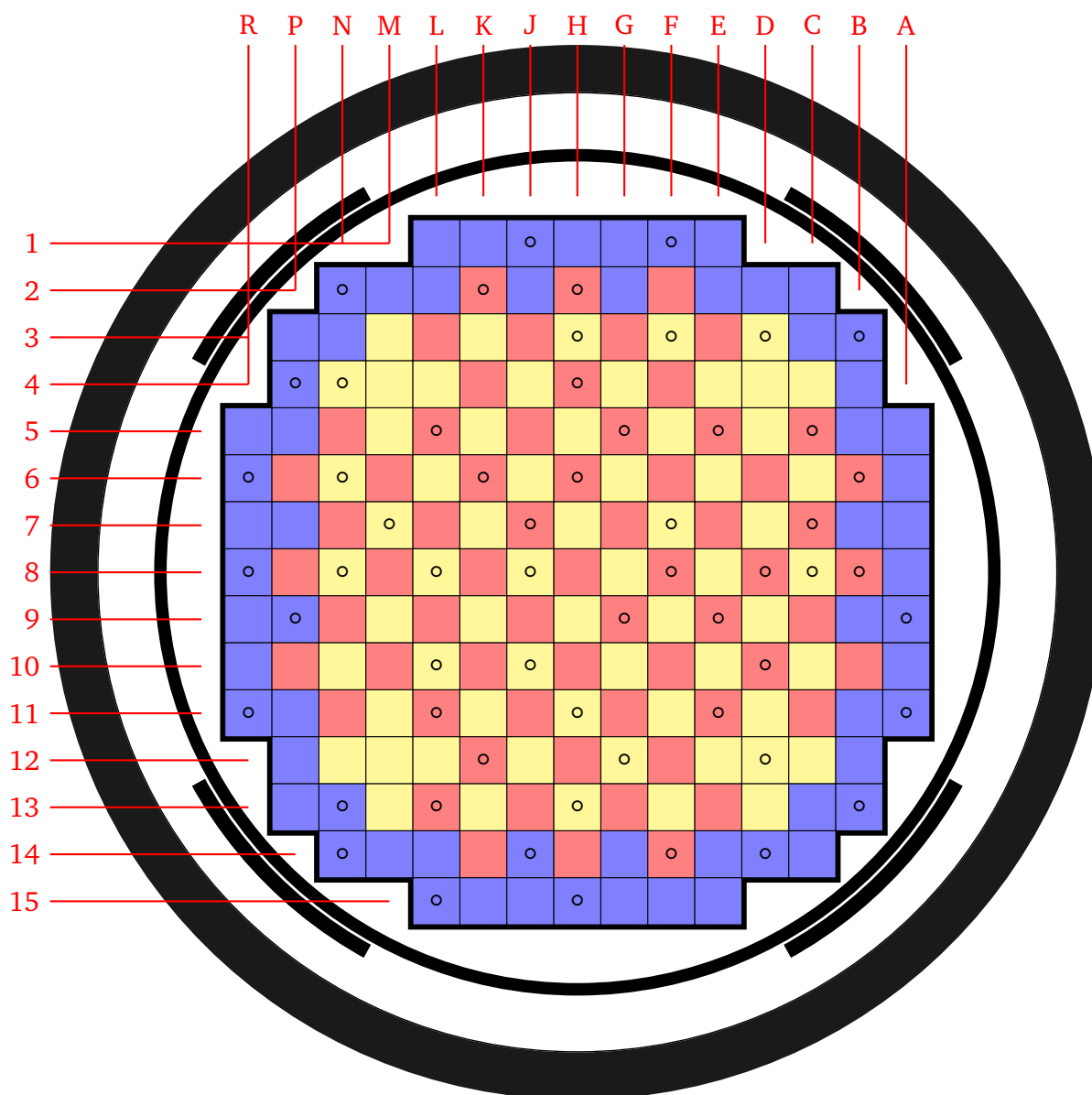
Figure 31: Instrument tube positions. Source: 48

2.3   Axial Geometry

While some of the previously-described radial features are uniform along the entire height of the model, many have several different axial zones. For instance, the models of the baffle, core barrel, neutron shield panels, and reactor pressure vessel do not change axially, in contrast to the pincells that make up the fuel assemblies. As presented in the following sections, the axial zones are treated at the pincell level to facilitate easier modelling, since the boundaries for the axial zones for each pincell type are not all at the same planes. With this type of definition, the final aggregate geometry inside the core barrel need only consist of the fuel assemblies, which are made up of only the inter-assembly gridstraps and the pincells that are defined for the entire axial extent.

2.3.1   Fuel Rods

Figure 32 shows all different axial sections used in the fuel rod pincell occupying each fuel position in the assemblies. In most places the pincells described in Section 2.2.1 are used, however where indicated the pincell is filled either entirely with water, or with solid pins of either stainless steel or Zircaloy. These solid pins use the outer-most radius of the regular fuel rod pincell.

Source Reference		Elevation (cm)	Description
		— 460.000	Highest Extent
46	Water	— 431.876	Top of Upper Nozzle
46	Nozzle / Support Plate Stainless Steel	— 423.049	Bottom of Upper Nozzle
47	Water	— 419.704	Top of Fuel Rod
47	Zircaloy Pin	— 417.164	Top of Fuel Rod Plenum
47	Fuel Rod Plenum Pincell	— 415.164	Grid 8 Top
36	Fuel Rod Plenum Pincell w/ Grid	— 411.806	Grid 8 Bottom
47	Fuel Rod Plenum Pincell	— 402.508	Top of Active Fuel
5	Fuel Rod Pincell	— 364.725	Grid 7 Top
36	Fuel Rod Pincell w/ Grid	— 359.010	Grid 7 Bottom
5	Fuel Rod Pincell	— 312.528	Grid 6 Top
36	Fuel Rod Pincell w/ Grid	— 306.813	Grid 6 Bottom
5	Fuel Rod Pincell	— 260.331	Grid 5 Top
36	Fuel Rod Pincell w/ Grid	— 254.616	Grid 5 Bottom
5	Fuel Rod Pincell	— 208.134	Grid 4 Top
36	Fuel Rod Pincell w/ Grid	— 202.419	Grid 4 Bottom
5	Fuel Rod Pincell	— 155.937	Grid 3 Top
36	Fuel Rod Pincell w/ Grid	— 150.222	Grid 3 Bottom
5	Fuel Rod Pincell	— 103.740	Grid 2 Top
36	Fuel Rod Pincell w/ Grid	— 98.0250	Grid 2 Bottom
5	Fuel Rod Pincell	— 40.5200	Grid 1 Top
36	Fuel Rod Pincell w/ Grid	— 37.1621	Grid 1 Bottom
5	Fuel Rod Pincell	— 36.7480	Bottom of Active Fuel
47	Zircaloy Pin	— 35.0000	Bottom of Fuel Rod
66	Nozzle / Support Plate Stainless Steel	— 20.0000	Bottom of Support Plate
	Water	— 0.00000	Lowest Extent

Figure 32: Fuel rod pincell axial specification.

2.3.2   Guide Tubes

Figure 33 shows the empty guide tube axial differentiation, referring to the pincells described in Section 2.2.1. As with the fuel rods, the pincell is replaced by water below the fuel region.

Source Reference		Elevation (cm)	Description
46	Water		
		431.876	Top of Upper Nozzle
46	Nozzle / Support Plate Borated Water		
		423.049	Bottom of Upper Nozzle
44	Guide Tube Pincell		
		415.164	Grid 8 Top
36	Guide Tube Pincell w/ Grid		
		411.806	Grid 8 Bottom
44	Guide Tube Pincell		
		364.725	Grid 7 Top
36	Guide Tube Pincell w/ Grid		
		359.010	Grid 7 Bottom
44	Guide Tube Pincell		
		312.528	Grid 6 Top
36	Guide Tube Pincell w/ Grid		
		306.813	Grid 6 Bottom
44	Guide Tube Pincell		
		260.331	Grid 5 Top
36	Guide Tube Pincell w/ Grid		
		254.616	Grid 5 Bottom
44	Guide Tube Pincell		
		208.134	Grid 4 Top
36	Guide Tube Pincell w/ Grid		
		202.419	Grid 4 Bottom
44	Guide Tube Pincell		
		155.937	Grid 3 Top
36	Guide Tube Pincell w/ Grid		
		150.222	Grid 3 Bottom
44	Guide Tube Pincell		
		103.740	Grid 2 Top
36	Guide Tube Pincell w/ Grid		
		98.0250	Grid 2 Bottom
44	Guide Tube Pincell		
		40.5200	Grid 1 Top
36	Guide Tube Pincell w/ Grid		
		39.9580	Control Rod Step 0
44	Dashpot Guide Tube w/ Grid		
		37.1621	Grid 1 Bottom
44	Dashpot Guide Tube		
		35.0000	Bottom of Fuel Rod
66	Nozzle / Support Plate Borated Water		
		20.0000	Bottom of Support Plate
	Water		
		0.00000	Lowest Extent

Figure 33: Empty guide tube pincell axial specification.

2.3.3   Instrument Tubes

Figure 34 shows the instrument tube axial differentiation, referring to the pincells described in Section 2.2.1. This follows the same pattern as the guide tube axial specification, with the caveat that below the fuel region the inner section of the instrument tubes (that is, without the surrounding guide tube) is used through the lowest extent of the geometry. Also note that regardless of whether or not the central instrument tube contains the inner instrument thimble, the outer guide tube does not shrink for the dashpot.

Source Reference		Elevation (cm)	Description
		460.000	Highest Extent
46	Water	423.049	Bottom of Upper Nozzle
42	Instr. Tube Pincell	415.164	Grid 8 Top
36	Instr. Tube Pincell w/ Grid	411.806	Grid 8 Bottom
42	Instr. Tube Pincell	364.725	Grid 7 Top
36	Instr. Tube Pincell w/ Grid	359.010	Grid 7 Bottom
42	Instr. Tube Pincell	312.528	Grid 6 Top
36	Instr. Tube Pincell w/ Grid	306.813	Grid 6 Bottom
42	Instr. Tube Pincell	260.331	Grid 5 Top
36	Instr. Tube Pincell w/ Grid	254.616	Grid 5 Bottom
42	Instr. Tube Pincell	208.134	Grid 4 Top
36	Instr. Tube Pincell w/ Grid	202.419	Grid 4 Bottom
42	Instr. Tube Pincell	155.937	Grid 3 Top
36	Instr. Tube Pincell w/ Grid	150.222	Grid 3 Bottom
42	Instr. Tube Pincell	103.740	Grid 2 Top
36	Instr. Tube Pincell w/ Grid	98.0250	Grid 2 Bottom
42	Instr. Tube Pincell	40.5200	Grid 1 Top
36	Instr. Tube Pincell w/ Grid	37.1621	Grid 1 Bottom
42	Instr. Tube Pincell	35.0000	Bottom of Fuel Rod
66	Support Plate / Nozzle Borated Water	20.0000	Bottom of Support Plate
42	Bare Instr. Tube	0.00000	Lowest Extent

Figure 34: Instrument tube pincell axial specification.

2.3.4   Burnable Absorbers

Figure 35 shows the axial regions of the burnable absorber pincells. Here, the active region of burnable absorber rods as presented in Section 2.2.1 extend from a plane a few inches above the bottom of the active fuel to a plane just below the top of the active fuel region. Above there, the outermost inner radius of the burnable absorber rods (or arrow 6 in Figure 8) is used to create a solid stainless steel pin tube through the top of the upper nozzle, inside the guide tube where appropriate.

Source Reference		Elevation (cm)	Description
		460.000	Highest Extent
46	Water	431.876	Top of Upper Nozzle
43	Stainless Steel Pin	423.049	Bottom of Upper Nozzle
43	Stainless Steel Pin in GT	421.532	Top of BPRA Rod Plenum
43	BPRA Rod Upper Plenum Pincell	415.164	Grid 8 Top
36	BPRA Rod Plenum Pincell w/ Grid	411.806	Grid 8 Bottom
43	BPRA Rod Plenum Pincell	401.238	Top of Active Absorber
43	Burnable Absorber Pincell	364.725	Grid 7 Top
36	Burnable Absorber Pincell w/ Grid	359.010	Grid 7 Bottom
43	Burnable Absorber Pincell	312.528	Grid 6 Top
36	Burnable Absorber Pincell w/ Grid	306.813	Grid 6 Bottom
43	Burnable Absorber Pincell	260.331	Grid 5 Top
36	Burnable Absorber Pincell w/ Grid	254.616	Grid 5 Bottom
43	Burnable Absorber Pincell	208.134	Grid 4 Top
36	Burnable Absorber Pincell w/ Grid	202.419	Grid 4 Bottom
43	Burnable Absorber Pincell	155.937	Grid 3 Top
36	Burnable Absorber Pincell w/ Grid	150.222	Grid 3 Bottom
43	Burnable Absorber Pincell	103.740	Grid 2 Top
36	Burnable Absorber Pincell w/ Grid	98.0250	Grid 2 Bottom
43	Burnable Absorber Pincell	40.5580	Bottom of Active Absorber
43	Stainless Steel Pin in GT	40.5200	Grid 1 Top
43	SS Pin in GT w/ Grid	39.9580	Control Rod Step 0
43	SS Pin in Dashpot GT w/ Grid	38.6600	Bot. of BPRA Rod
36	Dashpot Guide Tube w/ Grid	37.1621	Grid 1 Bottom
44	Dashpot Guide Tube	35.0000	Bottom of Fuel Rod
66	Support Plate / Nozzle Borated Water	20.0000	Bottom of Support Plate
	Water	0.00000	Lowest Extent

Figure 35: Burnable absorber pincell axial specification.

2.3.5 Control Rods

Figure 36 shows the control rod axial layout, which depending on the degree of insertion can either be occupied by the empty guide tube pincell or the control rod pincell described in Section 2.2.1. The details of insertion depend on the radial location of the specific control rod cluster, i.e. which control or shutdown bank it belongs to. Unlike the other axial descriptions in this section, Figure 36 presents the axial sections *only* for the control rod thimble that fits inside the guide tube. It is presented for the fully-inserted position; all intermediate planes should be shifted according to the number of steps withdrawn, and the appropriate axial sections created in combination with the surrounding guide tube and grid spacer pincell.

In this model, when fully-inserted the top of the upper control rod active absorber region should be flush with the top of the active fuel region. Control rods are considered to be withdrawn in 228 "steps" until the active region is drawn completely out of the active fuel region. When withdrawn 228 steps, the bottom of the lower control rod active absorber region should be flush with the top of the active fuel region. The total height of the lower and upper control rod regions is 360.68 cm, meaning the step height is 1.58193 cm.

The actual axial planes used depend on the the number of steps of insertion of the rod, and may be superseded by the highest axial plane when appropriate. In other words, the planes presented in Figure 36 should be shifted upwards by the number of steps withdrawn times the step height.

The control and shutdown banks can have any level of partial insertion, where the bottom tips of the rods can be at any axial step level between step 0 and step 228. While each of these banks move their control rod clusters together, their movement is often staggered with the other control rod banks, described in Figure 37 with an insertion sequence example. However, insertion levels for each individual bank are provided for most of the data presented in this benchmark, so the algorithm in Figure 37 may not be needed.

Source Reference	Elevation (cm)	Description
	460.000	Highest Extent
45 — Stainless Steel Pin	415.558	Top of Control Rod Plenum
45 — Control Rod Upper Plenum	403.778	Bottom of Control Rod Plenum
45 — Control Rod Spacer Pincell	402.508	Bottom of Spacer
45 — Control Rod Upper Absorber Pincell	143.428	Bottom of Upper Absorber (B4C)
45 — Control Rod Lower Absorber Pincell	41.8280	Bottom of Lower Absorber (AIC)
45 — Stainless Steel Pin	39.9580	Bottom of Control Rod
Water	35.0000	Bottom of Fuel Rod
66 — Support Plate / Nozzle Borated Water	20.0000	Bottom of Support Plate
Water	0.00000	Lowest Extent

Figure 36: Control rod pincell axial specification when fully-inserted. This only shows axial sections for the control rod itself, which is inside one of the guide tubes.

Control Rod Insertion Sequence

Starting from all rods fully withdrawn:

- First D moves in alone, until it gets to 113 steps withdrawn

- Now D and C move together until C gets to 113 steps withdrawn
  (D is all the way in when C is at 115)

- Now C and B move together until B gets to 113 steps withdrawn
  (C is all the way in when B is at 115)

- Now B and A move together until A gets to 0 steps withdrawn
  (B is all the way in when A is at 115)

Assuming only movement of each control rod bank by one step at a time, in total this sequence yields 574 unique positions, which we denote with integer $\mathbb{S}$ steps withdrawn. If $\mathbb{S} = 0$ all control rods are out of the core, and if $\mathbb{S} = 574$ all rods are fully inserted. For example for normal operation with the D bank at the bite position of $\mathbb{S}_D = 213$ steps withdrawn, $\mathbb{S} = 228 - 213 = 15$. With this notation, the following algorithm provides the elevation of the axial planes of the active region in each control rod bank (s_i^{bot} and s_i^{top}) for a given $\mathbb{S}$ with the fully inserted elevation s_0 and step width δ.

$$\mathbb{S}_D = \max(0, \ 228 - \mathbb{S})$$
$$\mathbb{S}_C = (\mathbb{S}_D < 113) \ ? \ \max(0, \ 228 - \mathbb{S} + 113 + 3) \ : \ 228$$
$$\mathbb{S}_B = (\mathbb{S}_C < 113) \ ? \ \max(0, \ 228 - \mathbb{S} + 113 \times 2 + 5) \ : \ 228$$
$$\mathbb{S}_A = (\mathbb{S}_B < 113) \ ? \ \max(0, \ 228 - \mathbb{S} + 113 \times 3 + 7) \ : \ 228$$

$$s_A^{\text{bot}} = s_0 + \delta \times \mathbb{S}_A$$
$$s_B^{\text{bot}} = s_0 + \delta \times \mathbb{S}_B$$
$$s_C^{\text{bot}} = s_0 + \delta \times \mathbb{S}_C$$
$$s_D^{\text{bot}} = s_0 + \delta \times \mathbb{S}_D$$

$$s_A^{\text{top}} = s_A^{\text{bot}} + \delta \times 228$$
$$s_B^{\text{top}} = s_B^{\text{bot}} + \delta \times 228$$
$$s_C^{\text{top}} = s_C^{\text{bot}} + \delta \times 228$$
$$s_D^{\text{top}} = s_D^{\text{bot}} + \delta \times 228$$

Figure 37: Control rod insertion sequence and axial specification [14].

2.3.6   Aggregate

By defining the full extent of the axial geometry in the pincells, several features remain to be described or examined in the final combination of each element of the model. In aggregate it is useful to see an exhaustive list of all axial planes used in the model, as presented in Figure 38. Control rod insertions are treated separately, as discussed in Section 2.3.5.

| Elevation (cm)	Description
460.000	Highest Extent
431.876	Top of Upper Nozzle
423.049	Bottom of Upper Nozzle
421.532	Top of BPRA Rod Plenum
419.704	Top of Fuel Rod
417.164	Top of Fuel Rod Plenum
415.558	Top of Control Rod Plenum
415.164	Grid 8 Top
411.806	Grid 8 Bottom
403.778	Bottom of Control Rod Plenum
402.508	Top of Active Fuel
401.238	Top of Active Absorber
400.638	Control Rod Step 228
364.725	Grid 7 Top
359.010	Grid 7 Bottom
312.528	Grid 6 Top
306.813	Grid 6 Bottom
260.331	Grid 5 Top
254.616	Grid 5 Bottom
208.134	Grid 4 Top
202.419	Grid 4 Bottom
155.937	Grid 3 Top
150.222	Grid 3 Bottom
103.740	Grid 2 Top
98.0250	Grid 2 Bottom
41.8280	Bottom of Lower Absorber (AIC)
40.5580	Bottom of Active Absorber
40.5200	Grid 1 Top
39.9580	Control Rod Step 0
38.6600	Bot. of BPRA Rod
37.1621	Grid 1 Bottom
36.7480	Bottom of Active Fuel
35.0000	Bottom of Fuel Rod
20.0000	Bottom of Support Plate
0.00000	Lowest Extent

Figure 38: *Left*: Scale view of row 8 axial cross section, with highlighted grid spacers and partial insertion of control rod bank D to the bite position. *Right*: exhaustive list of all axial planes used in the model, excluding partial control rod insertion planes.

2.3.6.1   Grid Spacers

Nearly all axial features of the model are captured in the axial pincell specifications. However, the stainless steel grid sleeve described in Section 2.2.2.2 for each of the 8 grid spacers needs to be defined on the assembly level, as it is not contained within any of the pincell elements. The axial planes used for the grid sleeves are the same as those used for the grids in the pincells, as listed in Figure 38.

2.3.6.2 Nozzles and Support Plate

By defining pincells as solid material pins below and above the fuel rod regions, the model implicitly approximates the nozzle and support plate regions as depicted in Figure 39. While the axial planes used here were taken from Source 46, this does not necessarily represent the true geometry of this portion of the reactor. However, the special densities of water and steel for the nozzle sections were calculated such that the mass and volume fractions of the materials are consistent with [15]. The material compositions of borated water and steel in the nozzle and support plate are in Material 18 and Material 19 respectively. Thus, when modeling, the material "Nozzle / Support Plate Stainless Steel" (19) rather than "Stainless Steel" should be used for all the fuel rods in the upper and lower nozzle / support plate regions as depicted in Figure 32, while the material "Nozzle / Support Plate Borated Water" (19) rather than "Borated Water" should be used for the water in the nozzles and support plate (Figure 33). Figures 32 through 40 illustrate the modeling details with material names and colors that preserve the actual masses of material. Note that since the bottom nozzle and support plate are both stainless steel, no distinction is made between the two regions.
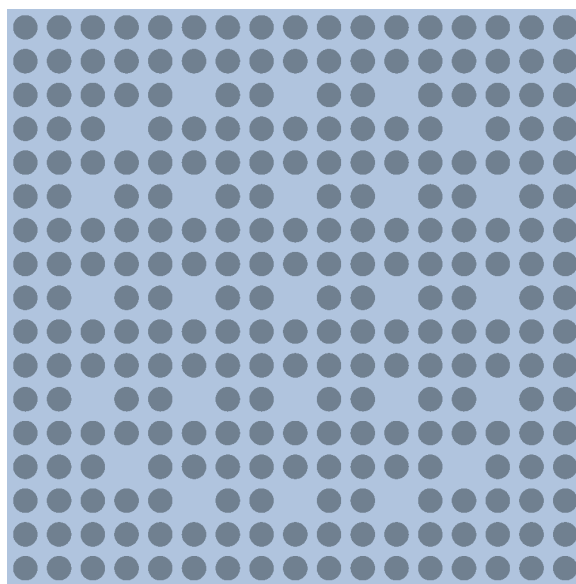

Figure 39: Radial picture of nozzles and support plate in aggregate model

2.3.6.3 Top and Bottom of the Core

For verification, Figure 40 shows scale views close to the bottom and top regions of the core resulting from the aggregate pincell specification as defined previously.
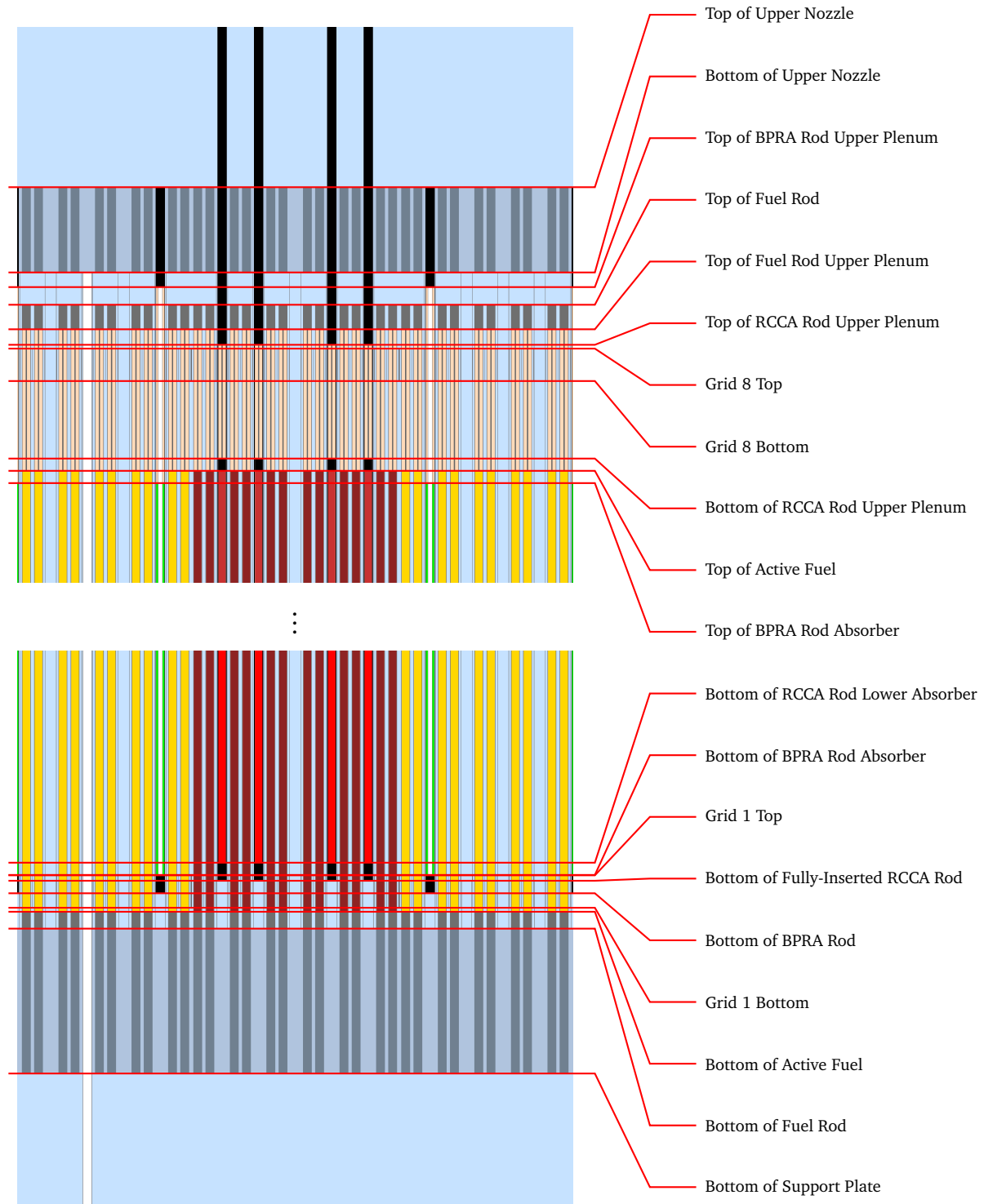
Figure 40: Axial scale view of the model near the top and bottom of the fuel rods in row 8, showing pin plenums, approximated springs, end plugs, and structures. *Blue*: water; *orange*: helium; *black*: stainless steel; *dark gray*: Zircaloy; *dim gray* Inconel; *white*: air; *slate gray*: nozzle / support plate stainless steel; *steel blue*: nozzle / support plate borated water; *green*: borosilicate glass; *yellow*: fuel.

2.4   Materials

Table 4 — Fuel 1.6% Enriched	
Density (g/cc)	10.31341
Isotope	Atom Density (atom/b-cm)
O16	4.5897e-02
O17	1.7436e-05
O18	9.2032e-05
U234	3.0131e-06
U235	3.7503e-04
U238	2.2625e-02

Source: 49

Table 5 — Fuel 2.4% Enriched

Density (g/cc)	10.29748
Isotope	Atom Density (atom/b-cm)
O16	4.5830e-02
O17	1.7411e-05
O18	9.1898e-05
U234	4.4842e-06
U235	5.5814e-04
U238	2.2407e-02

Source: 50

Table 6 — Fuel 3.1% Enriched

Density (g/cc)	10.30166
Isotope	Atom Density (atom/b-cm)
O16	4.5853e-02
O17	1.7420e-05
O18	9.1942e-05
U234	5.7987e-06
U235	7.2175e-04
U238	2.2253e-02

Source: 51

Table 7 — Fuel 3.2% Enriched

Density (g/cc)	10.34115
Isotope	Atom Density (atom/b-cm)
O16	4.6029e-02
O17	1.7487e-05
O18	9.2296e-05
U234	5.9959e-06
U235	7.4630e-04
U238	2.2317e-02

Source: 52

Table 8 — Fuel 3.4% Enriched

Density (g/cc)	10.35917
Isotope	Atom Density (atom/b-cm)
O16	4.6110e-02
O17	1.7517e-05
O18	9.2459e-05
U234	6.4018e-06
U235	7.9681e-04
U238	2.2307e-02

Source: 53

Table 9 — Air

Density (g/cc)	0.00616
Isotope	Atom Density (atom/b-cm)
Ar36	7.8730e-09
Ar38	1.4844e-09
Ar40	2.3506e-06
C12	6.7539e-08
C13	7.5658e-10
N14	1.9680e-04
N15	7.2354e-07
O16	5.2866e-05
O17	2.0084e-08
O18	1.0601e-07

Source: 54

Table 10 — Borosilicate Glass

Density (g/cc)	2.26
Isotope	Atom Density (atom/b-cm)
Al27	1.7352e-03
B10	9.6506e-04
B11	3.9189e-03
O16	4.6514e-02
O17	1.7671e-05
O18	9.3268e-05
Si28	1.6926e-02
Si29	8.5944e-04
Si30	5.6654e-04

Source: 55

Table 11 — Ag-In-Cd Control Rods

Density (g/cc)	10.16
Isotope	Atom Density (atom/b-cm)
Ag107	2.3523e-02
Ag109	2.1854e-02
Cd106	3.3882e-05
Cd108	2.4166e-05
Cd110	3.3936e-04
Cd111	3.4821e-04
Cd112	6.5611e-04
Cd113	3.3275e-04
Cd114	7.8252e-04
Cd116	2.0443e-04
In113	3.4219e-04
In115	7.6511e-03

Source: 56

Table 12 — B4C Control Rods

Density (g/cc)	1.76
Isotope	Atom Density (atom/b-cm)
B10	1.5206e-02
B11	6.1514e-02
C12	1.8972e-02
C13	2.1252e-04

Source: 57

Table 13 — Helium

Density (g/cc)	0.0015981
Isotope	Atom Density (atom/b-cm)
He3	4.8089e-10
He4	2.4044e-04

Source: 58

Table 14 — Inconel 718

Density (g/cc)	8.2
Isotope	Atom Density (atom/b-cm)
Cr50	7.8239e-04
Cr52	1.5088e-02
Cr53	1.7108e-03
Cr54	4.2586e-04
Fe54	1.4797e-03
Fe56	2.3229e-02
Fe57	5.3645e-04
Fe58	7.1392e-05
Mn55	7.8201e-04
Ni58	2.9320e-02
Ni60	1.1294e-02
Ni61	4.9094e-04
Ni62	1.5653e-03
Ni64	3.9864e-04
Si28	5.6757e-04
Si29	2.8820e-05
Si30	1.8998e-05

Source: 59

Table 15 — Stainless Steel 304

Density (g/cc)	8.03
Isotope	Atom Density (atom/b-cm)
Cr50	7.6778e-04
Cr52	1.4806e-02
Cr53	1.6789e-03
Cr54	4.1791e-04
Fe54	3.4620e-03
Fe56	5.4345e-02
Fe57	1.2551e-03
Fe58	1.6703e-04
Mn55	1.7604e-03
Ni58	5.6089e-03
Ni60	2.1605e-03
Ni61	9.3917e-05
Ni62	2.9945e-04
Ni64	7.6261e-05
Si28	9.5281e-04
Si29	4.8381e-05
Si30	3.1893e-05

Source: 60

Table 16 — Zircaloy 4

Density (g/cc)	6.55
Isotope	Atom Density (atom/b-cm)
Cr50	3.2962e-06
Cr52	6.3564e-05
Cr53	7.2076e-06
Cr54	1.7941e-06
Fe54	8.6698e-06
Fe56	1.3610e-04
Fe57	3.1431e-06
Fe58	4.1829e-07
O16	3.0744e-04
O17	1.1680e-07
O18	6.1648e-07
Sn112	4.6735e-06
Sn114	3.1799e-06
Sn115	1.6381e-06
Sn116	7.0055e-05
Sn117	3.7003e-05
Sn118	1.1669e-04
Sn119	4.1387e-05
Sn120	1.5697e-04
Sn122	2.2308e-05
Sn124	2.7897e-05
Zr90	2.1828e-02
Zr91	4.7601e-03
Zr92	7.2759e-03
Zr94	7.3734e-03
Zr96	1.1879e-03

Source: 61

Table 17 — Borated Water

Density (g/cc)	0.740582068
Isotope	Atom Density (atom/b-cm)
B10	7.9714e-06
B11	3.2247e-05
H1	4.9456e-02
H2	7.7035e-06
O16	2.4673e-02
O17	9.3734e-06
O18	4.9474e-05

Source: 62

Table 18 — Nozzle / Support Plate Borated Water

Density (g/cc)	0.981002532
Isotope	Atom Density (atom/b-cm)
B10	1.0559e-05
B11	4.2716e-05
H1	6.5512e-02
H2	1.0204e-05
O16	3.2683e-02
O17	1.2416e-05
O18	6.5535e-05

Source: 63

Table 19 — Nozzle / Support Plate Stainless Steel

Density (g/cc)	3.68384807
Isotope	Atom Density (atom/b-cm)
Cr50	3.5223e-04
Cr52	6.7924e-03
Cr53	7.7020e-04
Cr54	1.9172e-04
Fe54	1.5882e-03
Fe56	2.4931e-02
Fe57	5.7578e-04
Fe58	7.6625e-05
Mn55	8.0762e-04
Ni58	2.5731e-03
Ni60	9.9117e-04
Ni61	4.3085e-05
Ni62	1.3738e-04
Ni64	3.4985e-05
Si28	4.3711e-04
Si29	2.2195e-05
Si30	1.4631e-05

Source: 64

Table 20 — Carbon Steel

Density (g/cc)	7.8		
Isotope	Atom Density (atom/b-cm)	Isotope	Atom Density (atom/b-cm)
Al27	4.3523e-05	B10	2.5833e-06
B11	1.0450e-05	C12	1.0442e-03
C13	1.1697e-05	Ca40	1.7043e-05
Ca42	1.1375e-07	Ca43	2.3734e-08
Ca44	3.6673e-07	Ca46	7.0322e-10
Ca48	3.2875e-08	Cr50	1.3738e-05
Cr52	2.6493e-04	Cr53	3.0041e-05
Cr54	7.4778e-06	Cu63	1.0223e-04
Cu65	4.5608e-05	Fe54	4.7437e-03
Fe56	7.4465e-02	Fe57	1.7197e-03
Fe58	2.2886e-04	Mn55	6.4126e-04
Mo100	2.9814e-05	Mo92	4.4822e-05
Mo94	2.8110e-05	Mo95	4.8567e-05
Mo96	5.1015e-05	Mo97	2.9319e-05
Mo98	7.4327e-05	Nb93	5.0559e-06
Ni58	4.0862e-04	Ni60	1.5740e-04
Ni61	6.8420e-06	Ni62	2.1815e-05
Ni64	5.5557e-06	P31	3.7913e-05
S32	3.4808e-05	S33	2.7420e-07
S34	1.5368e-06	S36	5.3398e-09
Si28	6.1702e-04	Si29	3.1330e-05
Si30	2.0653e-05	Ti46	1.2144e-06
Ti47	1.0952e-06	Ti48	1.0851e-05
Ti49	7.9634e-07	Ti50	7.6249e-07
V50	1.1526e-07	V51	4.5989e-05

Source: 65

3   Operating Data

3.1   Processing Measured In-Core Detector Data

In this reactor plant, there are 58 assemblies that contain in-core detectors. This layout of in-core detectors is shown in Figure 31. These detectors are typically U-235 fission chambers varying in mass of U-235. Although there are 58 locations, there are usually only a few detectors (6-10). When measurements are being taken, multiple *passes* are performed to adequately measure all 58 assemblies. Each detector will, however, pass through one common assembly. This becomes important in the normalization process of detector signals.

Before a measurement is taken, detectors are inserted into the core through instrumentation tubes in assemblies until the top of the assembly is hit. Detector measurements are then taken as the detectors are pulled back through the core at a constant speed. Thus, each measurement reported is an integral of the signal over the recording time. Also, axial locations of where data is recorded may be slightly skewed. In these measurements, 61 axial data points were collected and processed with a Python script.

3.1.1   Example – Hot Zero Power Measurements

This section will go through the process of filtering measured data for HZP. It should be noted that the algorithm developed to process HZP data was used for all detector data. Therefore, some of the detector maps may show errors in processing. Current work is underway to develop an algorithm that can be applied to all data. Under HZP conditions, the core power for these measurements is approximately 25 MWth. Raw data was processed by first organizing it in Python objects. Each collection of measurements contain detector information for multiple passes through the core in various assemblies. Raw data for HZP is shown in Figure 41. In order to show all detector signals on one plot, each raw data signal was normalized to a sum of unity.

The first step in this process is to remove any detector background signal. This information was supplied with the raw data and can be subtracted from each detector measurement pass. The corrected data for background is shown in Figure 42.

Depending on the strength of the signal being measured, the signal can be amplified by adjusting the gain on the detectors. Gain factors are also reported with the raw data. When processing, these gain factors are multiplied by the measured data. For HZP, all of the gain factors are unity. Figure 43 shows the measured data after gain factors are applied.

In some of the detector signals, zero points exist where the detector failed. These zero points are removed by performing a linear interpolation/extrapolation between/from the nearest two points. The corrected data is shown in Figure 44.

As explained above, there is one common assembly where all detectors will pass. This is needed
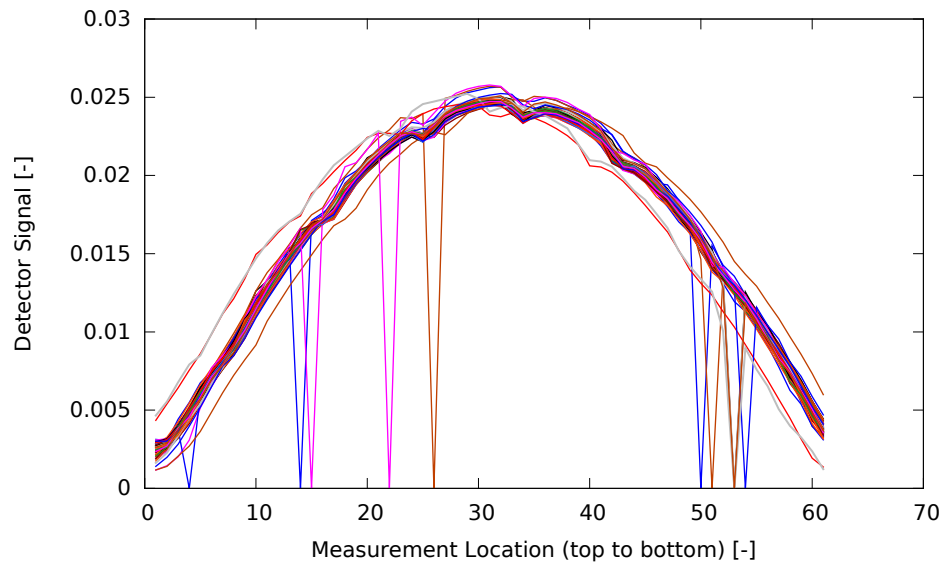
Figure 41: Initial Raw Detector Measurements (top to bottom).
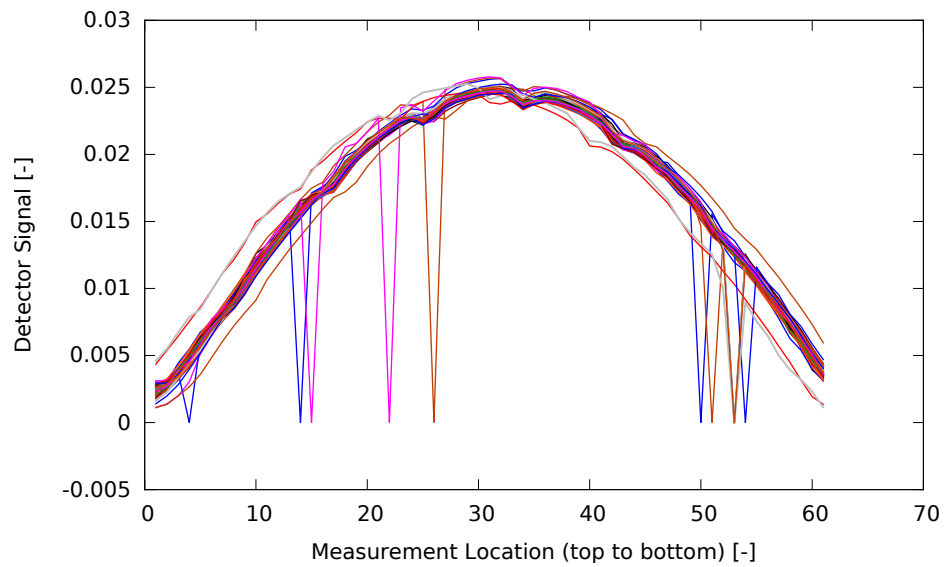
Figure 42: Detector Measurements Corrected for Background (top to bottom).
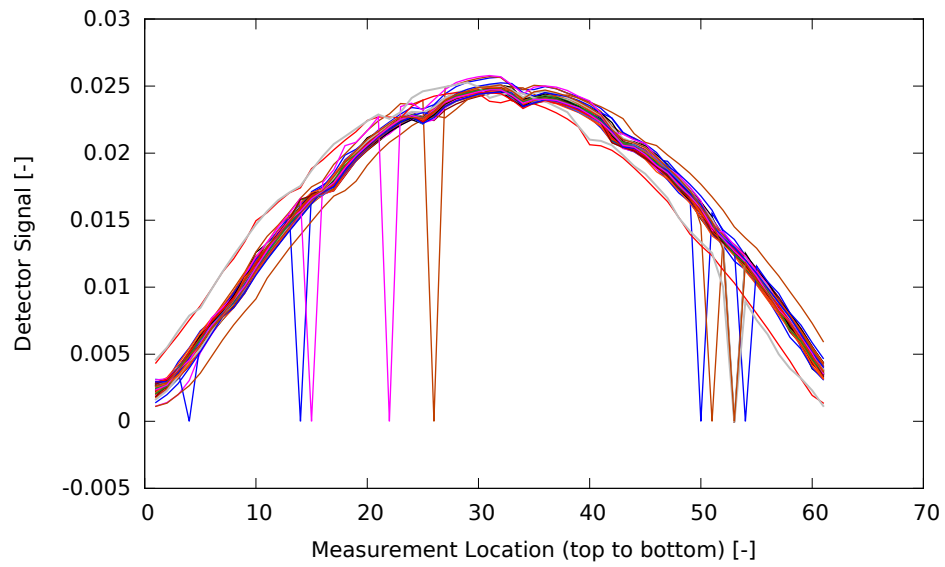
Figure 43: Detector Measurements Gain Factors Applied (top to bottom).
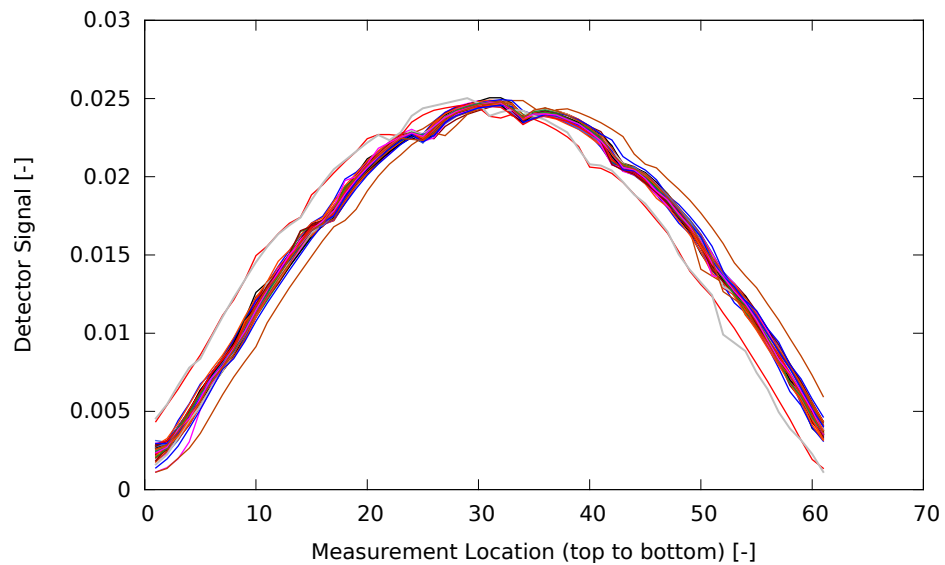
Figure 44: Detector Measurements with Zero Points Removed (top to bottom).
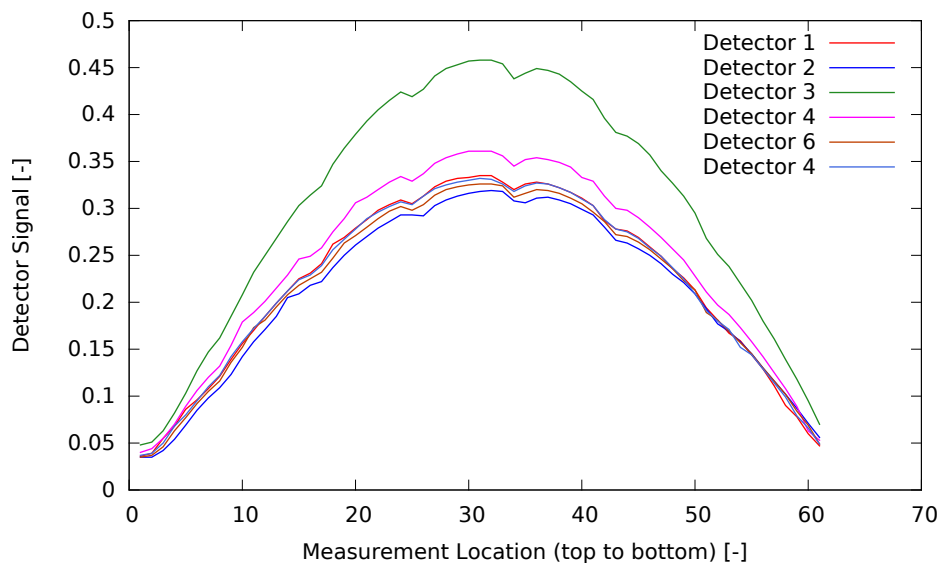
Figure 45: Detector Measurements with in J10 Assembly (top to bottom).

for normalization of detector signals. In this plant, assembly J10 was chosen as the common assembly. Figure 45 shows the measurements taken in assembly J10.

Each detector measurement represents a different measurement pass. The core power during one pass may not be the same as the others. There is typically a small fluctuation present in the core power. To account for this, each signal is divided by the core power reported during that measurement pass. The resulting detector signals are shown in Figure 46 for assembly J10.

The next step in the process is to make sure that all detector signals line up with one another. We can verify this by plotting all 58 detector signals on top of each other. This is the same as plot as Figure 46, except all assemblies are plotted here with signals normalized for shape comparison. This is shown in Figure 47. It is observed that not all of the signals are aligned with each other. Luckily, signals can be aligned to grid depressions. Here, we align to three grid depression positions, 25, 34, and 42, which are located in the centerline of grid 5, grid 4 and grid 3 respectively. The first step in this process is to find the measurement indexes corresponding to the local minimum in three regions, 22 to 28, 31 to 37, and 39 to 45 respectively. Then for each assembly, if the measurement indexes are inconsistent with correct indexes, a shifting length is estimated to make all the measurement indexes best match the correct indexes. All grids are then shifted either left or right. Depending on the shift direction, one end will lose a point and the other will gain one. The data point that is lost is just deleted from the data array, while the point that is gained is determined by a simple linear extrapolation from the nearest two points. The resulting realignment is shown in Figure 48. Results show that all detector signals are more consistently aligned, however still not perfect. The span of these signals can also be attributed to measurement uncertainty as they should all have the same shape once normalized here. There is one signal that is an outlier is observed between measurements 0 and 5. This assembly location corresponds to where control rod bank D is slightly inserted. Therefore, we should expect this depression in the signal toward the top of the core.
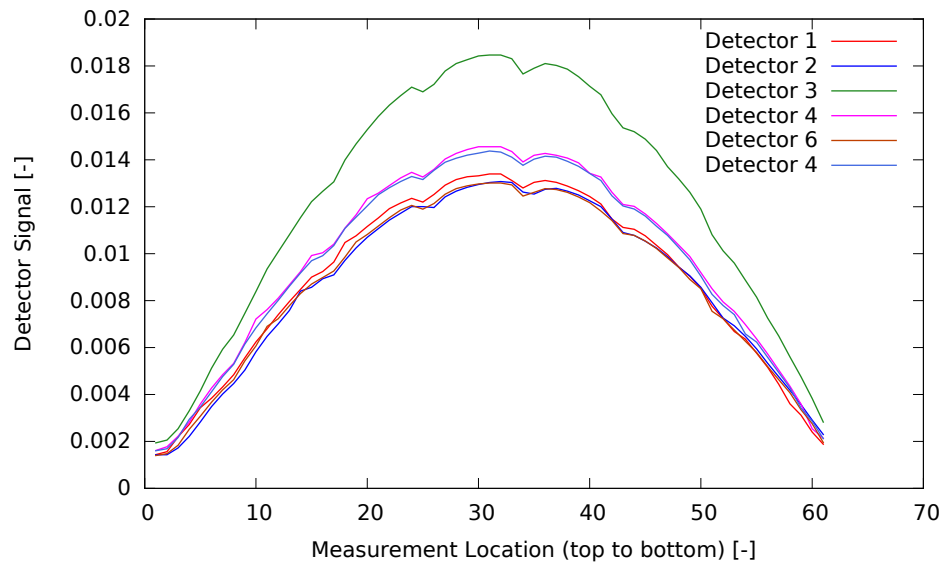
Figure 46: J10 Detector Measurements Divided by Core Power (top to bottom).
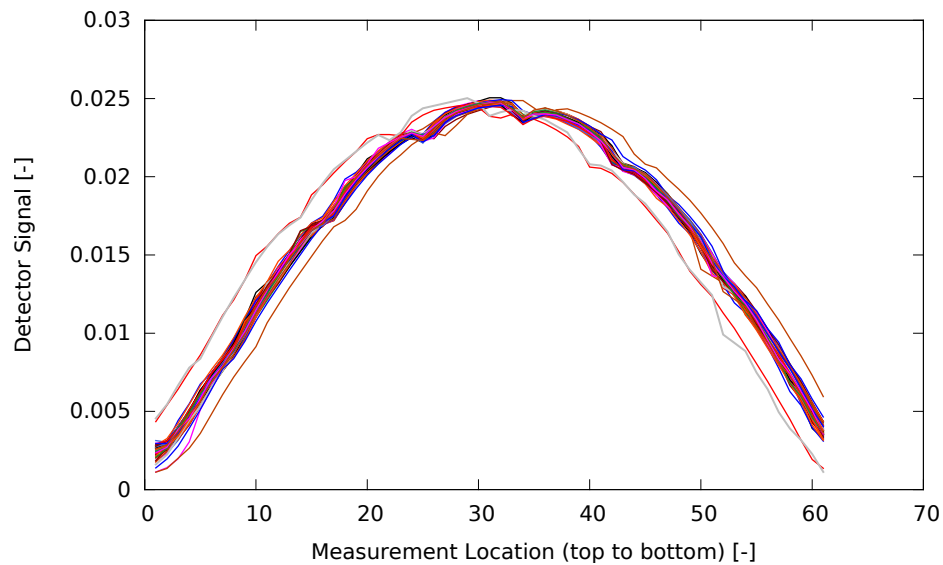
Figure 47: All Detector Signals Before Realignment.
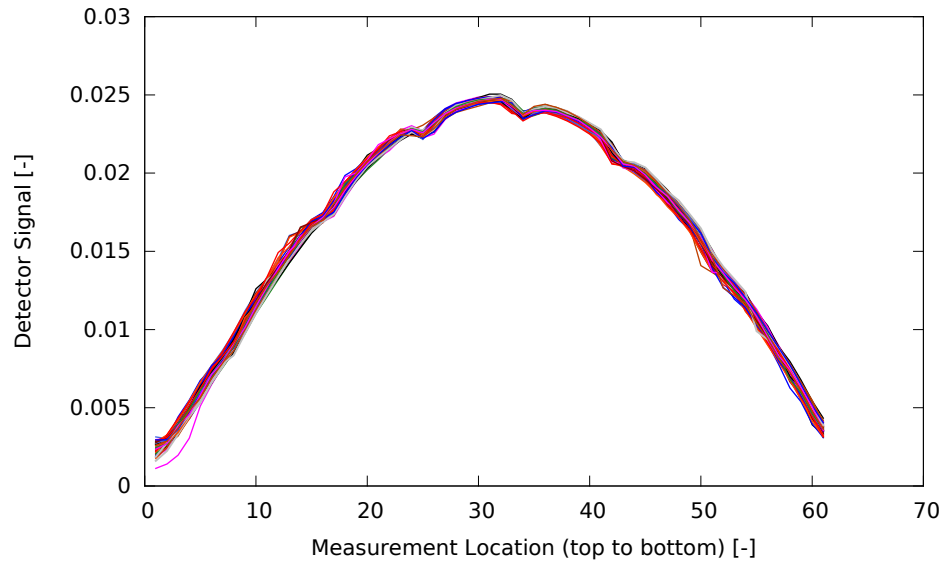
Figure 48: All Detector Signals After Realignment.

The next step in the process is to average detector signals that were measured from the same detector. It is important to look at the raw signals before performing this step since measurements may be poor. If this is observed, the poor measurement is commented out in the data file. In Figure 46 the two signals from detector 4 are close to each other and should be averaged. The resulting signals for assembly J10 are shown in Figure 49.

Each fission chamber detector contains a different amount of U-235. Therefore, some normalization process is needed to account for this mass difference. To get these normalization factors, the average of all detector signals is determined first. Then, normalization factors are computed by taking the ratio of the integral of each individual detector signal to the integral of the mean of all detector signals. For example, for HZP the normalization factors for each detector are:

- Detector 1: 0.922

- Detector 2: 0.901

- Detector 3: 1.272

- Detector 4: 1.002

- Detector 6: 0.903

These normalization factors are then multiplied to each corresponding detector signal in the core. The resulting signals are now very close to each other as shown in Figure 50 for assembly J10.

Lastly, detector signals need to be put on an axial coordinate grid corresponding to points that range from the bottom to top of active fuel. To do this we use the same grid point as before

59
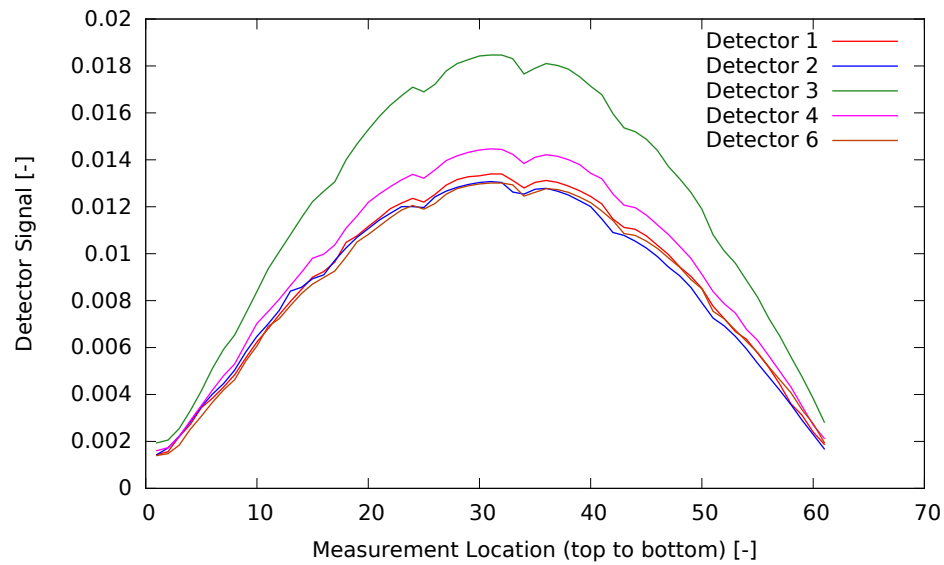
Figure 49: Multiple Detector Signals Averaged in J10 (top to bottom).
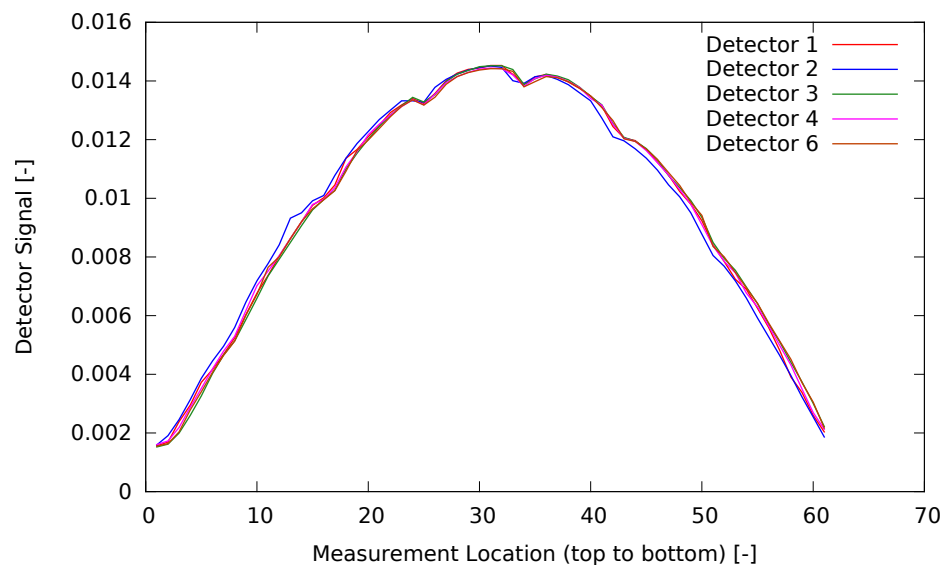
Figure 50: Application of Detector Normalization Factors for J10.

since we know that the centerline location of this grid is at 221.9 cm above bottom of active
fuel. The distance between axial measurement locations is assumed uniform and is equal to
active core height divided by 60 intervals. A 2nd order spline fit is then used to map from
measured data axial locations to a axial map has equal data points exactly at the Top of Active
Fuel (TAF) and Bottom of Active Fuel (BAF). A comparison of applying this spline is shown in
Figure 51. The spline fit does well for this data, however grid depressions are now less since the
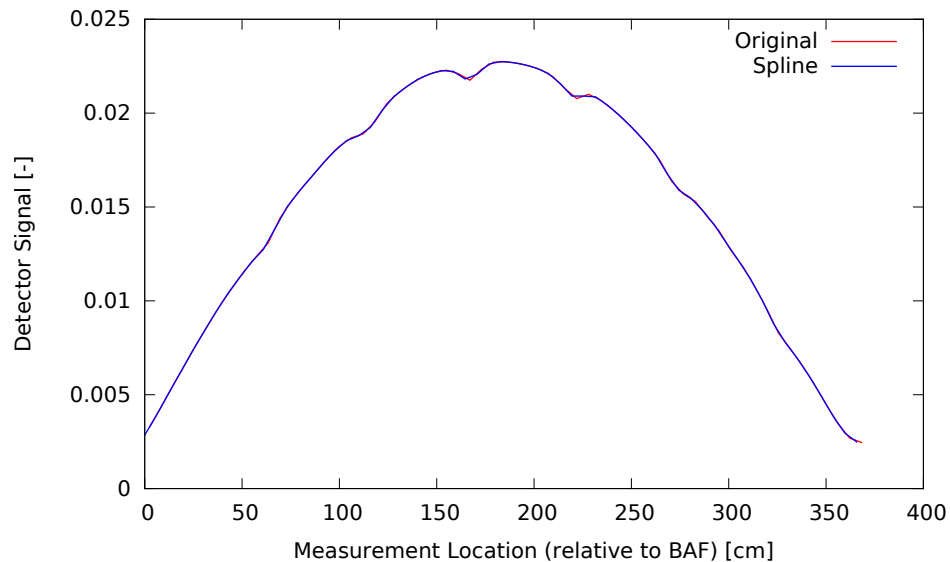
Figure 51: Comparison of Splined Data for Assembly J10.

grid centerline does not match up with the final axial grid. Before the spline, all detector signals
were averaged such that there is only one signal per assembly. All splined signals are shown
in Figure 52. There is some spread in the data when they are all normalized to one another.
There is one detector signal that seems to not follow the same shape at the top of the core. That
measurement corresponds to assembly D12 where control rod bank D is slightly inserted and
thus there is a depression in the measurement signal. A separate Excel sheet contains all of
the processed data organized by measurement data file and by assembly. A plot of the final
measurements (not all normalized to sum of unity) is shown in Figure 53.
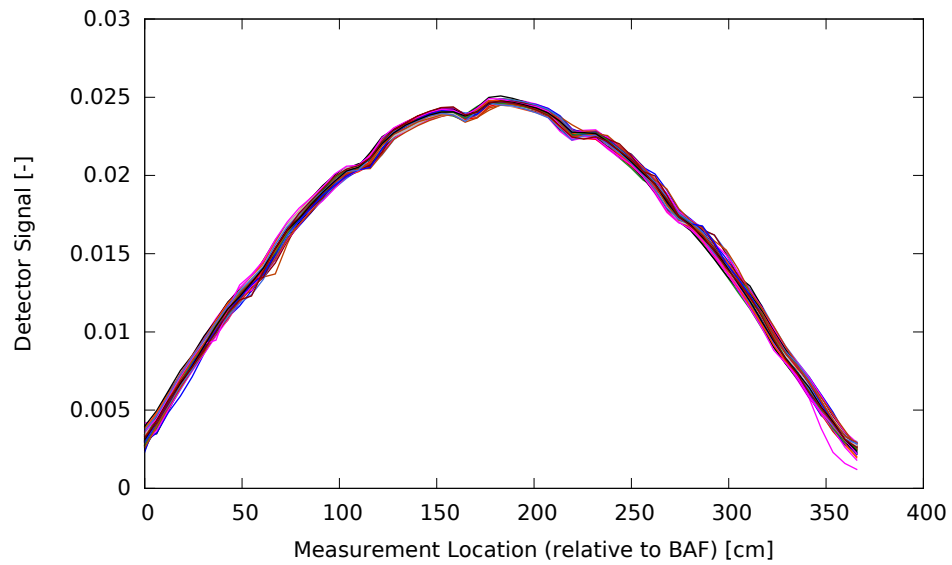
Figure 52: Comparison of All Assemblies after Spline.
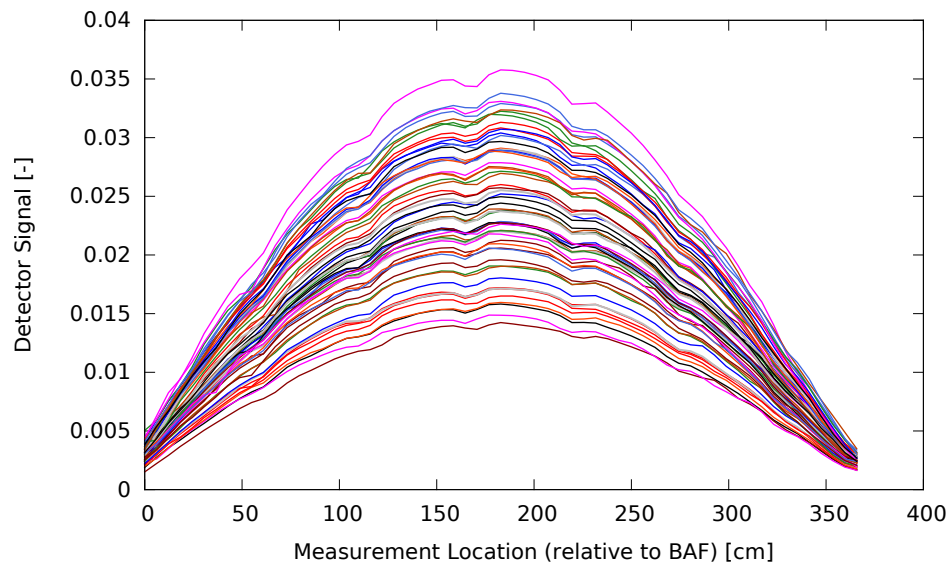
Figure 53: Final Processed HZP Measurement Data.

3.2 Hot Zero Power Data Discussion

Table 21 lists the thermal power of the reactor during initial physics testing the first available detector maps. Also included are the rod bank positions and critical boron concentration. This data can be used to evaluate how far off reactor models are from critical at HZP conditions.

Table 21: Cycle 1 hot zero power physics configuration.

Core Power	25 MWth
Core Flow Rate	61.5×10^6 kg/hr
Inlet Coolant Temperature	$560°$ F
Rod Bank A Position	Step 228
Rod Bank B Position	Step 228
Rod Bank C Position	Step 228
Rod Bank D Position	Step 213
Boron Concentration	975 ppm

Radial maps were also created to view the average relative power produced per assembly. These were obtained by renormalizing the signals in Figure 53 such that their total sum is the number of detector locations (in this case 58). Each measurement in an assembly was then axially averaged to produce a relative radial peaking factor. In Figure 54, this factor is presented on each assembly where a measurement was taken.

Results show that measurement locations are consistent with the reported instrumentation diagram shown in Figure 31. Since the reactor is quarter-core symmetric (disregarding perturbations from instrument tubes), measurements can be compared. For example, assemblies H13, C8, H3 and N8 are located in symmetric positions. The measured values in these locations should be close. It is observed that the measurements are on the same order, but not all that close. This can happen at low powers and gives us an indication of measurement uncertainty.

Another way to look at the data is to collapse it to quarter core. We can compare rotational quarter core positions. If more than one radial power is available, the mean and standard deviation are reported. Otherwise, the result from Figure 54 is listed without a standard deviation. This is shown in Figure 55. In each assembly, three values are reported. From top to bottom they are: average of radial (axially averaged) signals, standard deviation of average and number of measurements that were averaged. The standard deviations give us some idea on the uncertainty in these measured values. They can range all the way up to 5.4%. A weighted average of the standard deviation was computed to get an idea of the overall measurement uncertainty. This was determined by multiplying each uncertainty by the number of radial powers and then dividing by 58. For HZP, this uncertainty is 3.7%. This is rather high since we really would like to see values below 1%. However, when the power is very low, power tilting can occur which contributes to this high uncertainty.

To compare simulation values to these measured data, axial edits of a tally such as U235 fission
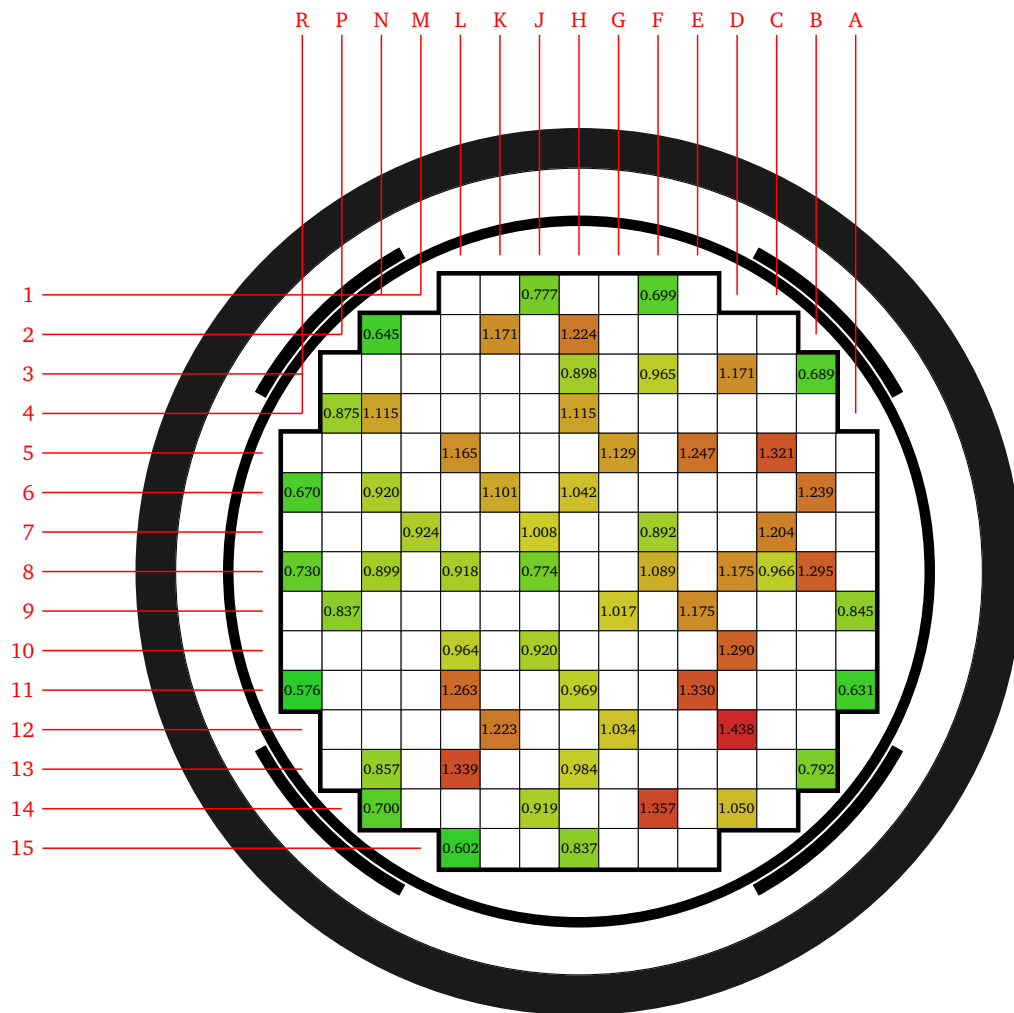
Figure 54: Radial detector measurements (axially integrated).
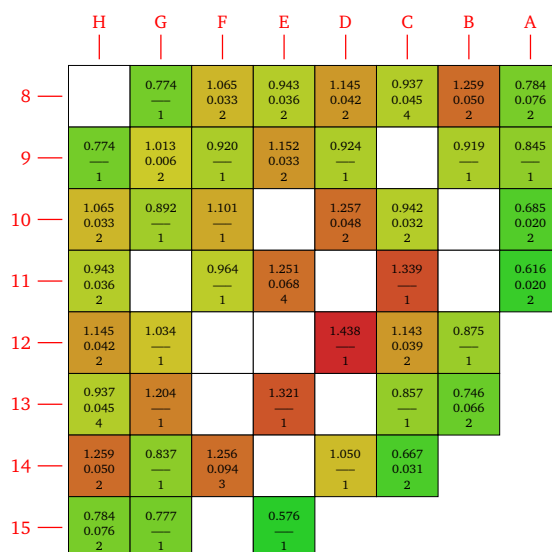
Figure 55: Quarter core (full core folded) radial measurements.

rate must be applied to each instrumented assembly in the core. To be fully consistent with the data a constant width 60 interval mesh (61 points) from bottom of active fuel to top of active fuel should be applied. All signals should be renormalized such that their average is 1.0 (or sum of all signals is 58).

Table 22 presents measured data for control rod bank worths and isothermal temperature coefficients for HZP conditions. Also provided are the critical boron concentrations for each configuration. Likewise, Table 23 presents the same data that is available for cycle 2. In contrast to cycle 1, control rod bank worths in cycle 2 were reported per individual bank.

Table 22: Cycle 1 hot zero power physics data, including critical boron concentrations, control rod bank worths for the full insertion sequence, and isothermal temperature coefficients.

Crit. Boron Concentrations (ppm)		Control Rod Bank Worths (pcm)		Temp. Coeffs. (pcm/°F)	
All Rods Out (ARO)	975			ARO	-1.75
D in	902	D in	788	D in	-2.75
C, D in	810	C with D in	1203	C, D in	-8.01
		B with D, C in	1171		
A, B, C, D in	686	A with D, C, B in	548		
		SE with D, C, B, A in	461		
		SD with D, C, B, A, SE in	772		
A, B, C, D, SE, SD, SC in	508	SC with D, C, B, A, SE, SD in	1099		

Table 23: Cycle 2 hot zero power physics data, including critical boron concentrations, control rod bank worths for the full insertion sequence, and isothermal temperature coefficients.

Crit. Boron Concentrations (ppm)		Control Rod Bank Worths (pcm)		Temp. Coeffs. (pcm/°F)	
ARO	1405			ARO	1.71
		D	426		
C in	1273	C	1014		
		B	716		
		A	420		
		SE	438		
		SD	305		
		SC	307		
		SB	781		
		SA	326		
		Total	4733		

3.3   Cycle 1 and 2 Available Data

3.3.1   Detector Measurement Maps

For Cycle 1 and 2 operation of this reactor, there are detector measurement maps available at various times during operation. For each measurement file, data is given for core power, inlet coolant temperature, core burnup, critical boron concentration and rod bank configuration. Although these are not described here, each measurement file has been processed according to the methodology described in Section 3.1. These are available online at the MIT-CRPG website.

3.3.2   Tilt Corrected Maps

The BEAVRS measured data presents a very large NW-SE (10%) tilt at HZP conditions that cannot be explained by detector measurements alone, since the core loading pattern is known to be symmetric. Simulations of such maps produce symmetric results, thus indicating a phenomenon that has not been accounted for. The leading hypothesis for this tilt is that it is created by a larger water gap in one corner of the core that stems from the core loading. As bundles are inserted and leaning against the baffle, uneven gaps could occur in opposite corners of the core. These gaps even out as the reactor heats up and fuel swells under irradiations. A script is introduced to fit a planar x-y tilt using the available detector data, and adjust the detector measurements so that the resulting radial map is eighth-core symmetric. Figure 56 illustrates a tilt-corrected radial map at HZP conditions that is eighth-core symmetric. Figures 57 and 58 plot the magnitude of the planar tilt over Cycle 1 and 2 respectively, and indeed as predicted, the tilt corrects itself as burnup increases.

For each burnup, tilt-corrected data at each assembly, as well as tilt-corrected radial maps are
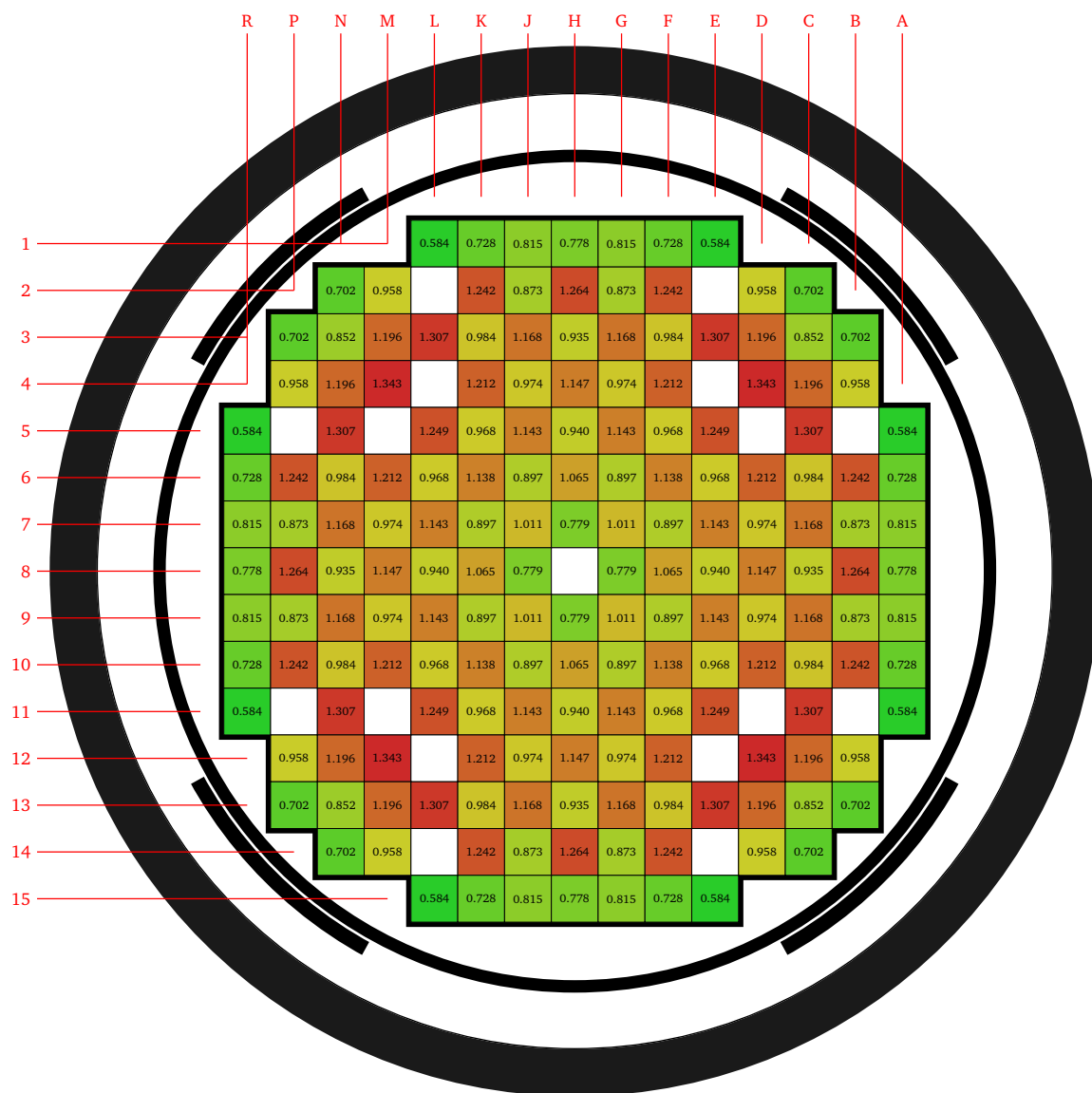
Figure 56: Radial detector measurements (tilt corrected).
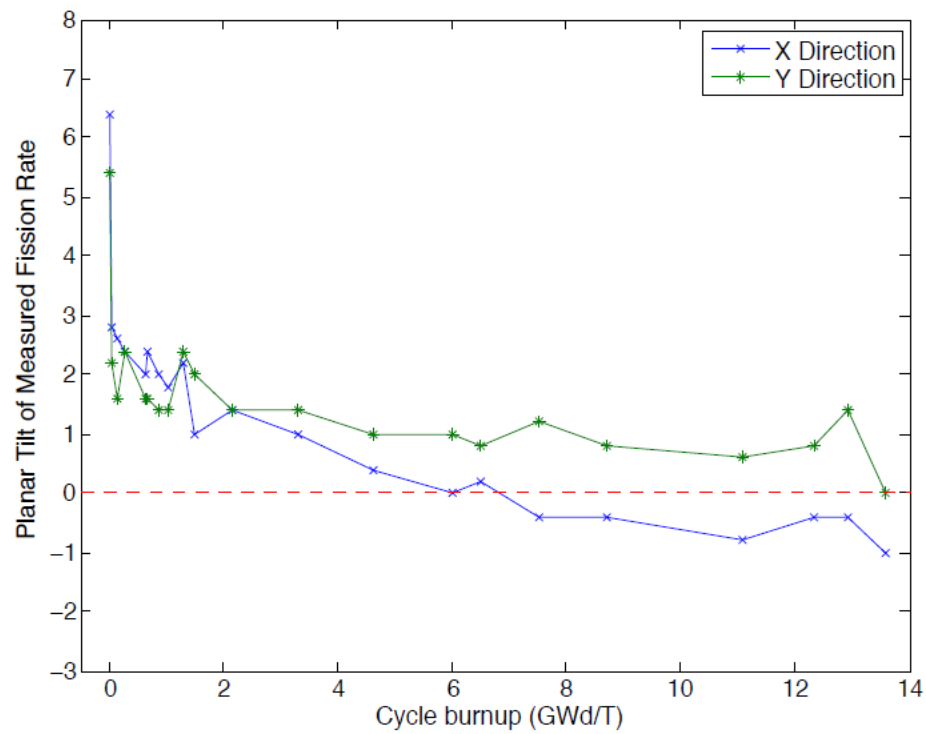
Figure 57: Planar tilt for cycle 1
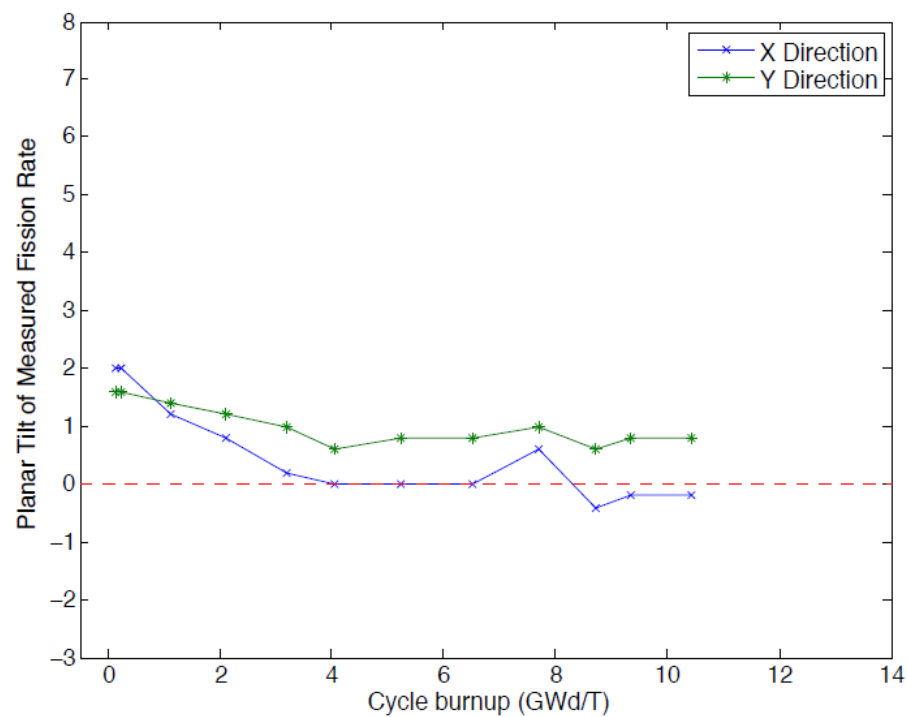
Figure 58: Planar tilt for cycle 2

68

all available on the MIT-CRPG website. It must be noted that there is no definitive explanation for why this tilt in the data arises or the validity of the planar tilt correction, so this data should be utilized at the user's own discretion.

3.3.3   Boron Letdown Curve

Also available is the boron letdown curve during Cycle 1 and Cycle 2 operation. Figure 59 and corresponding Table 24 present the boron letdown data. Finally, the power history reference from Beginning of Cycle (BOC) for Cycle 1 operation is presented in Figure 60. Power history data is also available online at the MIT-CRPG website. In Figure 60, locations of where detector maps are available are also shown. Note, the powers shown in Figure 60 are 24-hr averages, whereas, in detector measurement files, powers reported are instantaneous at the time of measurement. In the plot they are shown to be coincident with the power history, however, in the files they may be slightly different. Similarly, Figure 61 shows the power history of Cycle 2.
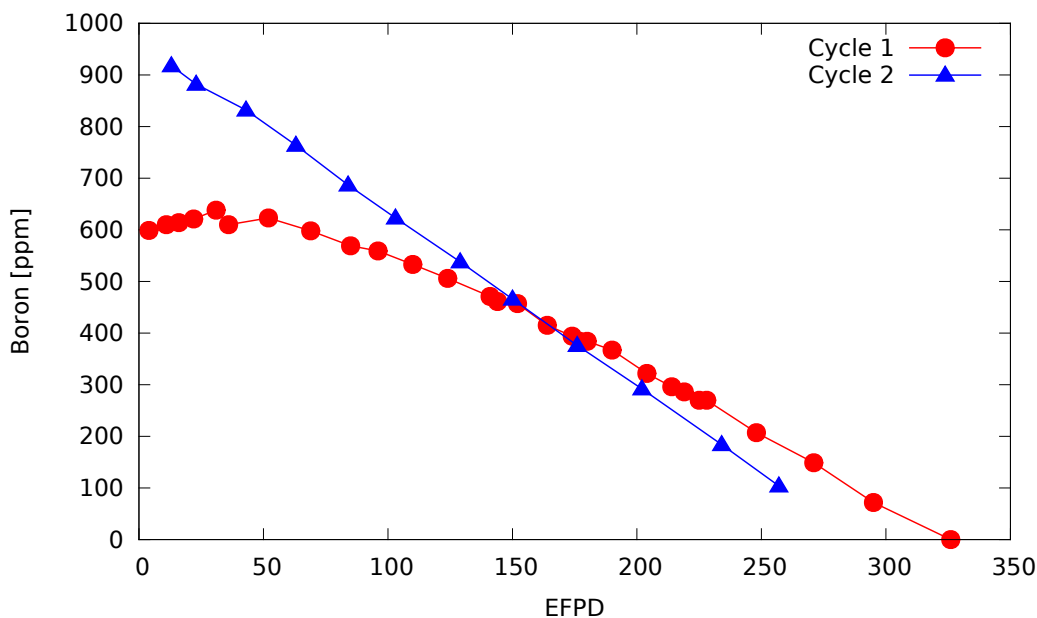
Figure 59: Measured boron letdown curves for two cycles of operation.

Table 24: Boron Letdown Curve Data for Cycles 1 and 2.

Cycle 1		Cycle 2	
EFPD	Boron [ppm]	EFPD	Boron [ppm]
4	599	13	918
11	610	23	882
16	614	43	832
22	621	63	764
31	638	84	687
36	610	103	623
52	623	129	538
69	598	150	466
85	569	176	376
96	559	202	292
110	533	234	184
124	506	257	104
141	471		
144	461		
152	457		
164	415		
174	394		
177	384		
180	384		
190	367		
204	322		
214	296		
219	286		
225	270		
228	270		
248	207		
271	149		
295	72		
326	0		
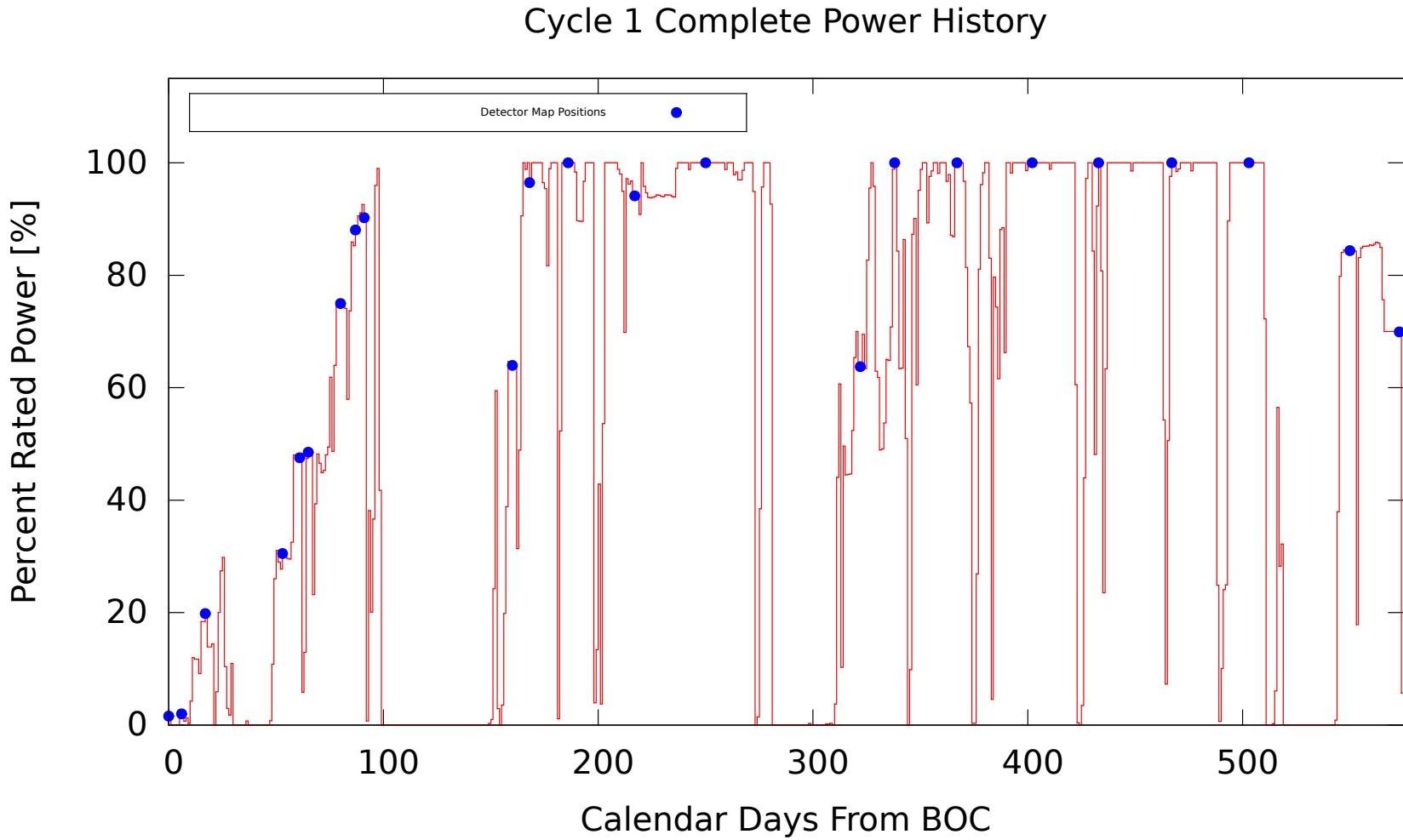
Figure 60: Power history of Cycle 1.
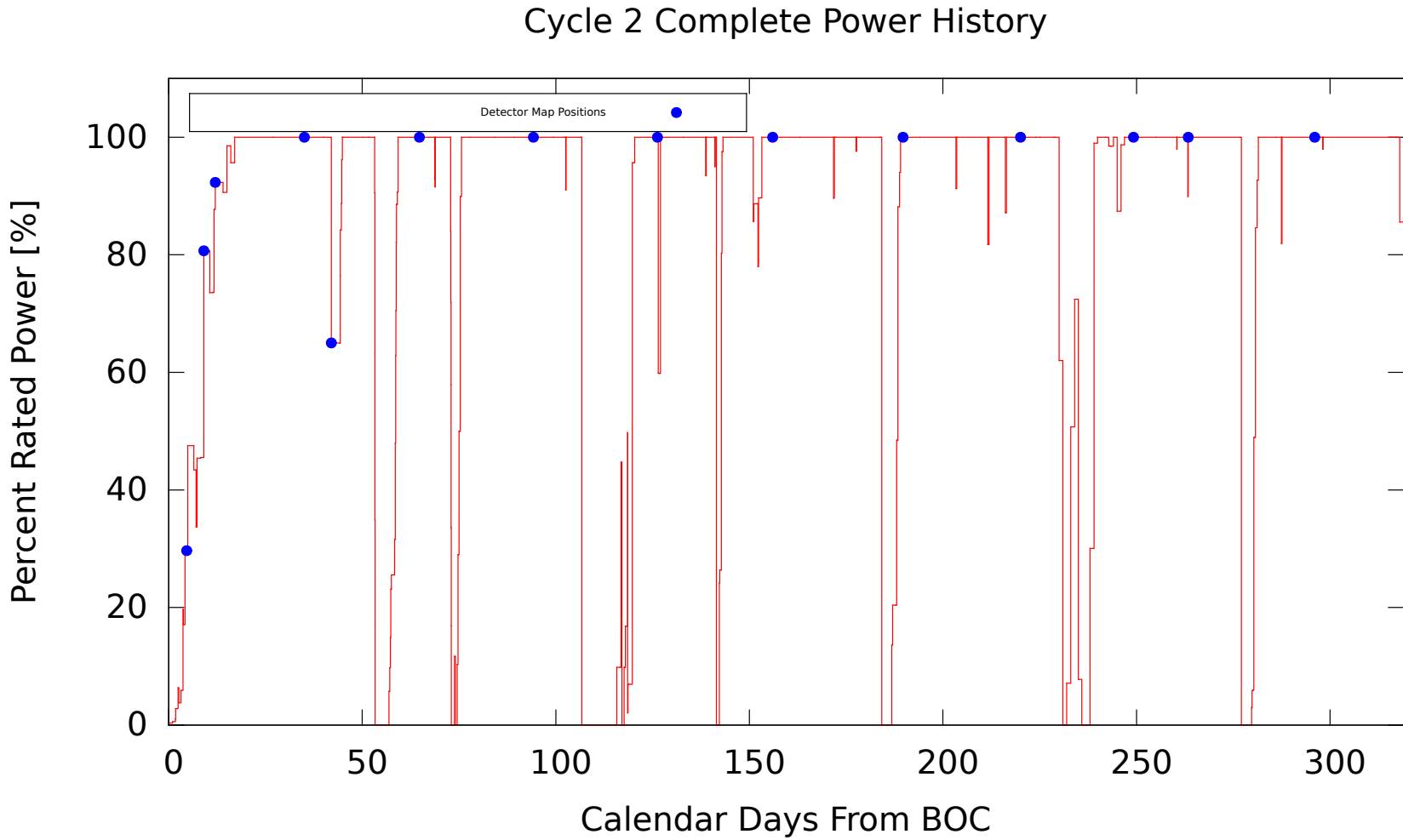
Figure 61: Power history of Cycle 2.

3.4   Uncertainty Quantification of Measurements

In addition to the model parameters and measured data, the associated uncertainties are also essential for the validation of high-fidelity tools. A series of uncertainty quantification work has been carried out in the BEAVRS benchmark. Uncertainties of various measurements are available in the data package, while the evaluation methods are detailed in [16] and [17].

References

[1] N. Horelik, B. Herman, B. Forget, and K. Smith. Benchmark for Evaluation and Validation of Reactor Simulations (BEAVRS), v1.0.1. *Proc. Int. Conf. Mathematics and Computational Methods Applied to Nuc. Sci. & Eng.*, 2013. Sun Valley, Idaho.

[2] K.S. Smith. Assembly homogenization techniques for light water reactor analysis. *Progress in Nuclear Energy*, 17(3):303 – 335, 1986.

[3] J. E. Hoogenboom and W. R. Martin. A Proposal for a Benchmark to Monitor the Performance of Detailed Monte Carlo Calculation of Power Densities in a Full Size Reactor Core. *Proc. Int. Conf. Mathematics, Computational Methods, and Reactor Physics*, 2009. Saratoga Springs, New York.

[4] D. Kelly, T. Sutton, T. Trumbull, and P. Dobreff. MC21 Monte Carlo Analysis of the Hoogenboom-Martin Full-Core PWR Benchmark Problem. *Proc. PHYSOR 2010, Adv. in Reac. Phys. to Power the Nuc. Renaissance, Pittsburgh, Pennsylvania, USA, May 9-14, on CD-ROM(2010)*, May 2010.

[5] D. Kelly, T. Sutton, and S. Wilson. MC21 Analysis of the Nuclear Energy Agency Monte Carlo Performance Benchmark Problem. *Proc. PHYSOR 2012, Adv. in Reac. Phys., Knoxville, Tennessee, USA April 15-20, on CD-ROM(2010)*, April 2012.

[6] K. Smith. Reactor Core Methods, 2003. Invited lecture at the M&C2003 International Conference, April 6-10, 2003, Gatlinburg, TN, USA (http://wwwtest.iri.tudelft.nl/j̃hoogenb).

[7] J. J. Jarrell, A. T. Godfrey, T. M. Evans, and G. G. Davidson. Full Core Reactor Analysis: Running Denovo on Jaguar. *Proc. PHYSOR 2012, Adv. in Reac. Phys., Knoxville, Tennessee, USA April 15-20, on CD-ROM(2010)*, April 2012.

[8] USDOE. Consortium for Advanced Simulation of Light Water Reactors (CASL), 2012. http://www.casl.gov/goals.shtml.

[9] USDOE. About CESAR | Center for Exascale Simulation of Advanced Reactors, 2012. http://cesar.mcs.anl.gov/content/about-cesar.

[10] OECD/NEA. International Reactor Physics Benchmark Experiments (IRPhE), May 2012. ISBN 978-92-64-99168-2.

[11] K.S. Smith, S. Tarves, T. Bahadir, and R. Ferrer. Benchmarks for Quantifying Fuel Reactivity Depletion Uncertainty. Technical Report 1022909, Electric Power Research Institute, 2011.

[12] Benchmark on Deterministic Transport Calculations Without Spatial Homogenisation. Technical Report NEA/NSC/DOC(2005)16, NEA No. 5420, 2005. ISBN 92-64-01069-6.

[13] S. Douglass, F. Rahnema, and J. Margulies. A stylized three dimensional PWR whole-core benchmark problem with Gadolinium. *Annals of Nuclear Energy*, 37(10):1384 – 1403, 2010.

[14] K. Smith. Personal communication on control rod sequence, May 2012.

[15] Civilian Radioactive Waste Management System Management & Operating Contractor. Summary Report of Commercial Reactor Criticality Data for Catawba Unit 1. Technical Report ML033530020, US Department of Energy, 1998.

[16] Jingang Liang, Shikhar Kumar, Benoit Forget, and Kord Smith. Quantifying uncertainty in the beavrs benchmark. In *Proc. Int. Conf. Mathematics and Computational Methods Applied to Nuc. Sci. & Eng*, 2017.

[17] Shikhar Kumar, Jingang Liang, Miriam Rathbun, Benoit Forget, and Kord Smith. Integral full core multi-physics pwr benchmark with measured data neup 14-6742: Final report. Technical report, Massachusetts Institute of Technology, 2018.

[18] PWR Utility. Specifications and Measured Data from PWR Plant. 2012.

[19] Global Data. Power eTrack, Catawba 1 Nuclear Power Plant, 2013. http://www.poweretrack.com.libproxy.mit.edu/.

[20] Engineer at Utility. Additional PWR Plant Specifications, October 2012.

[21] K. J. Geelhood, W. G. Luscher, and C. E. Beyer. FRAPCON-3.4: Integral Assessment. Technical Report NUREG/CR-7022, Vol. 2; PNNL-19418, Vol. 2, Pacific Northwest National Laboratory; USNRC, March 2011. http://frapcon.labworks.org/.

[22] Tennessee Valley Authority. Watts Bar, Unit 2 - Amendment 98 to Final Safety Analysis Report, Section 4, Reactor. Technical Report ML101370397, USNRC, May 2010.

[23] PWR Utility. Data Measurements from PWR Plant for Cycles 1 and 2. 2012.

[24] Engineering Toolbox. Air Properties. Electronic, January 2013. http://www.engineeringtoolbox.com/air-properties-d_156.html.

[25] Studsvik Scandpower. *CASMO-4: A Fuel Assembly Burnup Program*, University edition, 2009.

[26] National Institute of Standards and Technology. Isothermal Properties for Helium. Electronic, January 2013.

[27] AK Steel. *304/304L Stainless Steel Product Data Sheet*, January 2013. UNS S30400.

[28] National Institute of Standards and Technology. Isothermal Properties for Water. Electronic, January 2013.

[29] American Society for Testing and Materials. *Standard Specification for Quenched and Tempered Vacuum-Treated Carbon and Alloy Steel Forgings for Pressure Vessels – A508* , June 2014.

[30] E. M. Baum, M. C. Ernesti, H. D. Knox, T. R. Miller, and A. M. Watson. *Nuclides and Isotopes*. Chart of the Nuclides. Knolls Atomic Power Laboratory, 17 edition, 2009.

[31] Juris Meija, Tyler B Coplen, Michael Berglund, Willi A Brand, Paul De Bièvre, Manfred Gröning, Norman E Holden, Johanna Irrgeher, Robert D Loss, Thomas Walczyk, et al. Isotopic compositions of the elements 2013 (iupac technical report). *Pure and Applied Chemistry*, 88(3):293–306, 2016.

Source Details

Source 1 — Core Arrangement of Fuel Assemblies

This information is reported on the Core Arrangement worksheet.

References

[18]

Pages

3, 27, 29, 31

Source 2 — Cycle 2 Shuffling Pattern

This information is reported on the C2 Core Shuffle worksheet.

References

[18]

Pages

29

Source 3 — Fuel Assembly Loading

This information is reported on the Assembly Loading worksheet.

References

[18]

Pages

3

Source 4 — Fuel Lattice Specifications

This information is reported on the Fuel Lattice worksheet provided by the utility.

References

[18]

Pages

3, 13

Source 5 — Active Core Height

This information is reported on the Fuel Lattice worksheet (Source 4). The active fuel length is

$$L_f = 144\,\text{in} \cdot 2.54\frac{\text{cm}}{\text{in}} = 365.76\,\text{cm}$$

References

[18]

Value

365.76

Units

cm

Pages

3, 34

Source 6 — Nominal Core Power

Nominal Core Power is taken to be that for Catawba, which is available online from Power etrack.

References

[19]

Value

3411

Units

MWth

Pages

3

Source 7 — Core Mass Flow Rate

From an email communication with the utility, the total pump flow rate is 61.5×10^6 kg/hr. Normally, about 5% of the flow goes into the bypass region, so 95% of flow is through the core area, and the flow in the guide tubes is very low. It is assumed that this has no impact on active cooling flow. It is common to take 5% for the flow fraction through the bypass region although it is not known precisely.

References

[20]

Value

61.5×10^6

Units

kg/hr

Pages

3

Source 8 — Fuel Pellet Radius

This information is reported on the Fuel Lattice worksheet (Source 4). The fuel pellet radius is calculated in the spreadsheet with the following formula:

$$R_f = \frac{0.3088\,\text{in}}{2} \cdot 2.54\frac{\text{cm}}{\text{in}} = 0.39218\,\text{cm}$$

It can be inferred that the diameter of the fuel pellet that this radius was derived as was 0.3088 in.

References

[18]

Value

0.39218

Units

cm

Pages

5, 23, 24

Source 9 — Fuel Cladding Inner Radius

This information is reported on the Fuel Lattice worksheet (Source 4). The fuel rod inner radius is calculated in the spreadsheet with the following formula:

$$R_{IR} = \frac{0.36\,\text{in} - 0.0225\,\text{in} \cdot 2}{2} \cdot 2.54\frac{\text{cm}}{\text{in}} = 0.40005\,\text{cm}$$

It can be inferred that the cladding thickness is 0.0225 in.

References

[18]

Value

0.40005

Units

cm

Pages

5, 6, 23, 24

Source 10 — Fuel Cladding Outer Radius

This information is reported on the Fuel Lattice worksheet (Source 4). The fuel rod outer radius given is calculated in the spreadsheet with the following formula:

$$R_{OR} = \frac{0.36\,\text{in}}{2} \cdot 2.54\frac{\text{cm}}{\text{in}} = 0.45720\,\text{cm}$$

It can be inferred that the diameter of the fuel rod is 0.36 in.

References

[18]

Value

0.45720

Units

cm

Pages

5, 6, 23, 24

Source 11 — Plenum Spring Radius

The radius for the mass of Inconel approximating the plenum spring is chosen to be the equivalent radius for the volume of an approximate helical spring. The spring wire diameter d_{spgw} and number of turns v_s for the helical spring are taken from the FRAPCON-3 Integral Assessment Document in the appendix regarding the Westinghouse BR-3 fuel rods, which are assumed to be similar to the fuel rods in this plant. The helix diameter d_{spg} was chosen such that the ratio of the outer fuel rod cladding diameter d_{co} to the helix diameter was the same.

$$v_s = 8\,\text{turns}$$
$$d_{co,BR-3} = 0.422\,\text{in}$$
$$d_{spg,BR-3} = 0.37\,\text{in}$$

$$d_{spg} = d_{co}\frac{d_{spg,BR-3}}{d_{co,BR-3}} = 0.3156\,\text{in}$$

From here volume of the helical spring is calculated as

$$V_{spring} = v_s\pi\left(\frac{d_{spgw}}{2}\right)^2\pi\left(d_{dspg} - d_{spgw}\right)$$
$$V_{spring} = 8\pi\left(\frac{0.055\,\text{in}}{2}\right)^2\pi(0.3156\,\text{in} - 0.055\,\text{in})$$
$$V_{spring} = 0.01556\,\text{in}^3$$

Finally, the equivalent radius r_e is found with the plenum height $h_{pl} = 7.66\,\text{in}$ as

$$r_e = \sqrt{\frac{V_{spring}}{\pi h_{pl}}}$$
$$r_e = \sqrt{\frac{0.01556\,\text{in}^3}{\pi 7.66\,\text{in}}}$$
$$r_e = 0.02543\,\text{in}$$
$$r_e = 0.06459\,\text{cm}$$

References

[21]

Value

0.06459

Units

cm

Pages

6

Source 12 — RCCA Plenum Spring Radius

The plenum spring radius used in the control rod plenum was assumed to be the same as radius used for fuel pins. This makes no attempt to conform to the true volume of inconel in this region.

Value

0.06459

Units

cm

Pages

12

Source 13 — Guide Tube Inner Radius

This information is reported on the Fuel Lattice worksheet (Source 4). The guide tube inner radius is calculated in the spreadsheet with the following formula:

$$R_{IR} = \frac{0.442\,\text{in}}{2} \cdot 2.54 \frac{\text{cm}}{\text{in}} = 0.56134\,\text{cm}$$

It can be inferred that the inner diameter of the guide tube is 0.442 in. Note that this dimension is also used for instrumentation tubes.

References

[18]

Value

0.56134

Units

cm

Pages

6, 7, 9, 10, 11, 12

Source 14 — Guide Tube Outer Radius

This information is reported on the Fuel Lattice worksheet (Source 4). The guide tube outer radius is calculated in the spreadsheet with the following formula:

$$R_{OR} = \frac{0.474\,\text{in}}{2} \cdot 2.54\frac{\text{cm}}{\text{in}} = 0.60198\,\text{cm}$$

It can be inferred that the outer diameter of the guide tube is 0.474 in. Note that this dimension is also used for instrumentation tubes.

References

[18]

Value

0.60198

Units

cm

Pages

6, 7, 9, 10, 11, 12

Source 15 — Guide Tube Inner Radius at Dashpot

This information is reported on the Fuel Lattice worksheet (Source 4). The guide tube inner radius is calculated in the spreadsheet with the following formula:

$$R_{IR} = \frac{0.397\,\text{in}}{2} \cdot 2.54\frac{\text{cm}}{\text{in}} = 0.50419\,\text{cm}$$

It can be inferred that the inner diameter of the guide tube is 0.397 in.

References

[18]

Value

0.50419

Units

cm

Pages

7

Source 16 — Guide Tube Outer Radius at Dashpot

This information is reported on the Fuel Lattice worksheet (Source 4). The guide tube outer radius is calculated in the spreadsheet with the following formula:

$$R_{OR} = \frac{0.43\,\text{in}}{2} \cdot 2.54\frac{\text{cm}}{\text{in}} = 0.54610\,\text{cm}$$

It can be inferred that the outer diameter of the guide tube at dashpot is 0.43 in.

References

[18]

Value

0.54610

Units

cm

Pages

7

Source 17 — Instrumentation Tube Thimble Inner Radius

The instrumentation tube thimble inner radius was not reported in the spreadsheet. It is assumed that this dimension is the same as the burnable poison outer cladding inner radius (Source 23).

References

[18]

Value

0.43688

Units

cm

Pages

7, 8

Source 18 — Instrumentation Tube Thimble Outer Radius

The instrumentation tube thimble outer radius is not reported in the spreadsheet. It is assumed that this dimension is the same as the burnable poison outer cladding inner radius (Source 24).

References

[18]

Value

0.48387

Units

cm

Pages

7, 8

Source 19 — Inner Cladding Inner Radius of BP Pin

The Burnable Poison (BP) inner cladding inner radius is reported in the Fuel Lattice worksheet (Source 4). This number was calculated with the following formula:

$$R_{ICIR} = 0.08425 \, \text{in} \cdot 2.54 \frac{\text{cm}}{\text{in}} = 0.21400 \, \text{cm}$$

References

[18]

Value

0.21400

Units

cm

Pages

9, 10

Source 20 — Inner Cladding Outer Radius of BP Pin

The BP inner cladding outer radius is reported in the Fuel Lattice worksheet (Source 4). This number was calculated with the following formula:

$$R_{ICOR} = 0.09075 \, \text{in} \cdot 2.54 \frac{\text{cm}}{\text{in}} = 0.23051 \, \text{cm}$$

References

[18]

Value

0.23051

Units

cm

Pages

9, 10

Source 21 — Inner Radius of Poison of BP Pin

The BP inner radius is reported in the Fuel Lattice worksheet (Source 4). This number was calculated with the following formula:

$$R_{PIR} = 0.095\,\text{in} \cdot 2.54\,\frac{\text{cm}}{\text{in}} = 0.24130\,\text{cm}$$

References

[18]

Value

0.24130

Units

cm

Pages

9

Source 22 — Outer Radius of Poison of BP Pin

The BP outer radius is reported in the Fuel Lattice worksheet (Source 4). This number was calculated with the following formula:

$$R_{POR} = 0.168 \, \text{in} \cdot 2.54 \frac{\text{cm}}{\text{in}} = 0.42672 \, \text{cm}$$

References

[18]

Value

0.42672

Units

cm

Pages

9

Source 23 — Outer Cladding Inner Radius of BP Pin

The BP outer cladding inner radius is reported in the Fuel Lattice worksheet (Source 4). This number was calculated with the following formula:

$$R_{OCIR} = 0.172\,\text{in} \cdot 2.54\frac{\text{cm}}{\text{in}} = 0.43688\,\text{cm}$$

References

[18]

Value

0.43688

Units

cm

Pages

9, 10, 94

Source 24 — Outer Cladding Outer Radius of BP Pin

The BP outer cladding outer radius is reported in the Fuel Lattice worksheet (Source 4). This number was calculated with the following formula:

$$R_{OCOR} = 0.1905\,\text{in} \cdot 2.54\,\frac{\text{cm}}{\text{in}} = 0.48387\,\text{cm}$$

References

[18]

Value

0.48387

Units

cm

Pages

9, 10, 95

Source 25 — Control Rod Thimble Inner Radius

The control rod thimble inner radius was taken from page 15 of [15].

References

[15]

Value

0.38608

Units

cm

Pages

11, 12

Source 26 — Control Rod Thimble Outer Radius

The control rod thimble outer radius was taken from page 15 of [15].

References

[15]

Value

0.48387

Units

cm

Pages

11, 12

Source 27 — Control Rod AIC Outer Radius

The control rod outer radius for the lower absorber region was taken from page 15 of [15].

References

[15]

Value

0.38227

Units

cm

Pages

11

Source 28 — Control Rod B4C Outer Radius

The control rod outer radius for the upper absorber region was taken from page 15 of [15].

References

[15]

Value

0.37338

Units

cm

Pages

11

Source 29 — Control Rod Spacer Outer Radius

The control rod outer radius for the spacer region was taken from page 15 of [15].

References

[15]

Value

0.37845

Units

cm

Pages

12

Source 30 — Fuel Assembly Pitch

The fuel assembly pitch is taken from the Fuel Lattice worksheet (Source 4). The formula for calculating this parameter is

$$S_a = 8.466\,\text{in} \cdot 2.54\frac{\text{cm}}{\text{in}} = 21.50364\,\text{cm}$$

References

[18]

Value

21.50364

Units

cm

Pages

13, 24

Source 31 — Fuel Pin Pitch

The fuel pin pitch is taken from the Fuel Lattice worksheet (Source 4). The formula for calculating this parameter is

$$S_p = 0.496\,\text{in} \cdot 2.54\,\frac{\text{cm}}{\text{in}} = 1.25984\,\text{cm}$$

References

[18]

Value

1.25984

Units

cm

Pages

13

Source 32 — Inconel Grid Weight

Taken from email correspondence with an engineer at the utility. The weight of Inconel-718 for one end grid spacer is 332 lbs. The following formula is used to calculate the weight of Inconel per top/bottom grid:

$$W_{in} = 332\,\text{lb} \cdot 453.59237\frac{\text{g}}{\text{lb}} \cdot \frac{1}{193\,\text{assemblies}} = 780.273\,\text{g}.$$

References

[20]

Value

780.273

Units

g

Pages

13

Source 33 — Zircaloy Grid Weight

Taken from email correspondence with an engineer at the utility. The weight of Zircaloy-4 for the grid spacers is 2985 lbs. The following formula is used to calculate the weight of Zircaloy-4 per intermediate grid:

$$W_{zr} = 2985\,\text{lb} \cdot 453.59237\,\frac{\text{g}}{\text{lb}} \cdot \frac{1}{193\,\text{assemblies}} \cdot \frac{1}{6\,\text{grids}} = 1,169.23\,\text{g}.$$

References

[20]

Value

1,169.23

Units

g

Pages

13

Source 34 — Stainless Steel Grid Weight

Calculated from the volume of steel reported in Table 2-2 in [15] (11.3366cm^3) and the density of SS304 ρ_{SS304} (8.03g/cm^3).

References

[15]

Value

91.0329

Units

g

Pages

13

Source 35 — Burnable Poison Specifications

Taken from the data spreadsheet provided by the utility, on the sheet named BP Arrangement.

References

[18]

Pages

14, 15, 16, 17, 18, 19, 20, 21, 22

Source 36 — Grid Spacers

The axial positioning of the grid centers was taken from the Fuel Lattice worksheet. Upper and lower planes for each grid were found using the grid heights specified in [15].

The masses for determining radial grid spacer dimensions are taken from Sources 32, 33, and 34.

Top/Bottom Grid Sleeve

As shown in Figure 25, the grid sleeve is a box shell defined by inner and outer square pitch parameters P_i and P_o, where P_i is found using the pin pitch as $17 \times S_p$. Using the density of SS304 ρ_{SS304}, the estimated mass for each grid W_{SS304}, and the height of the grid, the outer pitch is found as:

$$P_o = \sqrt{P_i^2 + \frac{W_{SS304}/\rho_{SS304}}{h_{tb}}} = \sqrt{(17 \times 1.25984\,\text{cm})^2 + \frac{91.0329\,\text{g}/8.03\,\frac{\text{g}}{\text{cm}^3}}{1.322\,\text{in} \times 2.54\,\frac{\text{cm}}{\text{in}}}}$$

$$= 21.4960\,\text{cm}$$

This fits between assemblies, as P_o is less than the assembly pitch (21.50364 cm). The square radius reported in Figure 25 is half of P_o.

Top/Bottom Egg-Crate

As shown in Figure 23, the egg-crate is defined by a box shell defined by inner and outer square pitch parameters p_i and p_o, where p_o is simply the outer pincell pitch S_p. It is assumed that the entire mass of Inconel reported from Source 32 is uniformly distributed between all pincells in an assembly. Thus the mass of Inconel per pincell is $w_{in} = \frac{W_{in}}{17 \times 17} = 2.69990\,\text{g}$. Using this with the density of Inconel ρ_{in} and the height of the grid, the inner pitch is found as:

$$p_i = \sqrt{p_o^2 - \frac{w_{in}/\rho_{in}}{h_{tb}}} = \sqrt{(1.25984\,\text{cm})^2 - \frac{2.69990\,\text{g}/8.2\,\frac{\text{g}}{\text{cm}^3}}{1.322\,\text{in} \times 2.54\,\frac{\text{cm}}{\text{in}}}}$$

$$= 1.22030\,\text{cm}$$

This fits between the pin and outer pincell pitch for all pincell types, as p_i is greater than the guide tube diameter (1.20396 cm). The square radius reported in Figure 23 is half of p_i.

Intermediate Grid Sleeve

The dimensions for the intermediate grid sleeves are taken to be identical to those for the top/bottom grid sleeves.

Intermediate Egg-Crate

The intermediate grid egg-crate dimensions are found in the same way as the top/bottom grids, using the appropriate Zircaloy masses and densities. Here, the weight of Zircaloy $w_{zr,egg}$ used to calculate the egg-crate dimensions is the total grid weight of Zircaloy W_{zr} from Source 33, less the weight of Zircaloy in the intermediate grid sleeve $w_{zr,sleeve}$, divided by the number of pincells. The weight in the sleeve is found using the density of Zircaloy and the volume of the sleeve from the intermediate grid height and the previously-calculated grid sleeve pitch parameters.

$$
\begin{aligned}
w_{zr,sleeve} &= \rho_{zr} h_{int} \left(P_o^2 - P_i^2 \right) \\
&= 6.55 \frac{\text{g}}{\text{cm}^3} \times 2.25\,\text{in} \times 2.54 \frac{\text{cm}}{\text{in}} \left((21.4960\,\text{cm})^2 - (21.41728\,\text{cm})^2 \right) \\
&= 126.455\,\text{g}
\end{aligned}
$$

$$
\begin{aligned}
w_{zr,egg} &= \frac{1}{17 \times 17} \left(W_{zr} - w_{zr,sleeve} \right) \\
w_{zr,egg} &= \frac{1}{17 \times 17} (1169.23\,\text{g} - 126.455\,\text{g}) \\
w_{zr,egg} &= 3.60850\,\text{g}
\end{aligned}
$$

$$
p_i = \sqrt{p_o^2 - \frac{w_{zr,egg}/\rho_{zr}}{h_{int}}} = \sqrt{(1.25984\,\text{cm})^2 - \frac{3.60850\,\text{g}/6.55\frac{\text{g}}{\text{cm}^3}}{2.25\,\text{in} \times 2.54\frac{\text{cm}}{\text{in}}}}
$$
$$
= 1.22098\,\text{cm}
$$

This fits between the pin and outer pincell pitch for all pincell types, as p_i is greater than the guide tube diameter (1.20396 cm). The square radius reported in Figure 24 is half of p_i.

References

[18] [15]

Pages

23, 24, 34, 35, 36, 37

Source 37 — Core Baffle Thickness

Taken from email correspondence with an engineer at the utility. The core baffle is 7/8 inches thick. Converting this to centimeters:

$$T_{baf} = \frac{7}{8}\,\text{in} \cdot 2.54\frac{\text{cm}}{\text{in}} = 2.22250\,\text{cm}$$

References

[20]

Value

2.22250

Units

cm

Pages

26

Source 38 — Core Barrel Inner Radius

Taken from email corresponding with an engineer at the utility. The inner diameter of the core barrel is 148.0 inches. The inner radius of the core barrel is calculated to be

$$R_{bar} = \frac{148.0 \, \text{in}}{2} \cdot 2.54 \frac{\text{cm}}{\text{in}} = 187.96 \, \text{cm}$$

References

[20]

Value

187.96

Units

cm

Pages

26

Source 39 — Core Barrel Outer Radius

Taken from email correspondence with an engineer at the utility. The outer diameter of the core barrel is 152.5 inches. The outer radius of the core barrel is calculated to be

$$R_{bar} = \frac{152.5\,\text{in}}{2} \cdot 2.54\,\frac{\text{cm}}{\text{in}} = 193.675\,\text{cm}$$

References

[20]

Value

193.675

Units

cm

Pages

26

Source 40 — Core Barrel Material

From email correspondence with the utility, the core barrel is made out of Stainless Steel 304.

References

[20]

Pages

26

Source 41 — RPV, Liner, and Shield Panels

Core structural dimensions were taken from [15], with the exception of the baffle and core barrel dimensions that were provided by engineers at the utility. The water gap between fuel assemblies and the baffle was also taken from [15], which also indicates the material as Stainless Steel 304.

References

[15]

Pages

26

Source 42 — Instrument Tube Axial Planes

The instrument tube thimble penetrates the bottom of the reactor vessel and extends to the end of guide tubes at the bottom of the upper nozzle. The source for these planes is described in Source 47.

Pages

36

Source 43 — Burnable Absorber Axial Planes

Burnable absorbers are inserted from the top of assemblies with a spider assembly similar to those that hold control rods. The burnable absorber axial planes were set to be consistent with [15], Figure 2-9.

References

[15]

Pages

37

Source 44 — Guide Tube Axial Planes

The guide tubes are the structural components of the assemblies, connecting the top of the lower nozzle to the bottom of the upper nozzle. The dashpot axial plane is placed at the control rod step 0 (see Source 45).

Pages

35, 37

Source 45 — Control Rod Axial Planes

The control rod axial planes for full insertion were set to be consistent with [15], Figure 2-8. The step width of 1.582cm was calculated by dividing the active absorbing height (142 in.) by 228.

References

[18] [15]

Pages

38, 122

Source 46 — Assembly Nozzles

Upper nozzle and water gap axial spacings were estimated from the Watts Bar Unit 2 Safety Analysis Report, Section 4, Figure 4.2-2.

References

[22]

Pages

34, 35, 36, 37, 41

Source 47 — Fuel Rod Axial Planes

Fuel rod axial planes were set to be consistent with [15], Figure 2-7.

References

[15]

Pages

26, 34, 120

Source 48 — Location of Instrument Tubes

The locations of the instrumentation tubes were inferred from HZP detector measurement files. There are 58 locations in various locations around the core.

References

[23]

Pages

32

Source 49 — 1.6% Enriched Fuel Composition

Provided in the spreadsheet sent by the utility the initial Uranium heavy metal mass and U-235 mass are detailed for each assembly under the worksheet, Assembly Loading. These allow us to calculate U-235 enrichments and fuel density. To limit the number of materials, the average values for the enrichments were calculated.

Using the detailed assembly loadings, the actual core-averaged enrichment for the cycle 1 low-enriched bundles is $\chi_{25} = 1.61006\%$ (see Source 70). It assumed that the enrichment of U-234 is 0.8% of this,

$$\chi_{24} = 0.008 \cdot 1.61006\% = 0.01288048\%.$$

The rest of the heavy metal in the initial fuel loading is made up of U-238 calculated as

$$\chi_{28} = 100\% - 1.61006\% - 0.01288048\% = 98.37705952\%.$$

The atomic mass of Uranium can be calculated from these weight percents of Uranium isotopes and the isotopic masses taken from Source 67:

$$M_U = \left[\frac{\chi_{24}}{M_{24}} + \frac{\chi_{25}}{M_{25}} + \frac{\chi_{28}}{M_{28}} \right]^{-1} = 238.001241436 \, \text{amu}.$$

The weight fractions of Uranium in Uranium Dioxide and Oxygen in Uranium Dioxide can be determined by the following two expressions:

$$\omega_U = \frac{M_U}{M_U + 2 \cdot M_O} = 0.881485944114$$

and

$$\omega_O = 1 - \omega_U = 0.118514055886.$$

From the Uranium heavy metal weight percent, and detailed heavy metal loadings reported in the spreadsheet, the average density can be calculated. The total Uranium heavy metal mass for low enriched bundles is $m_f = 27.570971 \, \text{MT}$ (see Source 70). If there are 65 low enriched bundles, the volume can be calculated with

$$V_f = \pi \cdot R_f^2 \cdot H \cdot N_{assy} \cdot N_{pins}$$

$$V_f = \pi \cdot 0.39218^2 \cdot 365.76 \cdot 65 \cdot 264 = 3032733.5050 \, \text{cm}^3.$$

See Sources 8, 5 and Figures 14 and 27.

The fuel density can be calculated by computing the Uranium heavy metal density and dividing by its fractional weight

$$\rho_f = \frac{m_f}{V_f \cdot \omega_U} = 10.31341 \; \frac{\text{g}}{\text{cm}^3}.$$

Isotopic number densities for Uranium are then calculated with

$$N = \frac{\widetilde{\rho} \cdot A}{M}.$$

The parameter A is Avagadro's number $= 0.60221415 \cdot 10^{24} \frac{atom}{mol}$ and $\widetilde{\rho}$ is the isotopic mass density. The isotopic mass density is calculated by multiplying the weight fraction of the element by the weight fraction of the isotopic in that element ($\omega \cdot \chi$) multiplied by the fuel mass density,

$$\widetilde{\rho} = \rho_f \cdot \omega \cdot \chi.$$

For oxygen, the total number density of oxygen is calculated with

$$N_O = \frac{\rho_f \cdot \omega_O \cdot A}{M_O}.$$

Isotopic number densities are then determined by multiplying by fractional abundances provided in Source 68.

References

[18]

Pages

43

Source 50 — 2.4% Enriched Fuel Composition

Provided in the spreadsheet sent by the utility the initial Uranium heavy metal mass and U-235 mass are detailed for each assembly under the worksheet, Assembly Loading. These allow us to calculate U-235 enrichments and fuel density. To limit the number of materials, the average values for the enrichments were calculated.

Using the detailed assembly loadings, the actual core-averaged enrichment for the cycle 1 medium-enriched bundles is $\chi_{25} = 2.39993\%$ (see Source 70). It assumed that the enrichment of U-234 is 0.8% of this,

$$\chi_{24} = 0.008 \cdot 2.39993\% = 0.01919944\%.$$

The rest of the heavy metal in the initial fuel loading is made up of U-238 calculated as

$$\chi_{28} = 100\% - 2.39993\% - 0.01919944\% = 97.58087056\%.$$

The atomic mass of Uranium can be calculated from these weight percents of Uranium isotopes and the isotopic masses taken from Source 67:

$$M_U = \left[\frac{\chi_{24}}{M_{24}} + \frac{\chi_{25}}{M_{25}} + \frac{\chi_{28}}{M_{28}} \right]^{-1} = 237.976942215 \,\text{amu}.$$

The weight fractions of Uranium in Uranium Dioxide and Oxygen in Uranium Dioxide can be determined by the following two expressions:

$$\omega_U = \frac{M_U}{M_U + 2 \cdot M_O} = 0.881475277232$$

and

$$\omega_O = 1 - \omega_U = 0.118524722768.$$

From the Uranium heavy metal weight percent, and detailed heavy metal loadings reported in the spreadsheet, the average density can be calculated. The total Uranium heavy metal mass for medium enriched bundles is $m_f = 27.104522 \,\text{MT}$ (see Source 70). If there are 64 medium enriched bundles, the volume can be calculated with

$$V_f = \pi \cdot R_f^2 \cdot H \cdot N_{assy} \cdot N_{pins}$$

$$V_f = \pi \cdot 0.39218^2 \cdot 365.76 \cdot 64 \cdot 264 = 2986076.0665 \,\text{cm}^3.$$

See Sources 8, 5 and Figures 14 and 27.

The fuel density can be calculated by computing the Uranium heavy metal density and dividing by its fractional weight

$$\rho_f = \frac{m_f}{V_f \cdot \omega_U} = 10.29748 \, \frac{\text{g}}{\text{cm}^3}.$$

Isotopic number densities for Uranium are then calculated with

$$N = \frac{\widetilde{\rho} \cdot A}{M}.$$

The parameter A is Avagadro's number $= 0.60221415 \cdot 10^{24} \, \frac{atom}{mol}$ and $\widetilde{\rho}$ is the isotopic mass density. The isotopic mass density is calculated by multiplying the weight fraction of the element by the weight fraction of the isotopic in that element ($\omega \cdot \chi$) multiplied by the fuel mass density,

$$\widetilde{\rho} = \rho_f \cdot \omega \cdot \chi.$$

For oxygen, the total number density of oxygen is calculated with

$$N_O = \frac{\rho_f \cdot \omega_O \cdot A}{M_O}.$$

Isotopic number densities are then determined by multiplying by fractional abundances provided in Source 68.

References

[18]

Pages

44

Source 51 — 3.1% Enriched Fuel Composition

Provided in the spreadsheet sent by the utility the initial Uranium heavy metal mass and U-235 mass are detailed for each assembly under the worksheet, Assembly Loading. These allow us to calculate U-235 enrichments and fuel density. To limit the number of materials, the average values for the enrichments were calculated.

Using the detailed assembly loadings, the actual core-averaged enrichment for the cycle 1 high-enriched bundles is $\chi_{25} = 3.10221\%$ (see Source 70). It assumed that the enrichment of U-234 is 0.8% of this,

$$\chi_{24} = 0.008 \cdot 3.10221\% = 0.02481768\%.$$

The rest of the heavy metal in the initial fuel loading is made up of U-238 calculated as

$$\chi_{28} = 100\% - 3.10221\% - 0.02481768\% = 96.87297232\%.$$

The atomic mass of Uranium can be calculated from these weight percents of Uranium isotopes and the isotopic masses taken from Source 67:

$$M_U = \left[\frac{\chi_{24}}{M_{24}} + \frac{\chi_{25}}{M_{25}} + \frac{\chi_{28}}{M_{28}} \right]^{-1} = 237.955341741 \, \text{amu}.$$

The weight fractions of Uranium in Uranium Dioxide and Oxygen in Uranium Dioxide can be determined by the following two expressions:

$$\omega_U = \frac{M_U}{M_U + 2 \cdot M_O} = 0.881464534041$$

and

$$\omega_O = 1 - \omega_U = 0.118535465959.$$

From the Uranium heavy metal weight percent, and detailed heavy metal loadings reported in the spreadsheet, the average density can be calculated. The total Uranium heavy metal mass for high enriched bundles is $m_f = 27.115256 \, \text{MT}$ (see Source 70). If there are 64 high enriched bundles, the volume can be calculated with

$$V_f = \pi \cdot R_f^2 \cdot H \cdot N_{assy} \cdot N_{pins}$$

$$V_f = \pi \cdot 0.39218^2 \cdot 365.76 \cdot 64 \cdot 264 = 2986076.0665 \, \text{cm}^3.$$

See Sources 8, 5 and Figures 14 and 27.

The fuel density can be calculated by computing the Uranium heavy metal density and dividing by its fractional weight

$$\rho_f = \frac{m_f}{V_f \cdot \omega_U} = 10.30166 \, \frac{\text{g}}{\text{cm}^3}.$$

Isotopic number densities for Uranium are then calculated with

$$N = \frac{\widetilde{\rho} \cdot A}{M}.$$

The parameter A is Avagadro's number $= 0.60221415 \cdot 10^{24} \, \frac{atom}{mol}$ and $\widetilde{\rho}$ is the isotopic mass density. The isotopic mass density is calculated by multiplying the weight fraction of the element by the weight fraction of the isotopic in that element $(\omega \cdot \chi)$ multiplied by the fuel mass density,

$$\widetilde{\rho} = \rho_f \cdot \omega \cdot \chi.$$

For oxygen, the total number density of oxygen is calculated with

$$N_O = \frac{\rho_f \cdot \omega_O \cdot A}{M_O}.$$

Isotopic number densities are then determined by multiplying by fractional abundances provided in Source 68.

References

[18]

Pages

44

Source 52 — 3.2% Enriched Fuel Composition

Provided in the spreadsheet sent by the utility the initial Uranium heavy metal mass and U-235 mass are detailed for each assembly under the worksheet, Assembly Loading. These allow us to calculate U-235 enrichments and fuel density. To limit the number of materials, the average values for the enrichments were calculated.

Using the detailed assembly loadings, the actual average enrichment for these fresh assemblies is $\chi_{25} = 3.19547\%$ (see Source 71). It assumed that the enrichment of U-234 is 0.8% of this,

$$\chi_{24} = 0.008 \cdot 3.19547\% = 0.02556376\%.$$

The rest of the heavy metal in the initial fuel loading is made up of U-238 calculated as

$$\chi_{28} = 100\% - 3.19547\% - 0.02556376\% = 96.77896624\%.$$

The atomic mass of Uranium can be calculated from these weight percents of Uranium isotopes and the isotopic masses taken from Source 67:

$$M_U = \left[\frac{\chi_{24}}{M_{24}} + \frac{\chi_{25}}{M_{25}} + \frac{\chi_{28}}{M_{28}} \right]^{-1} = 237.952473579 \, \text{amu}.$$

The weight fractions of Uranium in Uranium Dioxide and Oxygen in Uranium Dioxide can be determined by the following two expressions:

$$\omega_U = \frac{M_U}{M_U + 2 \cdot M_O} = 0.881465793436$$

and

$$\omega_O = 1 - \omega_U = 0.118535465959.$$

From the Uranium heavy metal weight percent, and detailed heavy metal loadings reported in the spreadsheet, the average density can be calculated. The total Uranium heavy metal mass for high enriched bundles is $m_f = 20.414365 \, \text{MT}$ (see Source 71). If there are 48 bundles, the volume can be calculated with

$$V_f = \pi \cdot R_f^2 \cdot H \cdot N_{assy} \cdot N_{pins}$$

$$V_f = \pi \cdot 0.39218^2 \cdot 365.76 \cdot 48 \cdot 264 = 2239557.0499 \, \text{cm}^3.$$

See Sources 8, 5 and Figures 14 and 29.

The fuel density can be calculated by computing the Uranium heavy metal density and dividing by its fractional weight

$$\rho_f = \frac{m_f}{V_f \cdot \omega_U} = 10.34115 \ \frac{\text{g}}{\text{cm}^3}.$$

Isotopic number densities for Uranium are then calculated with

$$N = \frac{\widetilde{\rho} \cdot A}{M}.$$

The parameter A is Avagadro's number $= 0.60221415 \cdot 10^{24} \ \frac{atom}{mol}$ and $\widetilde{\rho}$ is the isotopic mass density. The isotopic mass density is calculated by multiplying the weight fraction of the element by the weight fraction of the isotopic in that element ($\omega \cdot \chi$) multiplied by the fuel mass density,

$$\widetilde{\rho} = \rho_f \cdot \omega \cdot \chi.$$

For oxygen, the total number density of oxygen is calculated with

$$N_O = \frac{\rho_f \cdot \omega_O \cdot A}{M_O}.$$

Isotopic number densities are then determined by multiplying by fractional abundances provided in Source 68.

References

[18]

Pages

iii, 45

Source 53 — 3.4% Enriched Fuel Composition

Provided in the spreadsheet sent by the utility the initial Uranium heavy metal mass and U-235 mass are detailed for each assembly under the worksheet, Assembly Loading. These allow us to calculate U-235 enrichments and fuel density. To limit the number of materials, the average values for the enrichments were calculated.

Using the detailed assembly loadings, the actual core-averaged enrichment for these fresh assemblies is $\chi_{25} = 3.40585\%$ (see Source 71). It assumed that the enrichment of U-234 is 0.8% of this,

$$\chi_{24} = 0.008 \cdot 3.40585\% = 0.02724680\%.$$

The rest of the heavy metal in the initial fuel loading is made up of U-238 calculated as

$$\chi_{28} = 100\% - 3.40585\% - 0.02724680\% = 96.56690320\%.$$

The atomic mass of Uranium can be calculated from these weight percents of Uranium isotopes and the isotopic masses taken from Source 67:

$$M_U = \left[\frac{\chi_{24}}{M_{24}} + \frac{\chi_{25}}{M_{25}} + \frac{\chi_{28}}{M_{28}} \right]^{-1} = 237.946003706, \text{amu}.$$

The weight fractions of Uranium in Uranium Dioxide and Oxygen in Uranium Dioxide can be determined by the following two expressions:

$$\omega_U = \frac{M_U}{M_U + 2 \cdot M_O} = 0.881461693055$$

and

$$\omega_O = 1 - \omega_U = 0.118538306945.$$

From the Uranium heavy metal weight percent, and detailed heavy metal loadings reported in the spreadsheet, the average density can be calculated. The total Uranium heavy metal mass for high enriched bundles is $m_f = 6.816624 \, \text{MT}$ (see Source 71). If there are 16 bundles, the volume can be calculated with

$$V_f = \pi \cdot R_f^2 \cdot H \cdot N_{assy} \cdot N_{pins}$$

$$V_f = \pi \cdot 0.39218^2 \cdot 365.76 \cdot 16 \cdot 264 = 746519.0166 \, \text{cm}^3.$$

See Sources 8, 5 and Figures 14 and 29.

The fuel density can be calculated by computing the Uranium heavy metal density and dividing by its fractional weight

$$\rho_f = \frac{m_f}{V_f \cdot \omega_U} = 10.35917 \, \frac{\text{g}}{\text{cm}^3}.$$

Isotopic number densities for Uranium are then calculated with

$$N = \frac{\widetilde{\rho} \cdot A}{M}.$$

The parameter A is Avagadro's number $= 0.60221415 \cdot 10^{24} \, \frac{atom}{mol}$ and $\widetilde{\rho}$ is the isotopic mass density. The isotopic mass density is calculated by multiplying the weight fraction of the element by the weight fraction of the isotopic in that element $(\omega \cdot \chi)$ multiplied by the fuel mass density,

$$\widetilde{\rho} = \rho_f \cdot \omega \cdot \chi.$$

For oxygen, the total number density of oxygen is calculated with

$$N_O = \frac{\rho_f \cdot \omega_O \cdot A}{M_O}.$$

Isotopic number densities are then determined by multiplying by fractional abundances provided in Source 68.

References

[18]

Pages

iii, 45

Source 54 — Composition of Air

The density of air was referenced from Engineering toolbox at 300 C to be $\rho_{air} = 0.000616$ g/cc. The composition of air included here contains Oxygen, Nitrogen, Argon and Carbon. Note that Hydrogen, Neon, Helium, Krypton and Xenon were all neglected as they contribute very little. Abundances were gathered from Engineering Toolbox and are listed below.

Element	Fractional Abundance	Element	Fractional Abundance
O	0.2095	N	0.7809
Ar	0.00933	C	0.00027[†]

† Carbon adjusted slightly so sum is unity.

Using these abundances and elemental masses in Source 69, the mass of air can be calculated with

$$M_{air} = \sum_i \alpha_i M_i = 14.6657850715 \, \text{amu},$$

where α represents the abundance fraction. The total number density of air can be calculated with

$$N_{air} = \frac{\rho_{air} \cdot A}{M_{air}} = 2.52945147219 \times 10^{-5} \, \frac{\text{atom}}{\text{barn} \cdot \text{cm}}.$$

The parameter A is Avagadro's number $= 0.60221415 \cdot 10^{24} \, \frac{atom}{mol}$. Elemental number densities can be calculated by multiplying the number density of air by their respective abundances,

$$N_i = \alpha_i \cdot N_{air}.$$

Similarly, the isotopic number densities can be calculated by multiplying the elemental number densities by isotopic abundances reported in Source 68.

References

[24]

Pages

46

Source 55 — Composition of Borosilicate Glass

The density of Borosilicate glass was referenced from the CASMO-4 manual to be $\rho_{bp} = 2.26$ g/cc. The composition, according to the manual is

Element/Isotope	Weight Fraction	Element/Isotope	Weight Fraction
O	0.5481	Al	0.0344
Si	0.3787	B-10	0.0071
B-11	0.0317		

The relative weight fractions of B-10 and B-11 in Boron can be calculated using the absolute weight fractions above,

$$\chi_{50} = \frac{\omega_{50}}{\omega_{50} + \omega_{51}} \qquad \chi_{51} = \frac{\omega_{51}}{\omega_{50} + \omega_{51}}.$$

The elemental mass of Boron can be done using isotopic masses in Source 67,

$$M_B = \left[\frac{\chi_{50}}{M_{50}} + \frac{\chi_{51}}{M_{51}} \right]^{-1} = 10.812422457829642 \, \text{amu}.$$

To compute the number densities of the elements/isotopes listed in the table above, the following formula can be used:

$$N_i = \frac{\omega_i \cdot \rho_{bp} \cdot A}{M_i}.$$

The parameter A is Avagadro's number $= 0.60221415 \cdot 10^{24} \frac{atom}{mol}$. The isotopic number densities of the elements listed in the table can be calculated by multiplying the elemental number densities by isotopic abundances reported in Source 68.

References

[25]

Pages

46

Source 56 — Composition of Ag-In-Cd Control Rods

The density of Ag-In-Cd control rods was referenced from the CASMO-4 manual to be $\rho_{cr} = 10.16$ g/cc. The composition, as given in the manual is 80% Ag, 15% In and 5% Cd.

Using these weight percents and elemental masses from Source 69, the number densities of each element can be calculated with.

$$N_i = \frac{\omega_i \cdot \rho_{cr} \cdot A}{M_i}.$$

The parameter A is Avagadro's number $= 0.60221415 \cdot 10^{24} \frac{atom}{mol}$. The isotopic number densities of the elements listed in the table can be calculated by multiplying the elemental number densities by isotopic abundances reported in Source 68.

References

[25]

Pages

3, 47

Source 57 — Composition of B4C Control Rods

The density of B4C control rods was referenced from the CASMO-4 manual to be $\rho_{cr} = 1.76$ g/cc. The composition, as given in the manual is 78.26% B and 21.74% C.

Using these weight percents and elemental masses from Source 69, the number densities of each element can be calculated with.

$$N_i = \frac{\omega_i \cdot \rho_{cr} \cdot A}{M_i}.$$

The parameter A is Avagadro's number $= 0.60221415 \cdot 10^{24} \frac{atom}{mol}$. The isotopic number densities of the elements listed in the table can be calculated by multiplying the elemental number densities by isotopic abundances reported in Source 68.

References

[25]

Pages

3, 47

Source 58 — Composition of Helium

The density of Helium gas was retrieved from NIST from a pressure of 2 MPa and temperature of 600 K. The density was given as $\rho_{He} = 0.0015981$ g/cc. The number density can be computed along with the element mass from Source 69,

$$N_{He} = \frac{\rho_{He} \cdot A}{M_{He}}.$$

The parameter A is Avagadro's number $= 0.60221415 \cdot 10^{24} \frac{atom}{mol}$.

References

[26]

Pages

48

Source 59 — Composition of Inconel

The density of Inconel-718 was referenced from the CASMO-4 manual to be $\rho_{in} = 8.2$ g/cc. The composition, according to the manual is

Element/Isotope	Weight Fraction	Element/Isotope	Weight Fraction
Si	0.0035	Cr	0.1896
Mn	0.0087	Fe	0.2863[†]
Ni	0.5119		

[†] weight fraction adjust such that sum is unity

To compute the number densities of the elements/isotopes listed in the table above, the following formula can be used:

$$N_i = \frac{\omega_i \cdot \rho_{in} \cdot A}{M_i}.$$

The parameter A is Avagadro's number $= 0.60221415 \cdot 10^{24} \frac{atom}{mol}$. The isotopic number densities of the elements listed in the table can be calculated by multiplying the elemental number densities by isotopic abundances reported in Source 68.

References

[25]

Pages

48

Source 60 — Composition of Stainless Steel

The density of Stainless Steel-304 was referenced from AK Steel Product Data Sheet to be $\rho_{ss} = 8.03$ g/cc. The composition, according to the data sheet is

Element/Isotope	Weight Fraction	Element/Isotope	Weight Fraction
Si	0.0060	Cr	0.1900
Mn	0.0200	Fe	0.6840[†]
Ni	0.1000		

[†] weight fraction adjust such that sum is unity

To compute the number densities of the elements/isotopes listed in the table above, the following formula can be used:

$$N_i = \frac{\omega_i \cdot \rho_{ss} \cdot A}{M_i}.$$

The parameter A is Avagadro's number $= 0.60221415 \cdot 10^{24} \frac{atom}{mol}$. The isotopic number densities of the elements listed in the table can be calculated by multiplying the elemental number densities by isotopic abundances reported in Source 68.

References

[27]

Pages

49

Source 61 — Composition of Zircaloy

The density of Zircaloy 4 was referenced from the CASMO-4 manual to be $\rho_{zr} = 6.55$ g/cc. The composition, according to the manual is

Element/Isotope	Weight Fraction	Element/Isotope	Weight Fraction
O	0.00125	Cr	0.0010
Fe	0.0021	Zr	0.98115[†]
Sn	0.0145		

[†] weight fraction adjust such that sum is unity

To compute the number densities of the elements/isotopes listed in the table above, the following formula can be used:

$$N_i = \frac{\omega_i \cdot \rho_{zr} \cdot A}{M_i}.$$

The parameter A is Avagadro's number $= 0.60221415 \cdot 10^{24} \frac{atom}{mol}$. The isotopic number densities of the elements listed in the table can be calculated by multiplying the elemental number densities by isotopic abundances reported in Source 68.

Pages

50

Source 62 — Composition of Borated Water

This source block describes how to compute the number density of isotopes in borated water. This block will show the necessary formulas, but the density and concentration of boron may change depending on cycle time. For a given reactor pressure and temperature, density of water is obtained from NIST. From the water density and boron weight percent, the density of borated water will be obtained.

For a given concentration of boron, the weight percent of boron in water is

$$\omega_B = C_B \, [\text{ppm}]^{-1} \times 10^{-6}.$$

The molecular mass of water can be determined from elemental masses in Source 69 as

$$M_{H_2O} = 2 \cdot M_H + M_O.$$

The number density of water can then be computed as

$$N_{H_2O} = \frac{\rho_{H_2O} \cdot A}{M_{H_2O}}.$$

The parameter A is Avagadro's number $= 0.60221415 \cdot 10^{24} \frac{atom}{mol}$. The number density of hydrogen and oxygen are given as:

$$N_H = 2 \cdot N_{H_2O} \qquad N_O = N_{H_2O}.$$

The density of borated water can be computed from the density of water and the weight percent of boron,

$$\rho_{BW} = \frac{\rho_{H_2O}}{1 - \omega_B}$$

To compute the number density of boron, the following expression is used:

$$N_B = \frac{\omega_B \cdot \rho_{BW} \cdot A}{M_B}.$$

The isotopic number densities of the elements can be calculated by multiplying the elemental number densities by isotopic abundances reported in Source 68.

References

[28]

Pages

51

Source 63 — Composition of Borated Water in Nozzle and Support Plate Region

To conserve the mass of borated water in the nozzle and support plate region, the density of borated water is adjusted using formula:

$$\rho'_{water} = \frac{\rho_{water} \times V_{water}}{V'_{water}}$$

where ρ_{water} and V_{water} are the actual density and volume of water while ρ'_{water} and V'_{water} are the density and volume in the model.

According to Section 2.3.6.2, the volume of water in the nozzle and support plate region is

$$V'_{water} = S_a^2 - n_{pins} \times \pi \times R_{pin}^2 = 21.50364^2 - 264 \times \pi \times 0.45720^2 = 289.03961 \, \text{cm}^3$$

From Reference [15], the volume fractions of water in the nozzle and support plate is 0.8280, so the actual volume of water should be:

$$V_{water} = S_a^2 \times 0.8280 = 382.87261 \, \text{cm}^3$$

The adjusted density of borated water is:

$$\rho'_{water} = 0.740582067516 \times 382.87261/289.03961 = 0.9810025 \, \text{g/cm}^3$$

The adjusted density can then be used to calculate number densities of nuclides in borated water described in Source 62.

References

[15]

Pages

51

Source 64 — Composition of Stainless Steel in Nozzle and Support Plate Region

To conserve the mass of stainless steel in the nozzle and support plate region, the density of stainless steel is adjusted using formula:

$$\rho'_{ss} = \frac{\rho_{ss} \times V_{ss}}{V'_{ss}}$$

where ρ_{ss} and V_{ss} are the actual density and volume of stainless steel while ρ'_{ss} and V'_{ss} are the density and volume in the model.

According to Section 2.3.6.2, the volume of stainless steel in the nozzle and support plate region is

$$V'_{ss} = n_{pins} \times \pi \times R^2_{pin} = 264 \times \pi \times 0.45720^2 = 173.36692 \, \text{cm}^3$$

From Reference [15], the volume fractions of stainless steel in the nozzle and support plate is 0.1720, so the actual volume of stainless steel should be:

$$V_{ss} = S^2_a \times 0.1720 = 79.533924 \, \text{cm}^3$$

The adjusted density of stainless steel is:

$$\rho'_{ss} = 8.03 \times 79.533924/173.36692 = 3.683848 \, \text{g/cm}^3$$

The adjusted density can then be used to calculate number densities of nuclides in stainless steel described in Source 60.

References

[15]

Pages

52

Source 65 — Composition of Carbon Steel

The density of Carbon Steel was assumed to be $\rho_{cs} = 7.8$ g/cc. The composition, according to the ranges in an ASTM datasheet is

Element/Isotope	Weight Fraction	Element/Isotope	Weight Fraction
C	0.00270	Mn	0.00750
P	0.00025	Si	0.00400
Mo	0.00625	Ni	0.00750
Fe	0.96487	S	0.00025
Cr	0.00350	V	0.00050
Nb	0.00010	Cu	0.00200
Ca	0.00015	B	0.00003
Ti	0.00015	Al	0.00025

To compute the number densities of the elements/isotopes listed in the table above, the following formula can be used:

$$N_i = \frac{\omega_i \cdot \rho_{cs} \cdot A}{M_i}.$$

The parameter A is Avagadro's number $= 0.60221415 \cdot 10^{24} \frac{atom}{mol}$. The isotopic number densities of the elements listed in the table can be calculated by multiplying the elemental number densities by isotopic abundances reported in Source 68.

References

[29]

Pages

53

Source 66 — Missing Data

This reference box lists all of the values that were estimated:

- Lower support plate and nozzle heights were guessed

Pages

34, 35, 36, 37, 38

Source 67 — Isotopic Masses

Isotope	Mass [amu]	Isotope	Mass [amu]
H-1	1.0078250	H-2	2.0141018
He-4	4.0026032542	B-10	10.0129370
B-11	11.0093054	C-12	12.0000000
C-13	13.003354838	O-16	15.9949146196
O-17	16.9991317	O-18	17.999161
N-14	14.003074005	N-15	15.000108898
Si-28	27.976926532	Si-29	28.97649470
Si-30	29.97377017	P-31	30.9737616
Al-27	26.9815386	Ar-36	35.96754511
Ar-38	37.9627324	Ar-40	39.962383123
Cr-50	49.946044	Cr-52	51.940507
Cr-53	52.940649	Cr-54	53.938880
Mn-55	54.938045	Fe-54	53.939611
Fe-56	55.934937	Fe-57	56.935394
Fe-58	57.933276	Ni-58	57.935343
Ni-60	59.930786	Ni-61	60.931056
Ni-62	61.928345	Ni-64	63.927966
Zr-90	89.904704	Zr-91	90.905646
Zr-92	91.905041	Zr-94	93.906315
Zr-96	95.908273	Mo-92	91.906811
Mo-94	93.905088	Mo-95	94.905842
Mo-96	95.904679	Mo-97	96.906021
Mo-98	97.905408	Mo-100	99.90748
Ag-107	106.905097	Ag-109	108.904752
Cd-106	105.90646	Cd-108	107.90418
Cd-110	109.903002	Cd-111	110.904178
Cd-112	111.902758	Cd-113	112.904402
Cd-114	113.903359	Cd-116	115.904756
In-113	112.904058	In-115	114.903878
Sn-112	111.904818	Sn-114	113.902779
Sn-115	114.903342	Sn-116	115.901741
Sn-117	116.902952	Sn-118	117.901603
Sn-119	118.903308	Sn-120	119.902195
Sn-122	121.903439	Sn-124	123.905274
U-234	234.040952	U-235	235.043930
U-238	238.050788		

References

[30]

Pages

127, 129, 131, 133, 135, 138

Source 68 — Isotopic Natural Abundances

Isotope	Fractional Abundance	Isotope	Fractional Abundance
Ag107	0.51839	Ag109	0.48161
Al27	1.0	Ar36	0.003336
Ar38	0.000629	Ar40	0.996035
B10	0.1982	B11	0.8018
C12	0.988922	C13	0.011078
Ca40	0.96941	Ca42	0.00647
Ca43	0.00135	Ca44	0.02086
Ca46	4e-05	Ca48	0.00187
Cd106	0.01245	Cd108	0.00888
Cd110	0.1247	Cd111	0.12795
Cd112	0.24109	Cd113	0.12227
Cd114	0.28754	Cd116	0.07512
Cr50	0.04345	Cr52	0.83789
Cr53	0.09501	Cr54	0.02365
Cu63	0.6915	Cu65	0.3085
Fe54	0.05845	Fe56	0.91754
Fe57	0.02119	Fe58	0.00282
H1	0.99984426	H2	0.00015574
He3	2e-06	He4	0.999998
In113	0.04281	In115	0.95719
Mn55	1.0	Mo100	0.09744
Mo92	0.14649	Mo94	0.09187
Mo95	0.15873	Mo96	0.16673
Mo97	0.09582	Mo98	0.24292
N14	0.996337	N15	0.003663
Nb93	1.0	Ni58	0.680769
Ni60	0.262231	Ni61	0.011399
Ni62	0.036345	Ni64	0.009256
O16	0.9976206	O17	0.000379
O18	0.0020004	P31	1.0
S32	0.9504074	S33	0.0074869
S34	0.0419599	S36	0.0001458
Si28	0.9222968	Si29	0.0468316
Si30	0.0308716	Sn112	0.0097
Sn114	0.0066	Sn115	0.0034
Sn116	0.1454	Sn117	0.0768
Sn118	0.2422	Sn119	0.0859

Sn120	0.3258	Sn122	0.0463
Sn124	0.0579	Ti46	0.0825
Ti47	0.0744	Ti48	0.7372
Ti49	0.0541	Ti50	0.0518
U234	5.4e-05	U235	0.007204
U238	0.992742	V50	0.0025
V51	0.9975	Zr90	0.5145
Zr91	0.1122	Zr92	0.1715
Zr94	0.1738	Zr96	0.028

References

[31]

Pages

128, 130, 132, 134, 136, 137, 138, 139, 140, 142, 143, 144, 145, 149

Source 69 — Elemental Masses

Element	Mass [amu]	Element	Mass [amu]
Ag	107.868150	Al	26.981539
Ar	39.947799	B	10.811825
C	12.011115	Ca	40.078023
Cd	112.413818	Cr	51.996132
Cu	63.546040	Fe	55.845144
H	1.007982	He	4.002601
In	114.818267	Mn	54.938044
Mo	95.948779	N	14.006726
Nb	92.906373	Ni	58.693351
O	15.999305	P	30.973762
S	32.063879	Si	28.085384
Sn	118.710113	Ti	47.866745
U	238.028910	V	50.941465
Zr	91.223642		

References

[30]

Pages

137, 139, 140, 141, 145

Source 70 — Cycle 1 Assembly Loadings

Assembly ID	Uranium [g]	U-235 [g]	Enrichment [%]
A05	424944	13162	3.0973492978
A06	420716	13030	3.0971011324
A07	426067	13160	3.0887160939
A08	424475	13142	3.0960598386
A09	425874	13192	3.0976298154
A10	425803	13186	3.0967372236
A11	420801	13069	3.1057435700
B03	424193	13136	3.0967036231
B04	422216	13097	3.1019667658
B05	420894	13253	3.1487738005
B06	425287	6846	1.6097364838
B07	425899	13198	3.0988567712
B08	423432	6792	1.6040355949
B09	425449	13182	3.0983737181
B10	424324	6852	1.6148037820
B11	424062	13129	3.0960095458
B12	422104	13159	3.1174781570
B13	423343	13140	3.1038661322
C02	424937	13163	3.0976356495
C03	424170	13119	3.0928637103
C04	421871	10124	2.3997857165
C05	424615	6829	1.6082804423
C06	423086	10146	2.3980940045
C07	422483	6783	1.6055083873
C08	424345	10192	2.4018192744
C09	424595	6849	1.6130665693
C10	424891	10221	2.4055581314
C11	424941	6844	1.6105765271
C12	421583	10130	2.4028483122
C13	423048	13127	3.1029575840
C14	421975	13192	3.1262515552
D02	424800	13159	3.0976930320
D03	424180	10156	2.3942665849
D04	424406	10169	2.3960547212
D05	424911	10202	2.4009733803
D06	424399	6848	1.6135759038
D07	424181	10210	2.4069913551

D08	425152	6833	1.6071898991
D09	422222	10147	2.4032381070
D10	424412	6847	1.6132908589
D11	424304	10181	2.3994588785
D12	423100	10150	2.3989600567
D13	424783	10202	2.4016968664
D14	424281	13124	3.0932330225
E01	423404	13084	3.0901928182
E02	420730	13039	3.0991372139
E03	424543	6843	1.6118508608
E04	421801	10123	2.3999468944
E05	424255	6837	1.6115308011
E06	423596	10170	2.4008725295
E07	421655	6786	1.6093725913
E08	423553	10191	2.4060743284
E09	423530	6836	1.6140533138
E10	423784	10167	2.3990995413
E11	426061	6882	1.6152616644
E12	420485	10097	2.4012747185
E13	423910	6809	1.6062371730
E14	424243	13137	3.0965743689
E15	423782	13111	3.0938076653
F01	421004	13280	3.1543643291
F02	424776	6817	1.6048458482
F03	423535	10162	2.3993294533
F04	423810	6823	1.6099195394
F05	423695	10149	2.3953551493
F06	424865	6872	1.6174549563
F07	421380	10157	2.4104134036
F08	421443	6782	1.6092330398
F09	423216	10180	2.4053911005
F10	424117	6837	1.6120551640
F11	424105	10174	2.3989342262
F12	425283	6862	1.6135138249
F13	421755	10118	2.3990231295
F14	424904	6840	1.6097753846
F15	424964	13164	3.0976741559
G01	423798	13121	3.0960504769
G02	425033	13158	3.0957596234
G03	424241	6834	1.6108768365
G04	423025	10162	2.4022220909
G05	423622	6839	1.6144109607
G06	424373	10207	2.4051954295
G07	424759	6831	1.6082060651

157

G08	423952	10177	2.4005076046
G09	421474	6782	1.6091146785
G10	423211	10156	2.3997485888
G11	425181	6847	1.6103729941
G12	424361	10148	2.3913601863
G13	424788	6847	1.6118628586
G14	426234	13199	3.0966558276
G15	423030	13097	3.0959979198
H01	424112	13134	3.0968234806
H02	423343	6793	1.6046090286
H03	423810	10136	2.3916377622
H04	422511	6778	1.6042185884
H05	423653	10164	2.3991332529
H06	424642	6822	1.6065297356
H07	421497	10187	2.4168618045
H08	423849	6823	1.6097714044
H09	422875	10143	2.3985811410
H10	424615	6825	1.6073384124
H11	424072	10157	2.3951121508
H12	425265	6865	1.6142875619
H13	422934	10150	2.3999016395
H14	424688	6836	1.6096522624
H15	425788	13194	3.0987251872
J01	420911	13082	3.1080204604
J02	425904	13192	3.0974116233
J03	424409	6824	1.6078829620
J04	424468	10163	2.3942912069
J05	425512	6859	1.6119404388
J06	424294	10208	2.4058789424
J07	423432	6834	1.6139545429
J08	423016	10153	2.4001456210
J09	424375	6824	1.6080117820
J10	424281	10221	2.4090166658
J11	424993	6847	1.6110853591
J12	424165	10176	2.3990664010
J13	421347	6753	1.6027170005
J14	424730	13157	3.0977326772
J15	421853	13063	3.0965762955
K01	422860	13118	3.1022087689
K02	424618	6826	1.6075625621
K03	421148	10132	2.4058050851
K04	424555	6819	1.6061523242
K05	421432	10140	2.4060821200
K06	423746	6824	1.6103986822

K07	424555	10169	2.3952138121
K08	424044	6818	1.6078520154
K09	422699	10153	2.4019455925
K10	424649	6832	1.6088581393
K11	423288	10149	2.3976583319
K12	424956	6839	1.6093430849
K13	423244	10138	2.3953086163
K14	422255	6776	1.6047175285
K15	424116	13121	3.0937290741
L01	422352	13092	3.0997840664
L02	420794	13073	3.1067458186
L03	425338	6828	1.6053115405
L04	424261	10159	2.3945165830
L05	424742	6849	1.6125082992
L06	424150	10166	2.3967935872
L07	423764	6831	1.6119821410
L08	424256	10154	2.3933662694
L09	425410	6872	1.6153828072
L10	424950	10200	2.4002823862
L11	421625	6792	1.6109101690
L12	423639	10192	2.4058219380
L13	424023	6813	1.6067524639
L14	424050	13133	3.0970404433
L15	424459	13147	3.0973545148
M02	425885	13193	3.0977846132
M03	424014	10131	2.3893079002
M04	421257	10112	2.4004348889
M05	425262	10201	2.3987565313
M06	423693	6822	1.6101280880
M07	423907	10139	2.3917982010
M08	424198	6854	1.6157549069
M09	424072	10153	2.3941689147
M10	425652	6843	1.6076513208
M11	422201	10199	2.4156740510
M12	424551	10155	2.3919387777
M13	425089	10199	2.3992622721
M14	425657	13183	3.0970946090
N02	421693	13265	3.1456533545
N03	422588	13124	3.1056253372
N04	421881	10131	2.4013880691
N05	423101	6785	1.6036360113
N06	424140	10176	2.3992078087
N07	425284	6870	1.6153911269
N08	424883	10175	2.3947769151

N09	425421	6872	1.6153410386
N10	424268	10175	2.3982482770
N11	424275	6852	1.6149902775
N12	424620	10163	2.3934341293
N13	422582	13101	3.1002267016
N14	425319	13149	3.0915618630
P03	424427	13146	3.0973524305
P04	425671	13187	3.0979324408
P05	422784	13107	3.1001646231
P06	423297	6826	1.6125793474
P07	425103	13163	3.0964260426
P08	423857	6827	1.6106847357
P09	420685	13284	3.1577070730
P10	424630	6827	1.6077526317
P11	423052	13116	3.1003280921
P12	423471	13111	3.0960797788
P13	422419	13108	3.1030801171
R05	423062	13099	3.0962364854
R06	422801	13119	3.1028781862
R07	426100	13196	3.0969256043
R08	424656	13155	3.0978015146
R09	425240	13172	3.0975449158
R10	422084	13071	3.0967769449
R11	421775	13100	3.1059214036

To determine core-averaged enrichment for each enrichment type (1.6%, 2.4% and 3.1%), the Enrichment column was first separated by enrichment type. Then, all the enrichments for a given type were averaged. In order to compute densities, the total mass of Uranium is needed for each enrichment type. Both of these values are reported in the table below.

Enrichment Type	Actual Core-averaged Enrichment	Total Heavy Metal [g]
1.6%	1.6100562050%	27570971
2.4%	2.3999267408%	27104522
3.1%	3.1022104528%	27115256
Core avg. enrichment	2.366789812%	
Total Heavy Metal Mass	81.79 MT	

References

[18]

Pages

3, 127, 129, 131

Source 71 — Cycle 2 Assembly Loadings

Assembly ID	Uranium [g]	U-235 [g]	Enrichment [%]
A06	426378	14523	3.4061325866
A07	425150	13582	3.1946371869
A08	426115	14522	3.4080001877
A09	425256	13588	3.1952518013
A10	425004	14481	3.4072620493
B04	424679	13568	3.1948836651
B05	424804	13591	3.1993578215
B11	425385	13581	3.1926372580
B12	425013	13591	3.1977845384
C03	426452	14523	3.4055415381
C06	425896	13653	3.2057121926
C10	425229	13600	3.1982766933
C13	426588	14507	3.4007051300
D02	425787	13600	3.1940853056
D05	426941	13636	3.1938839324
D11	425586	13580	3.1908944373
D14	425027	13576	3.1941500187
E02	424137	13537	3.1916574126
E04	426071	13608	3.1938338915
E06	423952	13485	3.1807846171
E10	426192	13632	3.1985583962
E12	424567	13551	3.1917223901
E14	424969	13613	3.2032924755
F01	426533	14524	3.4051292632
F03	425176	13601	3.1989105688
F05	425158	13594	3.1973995550
F11	424465	13545	3.1910758249
F13	424866	13596	3.2000677861
F15	426756	14527	3.4040529014
G01	424316	13554	3.1943174427
G15	425838	13648	3.2049746617
H01	424172	14448	3.4061654235
H15	426814	14554	3.4099162633
J01	426796	13635	3.1947347210
J15	424420	13552	3.1930634749
K01	424667	14464	3.4059627897
K03	424774	13549	3.1896961678

K05	425597	13596	3.1945713903
K11	425570	13629	3.2025283737
K13	424532	13566	3.1955188301
K15	426322	14520	3.4058763095
L02	425023	13605	3.2010032398
L04	427865	13665	3.1937643883
L06	425056	13597	3.1988726191
L10	424429	13585	3.2007709181
L12	424652	13520	3.1837834274
L14	424696	13559	3.1926366154
M02	425055	13586	3.1962922445
M05	424994	13578	3.1948686334
M11	424679	13566	3.1944127211
M14	426884	13639	3.1950131652
N03	427113	14526	3.4009735129
N06	424710	13587	3.1991241082
N10	425867	13611	3.1960682561
N13	427170	14549	3.4059039727
P04	425199	13588	3.1956801404
P05	425430	13593	3.1951202313
P11	426461	13632	3.1965408326
P12	425352	13585	3.1938253494
R06	425527	14493	3.4058943381
R07	426122	13614	3.1948596881
R08	426663	14554	3.4111230643
R09	425742	13589	3.1918391890
R10	424350	14449	3.4049723106

To determine core-averaged enrichment for each enrichment type (3.2% and 3.4%), the Enrichment column was first separated by enrichment type. Then, all the enrichments for a given type were averaged. In order to compute densities, the total mass of Uranium is needed for each enrichment type. Both of these values are reported in the table below.

Enrichment Type	Actual Core-averaged Enrichment	Total Heavy Metal [g]
3.2%	3.1954737208%	21066701
3.4%	3.4058507275%	7048788

References

[18]

Pages